

NUMERICAL ANALYSIS OF BALLISTIC AND SHAPED CHARGE IMPACT
ON METAL TARGETS

A THESIS SUBMITTED TO
THE GRADUATE SCHOOL OF NATURAL AND APPLIED SCIENCES
OF
MIDDLE EAST TECHNICAL UNIVERSITY

BY

YAĞMUR GÖÇMEN

IN PARTIAL FULFILLMENT OF THE REQUIREMENTS
FOR
THE DEGREE OF MASTER OF SCIENCE
IN
AEROSPACE ENGINEERING

MAY 2023

Approval of the thesis:

**NUMERICAL ANALYSIS OF BALLISTIC AND SHAPED CHARGE
IMPACT ON METAL TARGETS**

submitted by **YAĞMUR GÖÇMEN** in partial fulfillment of the requirements for the degree of **Master of Science in Aerospace Engineering Department, Middle East Technical University** by,

Prof. Dr. Halil Kalıpçılar
Dean, Graduate School of **Natural and Applied Sciences**

Prof. Dr. Serkan Özgen
Head of Department, **Aerospace Engineering**

Assoc. Prof. Dr. Tuncay Yalçinkaya
Supervisor, **Aerospace Engineering, METU**

Examining Committee Members:

Prof. Dr. Altan Kayran
Aerospace Engineering, METU

Assoc. Prof. Dr. Tuncay Yalçinkaya
Aerospace Engineering, METU

Prof. Dr. Erdem Acar
Mechanical Engineering, TOBB ETU

Assoc. Prof. Dr. Ercan Gürses
Aerospace Engineering, METU

Assist. Prof. Dr. Görkem Eğemen Güloğlu
Aerospace Engineering, METU

Date:30.05.2023

I hereby declare that all information in this document has been obtained and presented in accordance with academic rules and ethical conduct. I also declare that, as required by these rules and conduct, I have fully cited and referenced all material and results that are not original to this work.

Name, Surname: Yağmur Göçmen

Signature :

ABSTRACT

NUMERICAL ANALYSIS OF BALLISTIC AND SHAPED CHARGE IMPACT ON METAL TARGETS

Göçmen, Yağmur

M.S., Department of Aerospace Engineering

Supervisor: Assoc. Prof. Dr. Tuncay Yalçinkaya

May 2023, 103 pages

This thesis presents a numerical study of the behavior of metal targets subjected to ballistic impact and shaped charge impact, utilizing finite element (FE) and smoothed particle hydrodynamics (SPH) methods. The study encompasses an in-depth analysis of different damage models and modeling techniques for various configurations, and the obtained results are validated using available experimental tests from the literature. Numerical modeling of ductile failure is simulated through the Johnson-Cook (JC) and modified Mohr-Coulomb (MMC) uncoupled damage models. Obtained results are validated using available experimental tests from the literature. In the first part of the study, the effects of impact angle, target plate thickness, and projectile nose shape on ballistic impact are investigated on aluminum alloy 2024-T351. The behavior of the target plate is compared using JC and MMC damage by utilizing FE and SPH methods. Then, material parameters for JC and MMC damage models of armor steel ArmoX 500T are calibrated using available experimental data from the literature and validated by tensile and ballistic impact test simulations. Furthermore, the ballistic performance of the ArmoX 500T steel target is discussed using these damage models with varying target thickness, impact angle, and projectile nose shape.

Finally, a numerical analysis of shaped charge impact is conducted to investigate the jet formation process and its penetration performance on metal targets. This process is mainly used against heavily armored vehicles or in civil applications such as metal cutting and oil well completion. Conical and bowl-shaped liner geometries are simulated with various configurations to observe their effects on projectile shape and penetration capability is also studied. The ballistic performance of explosively formed projectiles (EFP) with different obliquity and target thicknesses are investigated and discussed by comparing FE and SPH methods. #45 and Armox 500T steels are used as the target materials, and the material behavior and failure mechanisms are modeled using the JC model. The results demonstrate that blunt projectiles, which are the most sensitive to parameter change and damage models. Moreover, FE outperforms the SPH method in predicting failure mechanisms; however, SPH can be useful for predicting residual velocity and hole diameter results. Furthermore, the performance of JC and MMC varies for different configurations.

Keywords: Ballistic impact, Shaped charge impact, Ductile failure, FEM, SPH

ÖZ

METAL HEDEFLER ÜZERİNDE BALİSTİK VE BOŞLUKLU İMLA HAKKI ÇARPMASININ SAYISAL ANALİZİ

Göçmen, Yağmur

Yüksek Lisans, Havacılık ve Uzay Mühendisliği Bölümü

Tez Yöneticisi: Doç. Dr. Tuncay Yalçınkaya

Mayıs 2023 , 103 sayfa

Bu tez, sonlu elemanlar (FE) ve düzleştirilmiş parçacık hidrodinamiği (SPH) yöntemlerini kullanarak, balistik ve boşluklu imla hakkı darbesine maruz kalan metal hedeflerin davranışının sayısal bir incelemesini sunmaktadır. Çalışma, farklı hasar modellerinin ve çeşitli konfigürasyonlar için modelleme tekniklerinin derinlemesine bir analizini kapsar ve elde edilen sonuçlar, literatürdeki mevcut deneysel testler kullanılarak doğrulanmıştır. Sayısal sünek hasar modellemesi, Johnson-Cook (JC) ve modifiye edilmiş Mohr-Coulomb (MMC) kırılma modelleri aracılığıyla simüle edilmiştir. Elde edilen sonuçlar, literatürdeki mevcut deneysel testler kullanılarak doğrulanmıştır. Çalışmanın ilk bölümünde, 2024-T351 alüminyum hedef üzerinde darbe açısının, hedef plaka kalınlığının ve mermi burun şeklinin balistik etki üzerindeki etkileri incelenmektedir. Hedef plakanın davranışı, FE ve SPH yöntemleri kullanılarak JC ve MMC hasarı kullanılarak karşılaştırılmıştır. Ardından, zırh çeliği Armox 500T'nin JC ve MMC hasar modellerine yönelik malzeme parametreleri, literatürdeki mevcut deneysel veriler kullanılarak kalibre edilip, çekme ve balistik darbe testi simülasyonlarıyla doğrulanmıştır. Ayrıca, Armox 500T çelik hedefin balistik performansı, değişen hedef

kalınlığı, çarpma açısı ve mermi burnu şekli ile bu hasar modelleri kullanılarak tartışılmaktadır. Son olarak, jet oluşum sürecini ve metal hedefler üzerindeki penetrasyon performansını araştırmak için boşluklu imla hakkı etkisinin sayısal bir analizi yapılmıştır. Bu süreç, ağırlıklı olarak ağır zırhlı araçlara karşı veya metal kesme ve petrol kuyusu tamamlama gibi sivil uygulamalarda kullanılır. Konik ve çanak şekilli astar geometrileri, mermi şekli üzerindeki etkilerini gözlemlemek için çeşitli konfigürasyonlarla simüle edilmiş ve penetrasyon kabiliyeti de incelenmiştir. Farklı eğiklik ve hedef kalınlıklarına sahip patlayarak şekillendirilmiş mermilerin (EFP) balistik performansı incelenmiş ve FE ve SPH yöntemleri karşılaştırılarak tartışılmıştır. #45 ve ArmoX 500T çelikleri hedef malzeme olarak kullanılmış, malzeme davranışı ve hasar mekanizmaları JC modeli kullanılarak modellenmiştir. Sonuçlar, parametre değişikliğine ve hasar modellerine en hassas olan küt mermilerin olduğunu göstermektedir. Ayrıca FE, kırılma mekanizmasını tahmin etmede SPH yönteminden daha iyi performans gösterir; ancak, SPH artık hız ve delik çapı sonuçlarını elde etmek için kullanılabilir. Ayrıca, JC ve MMC'nin performansı farklı konfigürasyonlar için değişiklik göstermektedir.

Anahtar Kelimeler: Balistik çarpışma, Boşluklu imla hakkı çarpışması, Sünek kırılma, SEM, SPH

To my family.

ACKNOWLEDGMENTS

First and foremost, I would like to express my gratitude to my supervisor, Assoc. Prof. Dr. Tuncay Yalçinkaya. His advice was invaluable during the research and writing of this thesis.

I am truly thankful to Can Erdoğan and Hande Vural for their assistance and contributions.

I wish to extend my appreciation to my friends İlbilge Umay Aydınır and Sarim Waseem.

I would like to express my sincerest gratitude to Barış İlgar for his support and encouragement.

I am incredibly grateful to my parents, Ümit Göçmen and Vildan Göçmen and my cat, Posirik Göçmen, for their love and support.

I am deeply grateful to Joey DeMaio, Eric Adams, and Scott Columbus, who has been a constant source of inspiration and motivation for me throughout my life.

Most importantly, I want to express my sincere gratitude to Mustafa Kemal Atatürk, whose contributions to our nation have left an enduring legacy that has had a profound impact on me and many others.

TABLE OF CONTENTS

ABSTRACT	v
ÖZ	vii
ACKNOWLEDGMENTS	x
TABLE OF CONTENTS	xi
LIST OF TABLES	xiv
LIST OF FIGURES	xvi
CHAPTERS	
1 INTRODUCTION	1
1.1 Ballistic Impact Parameters	4
1.1.1 Projectile Nose Shape	5
1.1.2 Impact Angle	6
1.1.3 Target Thickness	7
1.1.4 Target Material	7
1.2 Shaped Charge	9
1.3 Aim of The Study	11
2 NUMERICAL METHODS	15
2.1 Stress states	15
2.2 Plasticity	17

2.3	Damage Models	19
2.4	Equation of State (EOS)	21
2.5	SPH method	22
3	NUMERICAL ANALYSIS OF BALLISTIC IMPACT THROUGH FE AND SPH METHODS	27
3.1	Material Parameters	28
3.2	Numerical Modelling	28
3.3	Results and Discussion	34
4	A NUMERICAL BALLISTIC PERFORMANCE INVESTIGATION OF ARMOX 500T STEEL THROUGH DUCTILE DAMAGE MODELS	41
4.1	Numerical models and calibration	41
4.1.1	FE modeling of tensile tests	41
4.1.2	Plastic Deformation	45
4.1.3	Failure models and calibration process	46
4.1.4	Failure model validation	46
4.2	Ballistic Impact Simulations	48
4.3	Results and discussion	52
4.3.1	Comparisons with experiments	54
4.3.2	Comparison of the JC and MMC models under various con- figurations	56
4.3.3	Comparison of failure modes	59
5	A NUMERICAL STUDY ON THE BALLISTIC PERFORMANCE OF PROJECTILES FORMED BY SHAPED CHARGE	65
5.1	Numerical analysis	65
5.1.1	Jet formation process	65

5.1.2	Penetration process and damage modeling	69
5.2	Results and Discussion	73
5.2.1	Comparison with experiments	73
5.2.2	Jet formation results	75
5.2.3	Ballistic performance analysis	78
6	CONCLUSIONS	89
	REFERENCES	93

LIST OF TABLES

TABLES

Table 3.1	Material parameters of aluminum alloy 2024-T351.	28
Table 3.2	JC and MMC fracture criteria constants for aluminum alloy 2024-T351.	28
Table 4.1	The Voce law parameters of Armox 500T steel.	45
Table 4.2	Average Lode angle parameter ($\bar{\theta}_{av}$), average triaxiality (η_{av}), and fracture strain (ε_f) values for Armox 500T steel.	47
Table 4.3	JC and MMC damage model parameters for Armox 500T steel. . . .	49
Table 4.4	Experimental and numerical results for 7.62 API projectile with 8 mm thick target.	54
Table 4.5	Experimental and numerical results for 12.7 API projectile with 10 mm thick target.	55
Table 5.1	Properties of copper jet at $160\mu s$ with varying element sizes.	67
Table 5.2	Properties of iron jet at $160\mu s$ with varying element sizes.	67
Table 5.3	Material parameters of copper and iron liners.	68
Table 5.4	EOS parameters for copper and iron liners.	68
Table 5.5	Material parameters of explosive.	69
Table 5.6	JC plasticity parameters of #45 steel and Armox 500T	72

Table 5.7	JC damage model parameters of #45 and Armox 500T steels.	73
Table 5.8	EFP velocities at the onset of impact.	77
Table 5.9	Hole diameter at the inlet after penetration using the projectile geometries in Figure 5.9 (correspond to the experimental setup). Simulation vs. Experiments [55]	78

LIST OF FIGURES

FIGURES

Figure 1.1	Failure mechanism in ballistic impact [3].	2
Figure 1.2	Ogival (left), blunt (middle) and hemispherical (right) nose shapes.	5
Figure 1.3	Illustration of the oblique impact.	6
Figure 1.4	Monolithic (left), layered-in-contact (middle) and spaced lay- ered (right) target configurations.	8
Figure 1.5	Illustration of shaped charge impact process.	10
Figure 2.1	Geometrical illustration of Lode angle. [93]	17
Figure 2.2	The von Mises yield surface.	18
Figure 2.3	Visual representation of FE (left) and SPH (right) methods.	23
Figure 2.4	Visual representation cubic spline kernel function [94].	25
Figure 3.1	Numerical model set-up.	27
Figure 3.2	Geometry of the projectiles and targets	29
Figure 3.3	Initial vs. residual velocity curves of full, half and quarter models.	30
Figure 3.4	Mesh convergence study.	31
Figure 3.5	Enlarged view of the target for SPH simulations.	32
Figure 3.6	Mesh convergence study for SPH simulations.	32

Figure 3.7	Comparison of coarse and fine configurations for FE and SPH methods.	33
Figure 3.8	Energy time history of the target and projectile.	34
Figure 3.9	Initial vs. residual velocity curves of FE-JC, FE-MMC, SPH-JC, SPH-MMC models for blunt projectile at 9.94 mm target thickness. Experimental data from [38].	35
Figure 3.10	Initial vs. residual velocity curves of FE-JC, FE-MMC, SPH-JC, SPH-MMC models for hemispherical projectile at 9.94 mm target thickness. Experimental data from [38].	35
Figure 3.11	Initial vs. residual velocity curves of FE-JC, FE-MMC, SPH-JC, SPH-MMC models for ogival projectile at 9.94 mm target thickness. Experimental data from [38].	36
Figure 3.12	Target thickness-residual velocity curves of hemispherical projectile for FE-JC, FE-MMC, SPH-JC, SPH-MMC models at 250 m/s initial velocity with 3 mm, 6 mm, and 9.94 mm thicknesses.	37
Figure 3.13	Impact angle-residual velocity curves of blunt, hemispherical, and ogival projectile for FE-JC and FE-MMC models at 350 m/s initial velocity with 6 mm thickness.	37
Figure 3.14	Failure mechanisms of blunt, hemispherical, and ogival projectile at 350 m/s initial velocity with 6 mm thickness for 0°, 15°, 30°, 45°, and 60° obliquity with FE-MMC.	38
Figure 3.15	Failure mechanisms of 6 mm thickness ogival projectile at 350 m/s initial velocity with FE-JC, FE-MMC, SPH-JC, SPH-MMC for 0°, 15°, 30°, 45°, and 60° obliquity.	39
Figure 4.1	Geometry (a) and boundary conditions (b) of specimen 5.b.	42
Figure 4.2	Force vs. gauge length elongation curve with varying element sizes for specimen 5.b.	43

Figure 4.3	Force vs. gauge length elongation curve for an eighth and full scale specimens	44
Figure 4.4	Geometry of specimens 2.a (left), 8.b (middle) and 12.c (right).	44
Figure 4.5	True stress-plastic strain curve of experimental data versus Voce law fit.	45
Figure 4.6	JC and MMC damage model curve fits.	48
Figure 4.7	Comparison of JC and MMC damage models with the experimental data [90]. Force vs gauge length elongation for specimens (a) 5.b, (b) 8.b, (c) 2.a and (d) 12.c.	49
Figure 4.8	Projectile geometries (left), ballistic impact FE model boundary conditions (middle), impact angle (α) illustration (right).	50
Figure 4.9	Quarter target (left), full scale target (right).	51
Figure 4.10	Mesh convergence study.	52
Figure 4.11	Residual velocity (m/s) vs. maximum time increments curve.	53
Figure 4.12	Energy time history of the target and projectile.	53
Figure 4.13	Failure mechanism of Armox 500T steel against 7.62 API projectile with 8 mm thick target. Experimental data from [91].	55
Figure 4.14	Failure mechanism of Armox 500T steel against 12.7 API projectile with 10 mm thick target. Experimental data from [91].	56
Figure 4.15	Residual velocity (m/s) vs. initial velocity (m/s) curves for (a) 4 mm and (b) 8 mm thick targets	58
Figure 4.16	Difference of JC and MMC models in (%) vs. initial velocity (m/s) at 0° impact angle for 4 mm and 8 mm thick targets.	59
Figure 4.17	(a) Residual velocity (m/s) vs. target thickness (mm) curves and (b) percent difference between JC and MMC damage models for various target thickness at 900 m/s initial velocity.	60

Figure 4.18	(a) Residual velocity (m/s) vs. impact angle (α) curves and (b) percent difference between JC and MMC damage models for various impact angles at 900 m/s initial velocity.	61
Figure 4.19	Failure mechanisms of 7.62 API projectile at 900 m/s initial velocity for 4 mm target thickness and at 0°, 15°, 30°, 45°, and 60° obliquity with JC and MMC models.	62
Figure 4.20	Failure mechanisms of blunt projectile at 900 m/s initial velocity for 4 mm target thickness and at 0°, 15°, 30°, 45°, and 60° obliquity with JC and MMC models.	62
Figure 4.21	Failure mechanisms of hemispherical projectile at 900 m/s initial velocity for 4 mm target thickness and at 0°, 15°, 30°, 45°, and 60° obliquity with JC and MMC models.	63
Figure 5.1	Geometry of explosive charge and bowl-shaped (left) and conical (middle) liners. Axisymmetric FE model of the bowl-shaped liner (right).	66
Figure 5.2	Jet tip velocity (m/s) vs. maximum time increments curve.	67
Figure 5.3	Velocity variation plot for various points on formed jets.	70
Figure 5.4	Boundary conditions of the target (left) and illustration of thickness (t) and impact angle (β) (right).	71
Figure 5.5	FE model with max mesh size: 2 mm, min mesh size: 0.25 mm (left) and SPH model with max mesh size: 2 mm, min mesh size: 0.20 mm (right) models of the target.	71
Figure 5.6	Mesh convergence study for $\alpha = 65^\circ$ and $m = 7.5$ mm with FE and SPH methods.	72
Figure 5.7	Formed 2D shape and 3D models of EFPs at the onset of impact with ABAQUS. Deformable EFP is from [88] with LS-DYNA.	74

Figure 5.8	Failure mechanisms of 25 mm thick #45 steel target with FE and SPH methods.	75
Figure 5.9	Formed 2D shape and 3D models of EFPs at the onset of impact for bowl-shaped liner with $m = 9.5$ mm (correspond to the experimental setup).	76
Figure 5.10	Formed 2D shape and 3D models of EFPs at the onset of impact at various configurations.	77
Figure 5.11	Energy time history of the target and projectile.	79
Figure 5.12	Failure mechanisms of #45 steel and Armox 500T targets using copper and iron EFPs.	80
Figure 5.13	Failure mechanisms of #45 steel and Armox 500T targets using EFPs with various cone angles.	81
Figure 5.14	Failure mechanisms of #45 steel and Armox 500T targets using EFPs with different m parameter.	82
Figure 5.15	Residual velocity and hole diameter vs. cone angle and m parameter for #45 steel and Armox 500T targets with FE and SPH methods.	83
Figure 5.16	Penetration depth vs. cone angle and m parameter.	84
Figure 5.17	Maximum penetration depth for 250 mm thick Armox 500T.	85
Figure 5.18	Plot for #45 and Armox 500T (a) using conical liner with $\alpha = 65^\circ$ and (b) steel targets using EFPs with $\alpha = 65^\circ$ and $m = 11.5$	86
Figure 5.19	Failure mechanisms of #45 steel and Armox 500T targets using EFPs with $\alpha = 65^\circ$ and $m = 11.5$	87

CHAPTER 1

INTRODUCTION

Body armor has been used for protection for centuries. In times of battle, warriors were protected by helmets and harnesses from weapons like swords, axes, and arrows, while barding was used to protect horses. Since the dawn of human history, numerous armor combinations have been created. For instance, in ancient times, different-sized plates made of bone, antler, and ivory were used to make armor vests [1]. Steel body armor was commonly used during the medieval era [2]. In modern applications, many structures in the aerospace and defense industries are required to be lightweight and resistant to impact loads, such as bird strikes in aviation and ballistic impact on military vehicles. Ballistic impact refers to the high-velocity collision of two or more objects with one another or a target. This can happen either naturally or through artificial ways. The projectile's velocity ranges from around 500 m/s to 1300 m/s. The ballistic impact is a process in which materials are subjected to high strain rate loading. Ballistic impact experiments can be used to analyze material failure in order to assist in the design process. The ballistic impact experiment setup consists of a projectile and a target. Projectiles can have a variety of shapes or be formed during the impact process, such as a shaped charge. Target plates are constructed from high-strength metals like steel and aluminum alloys. The target can also be made of composites, ceramics, or a combination of different materials. By investigating the behavior of the target against the impact load, stronger and more resilient structures can be designed and manufactured. The penetration of the projectile into the target results in damage to the target which is referred to as the failure mechanism. There are some characteristic failure mechanisms in ballistic impact as shown in Figure 1.1. On metal targets petaling, shear plugging, fragmentation, and ductile hole growth are observed commonly. Petaling failure mechanism is a phenomenon that occurs at

high strain rates typically associated with impact, where metal deforms around the point of impact into thin sheets resembling flower petals. Moreover, plugging is a failure mechanism where a plug is separated from the target and creates a hole, and fragmentation is another failure mechanism where the target breaks apart into smaller pieces.

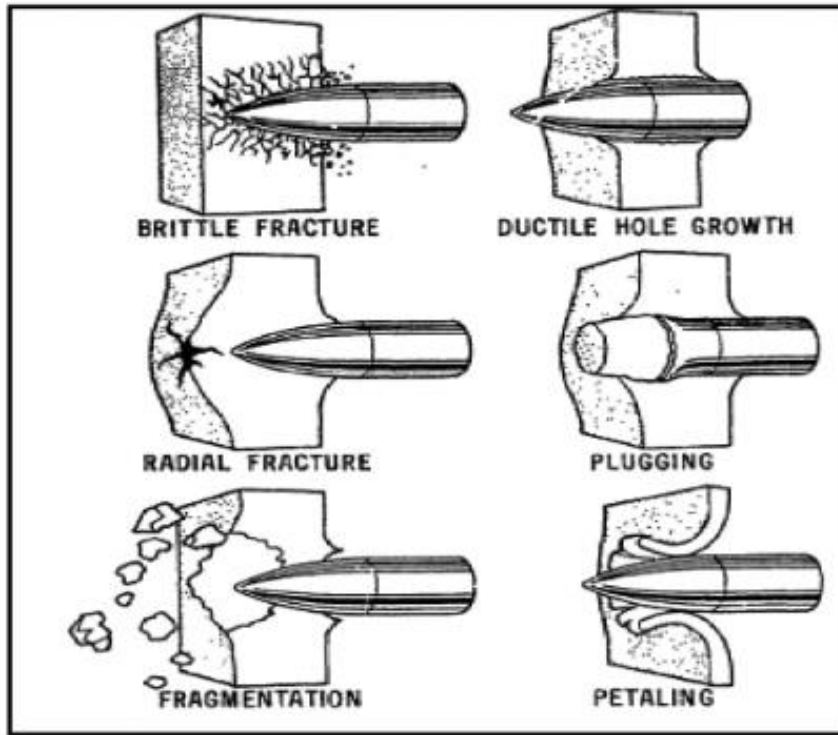


Figure 1.1: Failure mechanism in ballistic impact [3].

The fracture behavior of the target is strongly reliant on various factors, including impact velocity, projectile nose shape, target plate thickness, the material of the target, and impact angle. Experiments are necessary to establish the ballistic limit of materials since the ballistic impact is a highly parameter-dependent process. In literature, there are a variety of studies (see e.g. [4, 5, 6, 7]) that conducted ballistic impact experiments by firing a projectile towards steel and aluminum targets. However, experiments are costly and challenging to carry out when all design requirements are taken into account.

As an alternative to experiments, numerical approaches are shown to be efficient in predicting the results with reduced costs. The numerical modeling of ballistic im-

impact has been successfully implemented using the finite element (FE) approach (see e.g. [8, 9, 10, 11]). They are successful in capturing residual velocity and failure mode results that are in good correlation with the experiments. However, the FE approach is prone to high mesh dependencies and mesh distortion issues when simulating failure under high deformations. Meshless simulation techniques have been suggested as a solution to mesh-related issues, such as smoothed particle hydrodynamics (SPH). SPH is a particle-based technique that uses particle interpolation to determine smoothed field variables. These particles, which have mass, velocity, and location, define the geometry of the numerical model. The SPH approach is an efficient alternative for FE method impact simulations. SPH has a higher computational cost and cannot satisfy fundamental boundary requirements. Ballistic impact with various target thicknesses and projectile nose shapes is studied successfully using the SPH technique [12, 13].

Ballistic impact generally results in ductile failure of the metal target. Ductile fracture has been extensively studied through several numerical techniques such as cohesive zone models [14, 15, 16, 17, 18], micromechanically motivated porous plasticity models [19, 20, 21] and phenomenological models [22, 23, 24]. To anticipate ductile failure using FE analysis, an efficient method is to employ coupled or uncoupled phenomenological ductile fracture criteria. In coupled approach, the damage parameter directly affects the constitutive equations resulting in material degradation. In the uncoupled approach, damage parameter and constitutive equations are independent of one another until complete failure occurs. The uncoupled approach is more commonly used due to lower computational cost and practical application in engineering problems (see e.g. [25, 26]). In this thesis, uncoupled methods are utilized.

The accuracy of the FE approach is mostly dependent on how correctly the material is represented in the numerical model. The process of ballistic impact is subject to high temperatures and strain rates. Hence it is important to base the FE model on these effects. Ballistic impact on metal targets has been studied through various damage models integrated with FE analysis. One of the most used damage models in ballistic impact, Johnson-Cook (JC), incorporates the effects of temperature, strain rate, and stress triaxiality. JC model is successfully utilized for Weldox 460E steel, Ti-6Al-4V, 1100-H1 aluminum, and Inconel 718 targets with various set-ups [27, 28, 29, 30].

However, JC damage model parameters are calibrated at a constant Lode angle parameter which indicates that JC is not Lode-dependent. In shear-dominated failure mechanisms it is important to capture Lode parameter effects [31]. Some damage models, such as modified Mohr-Coulomb (MMC), incorporate the influence of the Lode parameter. In references [32, 33, 34, 35] Lode-dependent Cockcroft and Latham (CL) damage model is utilized in predicting damage in ballistic impact simulations with various configurations. A good agreement between the results and the experiments is obtained. Roth et al. [36] and Frasier et al. [37] adapted Lode-dependent Hosford-Coulomb (HC) damage model for aluminum 7020-T6 and Mars 300 armor steel targets and results align with experimental data. In [38, 39] effectiveness of the Lode parameter in ballistic impact is investigated by comparing MMC with a Lode-independent damage model using various projectile nose shapes. The results demonstrate that the Lode parameter has the greatest influence on blunt-nosed projectiles and the least effect on ogival-nosed projectiles. Moreover, in [40, 41, 42] effect of the Lode parameter is investigated with the same method using Weldox 700E steel, 2024-T351 aluminum, and double-layered 2024-T351 aluminum plates. For 2024-T351 aluminum plates, it is shown that MMC provides more accurate results than the JC damage model compared with experiments. However, when Weldox 700E steel is investigated with MMC and modified JC, both models provide accurate ballistic limit velocities and failure mechanisms compared with experimental data. As a result, the Lode parameter necessity is affected by both the material and the projectile nose shape. Since the ballistic impact is a highly parameter-dependent process, the necessity and efficiency of the Lode parameter should be further investigated using different configurations. In the first section, ballistic impact parameters are explained. The impact of shaped charges is described further in the second section.

1.1 Ballistic Impact Parameters

The target's fracture behavior is heavily influenced by several factors, including projectile nose shape, impact angle, target thickness, and target material. The effects of these parameters on ballistic impact are commonly studied and summarized in this section.

1.1.1 Projectile Nose Shape

The shape of the projectile nose is an essential design parameter that influences the dominant stress state. As a result, different nose-shaped projectiles have characteristic failure modes. The nose shape of a projectile may sometimes be determined just by looking at the damage that has occurred on the target plate. In Figure 1.2, the most typical projectile nose shapes are shown as ogival, blunt, and hemispherical, respectively.

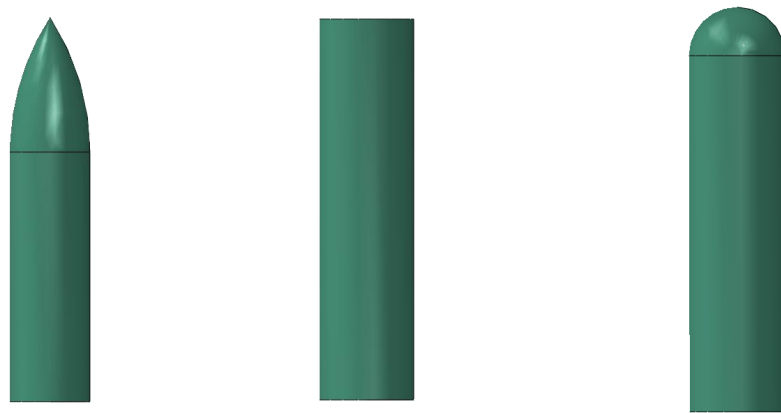


Figure 1.2: Ogival (left), blunt (middle) and hemispherical (right) nose shapes.

In references [34, 38, 39] ballistic response of blunt, ogival, hemispherical and spherical projectile nose shapes are investigated. They discovered that as the impact angle increases, the residual velocity of the projectiles converge towards each other. For the targets impacted by hemispherical and blunt projectiles, shear plugging is identified as the failure mechanism. For ogival projectiles petalling is observed. Moreover, it is shown that the failure mechanism is petalling and disc-like plug forming for the spherical projectile. Hole enlargement and fragmentation are also observed for all nose shapes, however, the size and amount of fragmentation depend on the configuration. It is discovered that the spherical projectile has the highest ballistic limit velocity followed by the ogival projectile while the blunt projectile has the lowest. The ballistic limit refers to the minimum velocity necessary for a projectile to successfully penetrate a particular target.

1.1.2 Impact Angle

In a ballistic impact model, the impact angle is the angle between the projectile and the direction of the target, as illustrated in Figure 1.3. It is an important component in resistant target design. The obliquity to the normal governs a variety of factors, including how obliquely a projectile may contact and still induce penetration, as well as damage to the target. When a projectile strikes a target, it may occasionally bounce back from the target, a phenomenon known as a "ricochet".

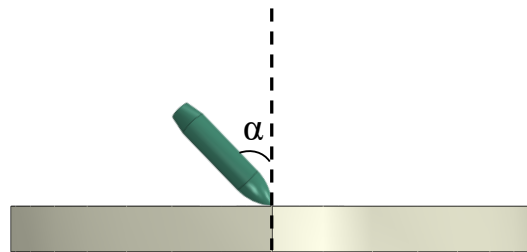


Figure 1.3: Illustration of the oblique impact.

1100-H12 and 7020-T6 aluminum targets are examined with various obliquity in [36, 43]. It is shown that aside from characteristic failure modes for different nose shapes, with the increase in obliquity, the size of the hole in the target increased as well. Additionally, failure mechanisms in the target switch from shear plugging to tearing as the obliquity increases. Similarly, the ballistic limit increases as obliquity increases.

Oblique impact on various configurations is investigated and the critical impact angle for a projectile to ricochet is discussed using mild steel targets in [44]. Oblique angle varied from 0° to 60° . At low obliquity, the ballistic performance of the various configurations did not differ significantly. However, at higher obliquity, each configuration's ballistic performance varied. It is also mentioned that as obliquity increases, the ballistic resistance of the target increases. This is due to the fact that the effective target thickness increases with obliquity.

1.1.3 Target Thickness

Target thickness is important in ballistic impact as it directly influences the level of protection provided against projectiles. While thicker targets present increased resistance to penetration, it is important to note that the efficiency of the armor is not consistently optimized by maximizing thickness alone. Han et al. [45] studied the ballistic performance of 2024-T351 aluminum plates struck by blunt nose-shaped projectiles. Target thickness varied as 2, 4, 4.82, and 8 mm. They discovered that shear plugging failure occurred regardless of the target's thickness. Additionally, it is stated that as target thickness increases, ballistic limit velocity decreases.

Furthermore, [44, 46, 47] studied monolithic, layered, layered-in-contact, and spaced layered target configurations with oblique and normal impact. Monolithic, layered-in-contact, and spaced layered target configurations are illustrated in Figure 1.4. These layers are not necessarily made of the same material. It is shown that the resistance of the structure decreases when multiple layers of equal thickness are added. Additionally, ballistic limit velocities are highest at higher obliquity. It has been discovered that as the target's thickness increases, so does its resistance. For monolithic, layered-in-contact, and spaced layered configurations, the residual velocity of the projectile did not vary significantly at a normal impact angle. Moreover, as the number of layers increases, the ballistic limit velocity decreases. Layered-in-contact configurations have a higher ballistic limit velocity than spaced layered configurations. Additionally, it is stated that when the first layer of the target is thinner than the second layer, layered configurations have better ballistic resistance.

1.1.4 Target Material

Material selection is critical in the aerospace and defense industries. A vehicle should be resistant to ballistic loads while simultaneously being light. A material with the highest ballistic resistance is not necessarily beneficial in and of itself. Design requirements should be taken into account. By optimizing the weight and resistance characteristics, a more efficient armor may be manufactured. More resistant and lightweight configurations may be produced by layering various materials instead

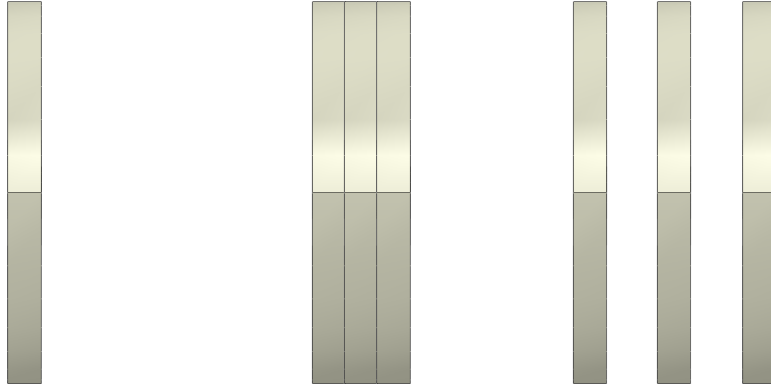


Figure 1.4: Monolithic (left), layered-in-contact (middle) and spaced layered (right) target configurations.

of one material. However, because there are so many possibilities for optimization, it would be highly costly to conduct experiments for each design.

Senthil et al. [48] investigated the ballistic performance of low ductility-high strength (armor steel), high ductility-low strength (mild steel), and medium ductility-medium strength (aluminum) metal targets using 7.62 AP projectile. It is observed that the best ballistic performance is shown by armor steel, followed by mild steel and aluminum. Steel targets, on the other hand, have a larger areal density than aluminum targets. Various combinations of these metal targets are studied and it is shown that the superior design is using layered armor steel-mild steel-aluminum configuration. Not only does this configuration improve ballistic resistance, but it also reduces areal density.

Weldox 700E steel and 7075-T651 aluminum target plates are investigated with various configurations in [49]. It is reported that although aluminum is at least twice as thick as steel targets at a comparable areal density, aluminum has higher ballistic performance at that areal density. Moreover, a superior design is shown to be an aluminum-steel layered configuration. This implies that more resistant and lightweight armors may be created employing two high-strength aluminum and steel layered designs.

Metal targets can also be layered with other materials, such as composites. Palta et al. [50] conducted a parametric study using Weldox 700E steel and Kevlar 129/epoxy.

Thirty different tests are carried out in monolithic, layered, and hybrid configurations. It is concluded that a hybrid configuration offers better ballistic resistance while reducing weight by 26% compared to a monolithic Weldom 700E steel configuration.

It should be noted that the computational cost of simulating numerous configurations to find the best configuration is high. Paman et al. [51] discussed an optimization methodology to determine the superior configuration. To determine ballistic performance, a parameter is adopted that includes the effects of residual velocity and penetration depth. The thickness and weight of the target are also taken into account in this optimization scheme. Target materials are selected as Armox 500T, Ti-6Al-4V, and Al-2024. Layered hybrid 5.5 mm Armox 500T, 8.5 Ti-6Al-4V, and 13 mm Al-2024 hybrid configuration is found to be superior.

1.2 Shaped Charge

A shaped charge is an explosive device that is commonly used in the military and defense industries, as well as civil applications such as metal cutting and oil well completion, etc. A shaped charge is typically an explosive-filled cavity with a metal liner on top and a detonator at the bottom. The process of shaped charge impact can be simplified into 3 stages as detonation, jet formation, and penetration as illustrated in Figure 1.5. When the explosive material is triggered, it detonates and forms a high-pressure shock wave. As a result, a high-velocity jet is formed which then crushes the metal liner. The liner takes the shape of a projectile and penetrates the target. Extremely high pressures are produced during the detonation and formation of the jet. The generated pressure becomes greater than the yield strength of the metal liner with highly elevated surface temperatures. Thus, the metal liner behaves almost fluid-like. However, the ballistic efficacy of explosively formed projectile (EFP) is completely governed by their kinetic energy rather than their thermal effects. The velocity of the tip of the jet can exceed Mach 25 (see [52]). Nevertheless, the process does generate a lot of heat and it has a significant damaging effect after penetration. Thus explosives with shaped charge technology are shown to be effective at disarming heavily armored vehicles or buildings.

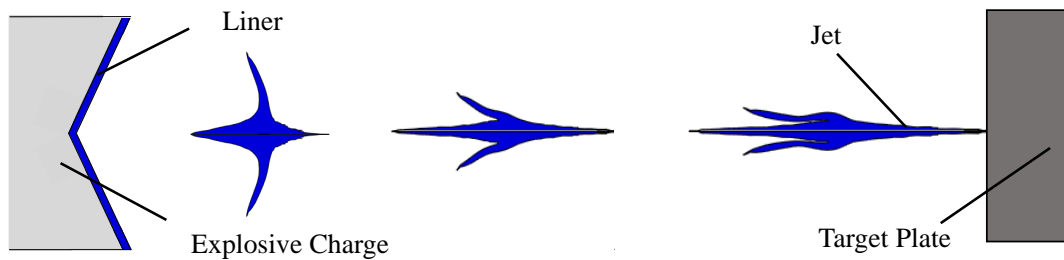


Figure 1.5: Illustration of shaped charge impact process.

The effectiveness of the shaped charge impact depends on several design parameters and it has been investigated through experimental studies. The liner, which is the main penetrator in shaped charge, is made up of metal materials with geometries varying from conical to bowl-type structures [53, 54, 55, 56, 57]. Copper has been utilized as liner material primarily [55, 58, 59, 60] while several other metals such as aluminum and steel alloys have been employed as well [61, 62, 63, 64]. In terms of penetration depth, copper has been found to be superior to other materials. In addition, multi-layered [65, 66] or tronconical liners [67, 68, 69] have been investigated due to their performance increase in the jet formation and jet velocity. The shape of the liner has a strong influence on the penetration depth and diameter [59, 61, 64, 70]. In recent applications, annular-shaped liners are employed to increase the penetration hole diameter [57, 71, 72].

Projectiles formed by a shaped charge are effective on metal armor used for military vehicles as well as concrete structures such as airport runways or shelters. Ballistic performance of EFP is demonstrated with experiments for target plates made up of copper, steel, and titanium alloys [73, 74] and concrete walls [60, 61, 64]. Furthermore, layered armors with multiple materials with stacked or spaced configurations are widely investigated against EFPs [60, 64, 75, 76, 77] where spaced configurations are found to have better protection performance than stacked ones. Due to the endless combinations of shaped charge process parameters or target configurations, numerical methods are employed to optimize the impact performance and reduce experimental costs.

Numerous studies have successfully used the FE method to simulate shaped charge impact experiments. A common approach for modeling detonation and formation

stages, employs an equation of state (EOS) shock model for the metal liner, while the Jones-Wilkins-Lee (JWL) EOS model is used for the explosive. JC plasticity model is widely utilized at the penetration stage since it incorporates strain rate and temperature effects. In [65, 78], the jet formation and penetration diameter and depth are successfully modeled with FE analysis. JC plasticity and the EOS model are employed to model the metal liner and target. In [79, 80] followed a similar modeling approach but only used EOS to describe the behavior of the metal liner assuming a fluid-like behavior of the formed jet. The impact of EFP on the target is mostly described only with a plasticity model for metal targets lacking any relevant fracture criteria. A limited number of works [55, 56, 81, 82] include stress, plastic strain, and strain rate-based damage model to simulate failure. These models are commonly utilized for ballistic impact with conventional projectiles but are not widely adopted for shaped charge impact.

Many numerical challenges arise in the modeling of the shaped charge impact process due to the large plastic deformations which lead to extreme mesh distortion. To overcome this problem meshless methods have been adopted in the literature. In [81, 83] SPH and SPH-FE coupled approaches are employed to simulate shaped charge impact and their results are validated with experiments. Another solution to the mesh distortion problem is Arbitrary Lagrangian-Eulerian (ALE) approach (e.g.[84, 85]). The mesh on the moving domain boundaries may move in tandem with the material, and the mesh of the moving domain relocates to optimize element geometry. Another approach is to model the stages of shaped charge impact separately. It is discussed that the final shape of the formed jet can be treated as a rigid body due to its high speed [86]. In [87] the EFPs are treated as blunt projectile samples with different diameters and lengths. Similarly in [88] simplified projectile geometries are utilized and compared with the real EFP shapes. It is stated that penetrations of the simulated EFP and the real EFP are remarkably similar.

1.3 Aim of The Study

This thesis aims to investigate the behavior of metal targets subjected to ballistic and shaped charge impact, utilizing numerical simulations with FE and SPH methods.

The study includes a thorough examination of various modeling approaches and damage models for a range of configurations, and the outcomes are confirmed by available experimental tests from the literature. The methods and constitutive relations utilized in the numerical analysis are extensively discussed in Chapter 2, providing a comprehensive understanding of the simulation approach employed in this research.

In Chapter 3, the effects of projectile nose shape, the thickness of the target plate, and the angle of the impact on ballistic impact. This study uses the JC plasticity model to define yield stress. JC and strain rate-dependent MMC models are used for failure predictions. The MMC damage model is implemented in a user-defined field (VUSDFLD), and for the JC model, the built-in framework is used in ABAQUS/Explicit. Using these two damage criteria, ballistic impact simulations are performed using FE and SPH methods. Ballistic impact simulations are conducted for 2024-T351 aluminum alloy targets with blunt, hemispherical, and ogival nose shapes at 3 mm, 6 mm, and 9.94 mm thicknesses, with an initial velocity of 100 to 400 m/s. The results from the numerical simulations are compared and discussed with the experimental data in [38].

Moreover, in Chapter 4, the ballistic response of Armox 500T steel is examined numerically using the JC and MMC damage models on commercial FE software ABAQUS/Explicit [89]. Effects of projectile nose shape, the thickness of the target plate, and the impact angle are investigated and the effect of Lode parameter incorporation is discussed in detail. Due to the lack of an available damage model that includes the Lode angle for Armox 500T steel, MMC model parameters are calibrated using tensile test data presented in [90]. In the aforementioned study, data for material testing are provided at every instant, however, damage model parameter calibration is not performed. JC damage model is also calibrated with these data in order to assess the necessity of a more complex failure prediction for ballistic impact performance. The strain rate effect on damage models is further discussed. Calibrated damage models are compared and validated using Armox 500T impact tests from [91]. The ballistic performance of the Armox 500T steel target is investigated using JC and MMC damage models employing 7.62 API, hemispherical, and blunt nose-shaped projectiles with target thicknesses ranging from 2 mm to 10 mm. The impact velocity range of the projectiles is 400 m/s to 1200 m/s. Furthermore, impact

angles of 0° , 15° , 30° , 45° , and 60° are examined.

Chapter 5 is concerned with the numerical modeling of both jet formation and penetration processes through FE and SPH methods emphasizing the accuracy of the numerical procedures. Copper and iron liners with conical and bowl-shaped geometries are investigated numerically. Results are validated with the published experimental data [55] for the available geometries. A separated modeling strategy is followed for the formation and penetration of the projectile. Detonation and formation of the jet are modeled with 2D axisymmetric elements in commercial finite element software ABAQUS/Explicit [89]. The exact shape of the EFP is extracted just before it contacts the target. Then it is modeled separately as a 3D rigid body to simulate the penetration process. The advantages and shortcomings of assuming rigid EFPs are discussed in the context of shaped charged impact. Moreover, impact performance is studied with varying liner geometries for conical and bowl-shaped liners. #45 and Armox 500T steels are employed as target materials. JC damage criterion and yield function are used to define deformation and failure behavior of targets where the model parameters are retrieved from [55, 92] for #45 steel and [91] for Armox 500T. A comprehensive numerical investigation is performed for a common armor material, Armox 500T, targets against EFPs which has been lacking in the literature. Impact angle and maximum penetration depth are studied for different liner geometries. In addition to the FE analysis, the SPH method is used for the penetration simulations and compared with the FE method. Their performance in predicting residual velocity and the failure mode is discussed in detail. Finally, Chapter 6 provides a conclusion to the thesis along with some thoughts about future work.

CHAPTER 2

NUMERICAL METHODS

This chapter provides a detailed explanation of the methods used in modeling of ballistic and shaped charge impact simulations. Various methods that are used to simulate ductile failure due to the impact of shaped and ballistic charges are discussed. Throughout this study, an uncoupled approach is adopted. Numerical modeling is conducted using FE and SPH methods. The discussion begins with the stress states included within the failure models. The plasticity and damage models are then described. The equation of state that is used for explosives and metal liners in shaped charge impact simulations is covered, next. Furthermore, the FE modeling details are thoroughly explained in the relevant chapters. Finally, the formulation of the SPH method is discussed, providing an overview of the methodology used in the simulations.

2.1 Stress states

Deformation and ductile failure of metals are significantly influenced by the stress states (e.g. stress triaxiality (η), Lode angle parameter ($\bar{\theta}$), etc.). Different non-dimensional parameters are incorporated into the plasticity or damage models depending on the dominant stress state. Stress triaxiality is defined as the ratio of hydrostatic stress to von Mises equivalent stress. It offers information regarding a material's deformation behavior under various loadings. A material with high triaxiality is subjected to high pressure, whereas a material with low triaxiality is subjected to less pressure and more shear stresses. Stress triaxiality is negative in compression, positive in tension, and $1/3$ in uniaxial tension. Moreover, the stress triaxiality value

is 3 at sharp corners like cracks. Consequently, even though two different specimens undergo the same tension test and have the same triaxiality value, they may fail in different ways. Stress triaxiality changes with the notch of the specimen. It is given as,

$$\eta = \frac{\sigma_h}{\sigma_{eq}} \quad (2.1)$$

where, the hydrostatic stress is shown as,

$$\sigma_h = \frac{I_1}{3} \quad (2.2)$$

in which I_1 is first stress invariant, $I_1 = \sigma_{11} + \sigma_{22} + \sigma_{33}$

Von Mises equivalent stress, σ_{eq} , is,

$$\sigma_{eq} = \frac{1}{\sqrt{2}} \sqrt{(\sigma_1 - \sigma_2)^2 + (\sigma_2 - \sigma_3)^2 + (\sigma_3 - \sigma_1)^2} \quad (2.3)$$

where σ_1 , σ_2 and σ_3 are the principal stresses.

In low stress triaxialities, the Lode angle parameter is crucial. To distinguish between the various shear stress states in three dimensions, the Lode angle parameter, which is a function of the third invariant of the stress deviator, is used. The Lode angle parameter is shown as,

$$\bar{\theta} = 1 - \frac{6\theta_L}{\pi} \quad (2.4)$$

where Lode angle, θ_L , is described as

$$\theta_L = \frac{1}{3} \arccos \left(\frac{J_3}{2} \left(\frac{3}{J_2} \right)^{3/2} \right) \quad (2.5)$$

in which J_2 and J_3 are the second and third deviatoric stress invariants, respectively, and they are expressed as,

$$J_2 = \frac{1}{2} \boldsymbol{\sigma}' : \boldsymbol{\sigma}', \quad J_3 = \det(\boldsymbol{\sigma}') \quad (2.6)$$

Geometrical illustration of Lode angle is shown in Figure 2.1. The angle between O'A and O'P in a deviatoric plane is the Lode angle, where P represents the stress state and A is the pure shear condition. The range of Lode angle is $0 \leq \theta \leq \pi/3$ whereas the range of Lode angle parameter is $-1 \leq \bar{\theta} \leq 1$. $\bar{\theta} = -1$ at equi-biaxial tension or uniaxial compression, 0 at pure shear and 1 at uniaxial tension.

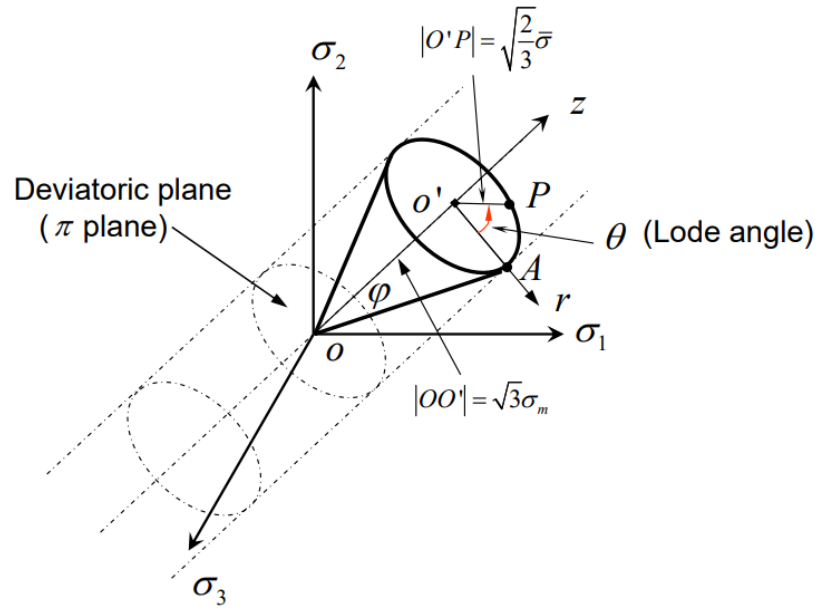


Figure 2.1: Geometrical illustration of Lode angle. [93]

2.2 Plasticity

When subjected to an external force or stress, the property of a material that allows it to undergo permanent deformation without fracturing or breaking is referred to as "plasticity". When a material is subjected to a load or stress, it may initially deform elastically, which means that when the stress is removed, the material will return to its original shape. However, the material will begin to experience plastic deformation if the stress or load exceeds its yield strength. Parameters that influence the plastic behavior of the material are incorporated through a yield function which is used in numerical analyses. The yield criterion can be described as,

$$\phi = \sigma_{eq} - \sigma_y = 0 \quad (2.7)$$

where σ_{eq} is the von Mises equivalent stress and σ_y is the yield stress. For $\phi < 0$ elastic deformation occurs and for $\phi = 0$ plastic deformation occurs. The condition mentioned is applicable to deviatoric plasticity models.

The von Mises plasticity is described in terms of the second deviatoric stress invariant, hence it is also referred to as " J_2 plasticity". The von Mises equivalent stress (Eq. 2.3) can be written in terms of J_2 as,

$$\sigma_{eq} = \sqrt{3J_2} \quad (2.8)$$

By substituting J_2 into Eq. 2.8,

$$\sigma_{eq}^2 = \frac{1}{2}[(\sigma_{11} - \sigma_{22})^2 + (\sigma_{22} - \sigma_{33})^2 + (\sigma_{33} - \sigma_{11})^2 + 6(\sigma_{12}^2 + \sigma_{23}^2 + \sigma_{31}^2)] \quad (2.9)$$

In terms of deviatoric stress, s , Eq. 2.9 can be written as,

$$\sigma_{eq}^2 = \frac{3}{2}s_{ij}s_{ij} \quad (2.10)$$

The von Mises yield surface is illustrated in Figure 2.2. A cylinder with a radius of $\sqrt{\frac{2}{3}}\sigma_y$ is encircled by the von Mises yield surface around the hydrostatic axis.

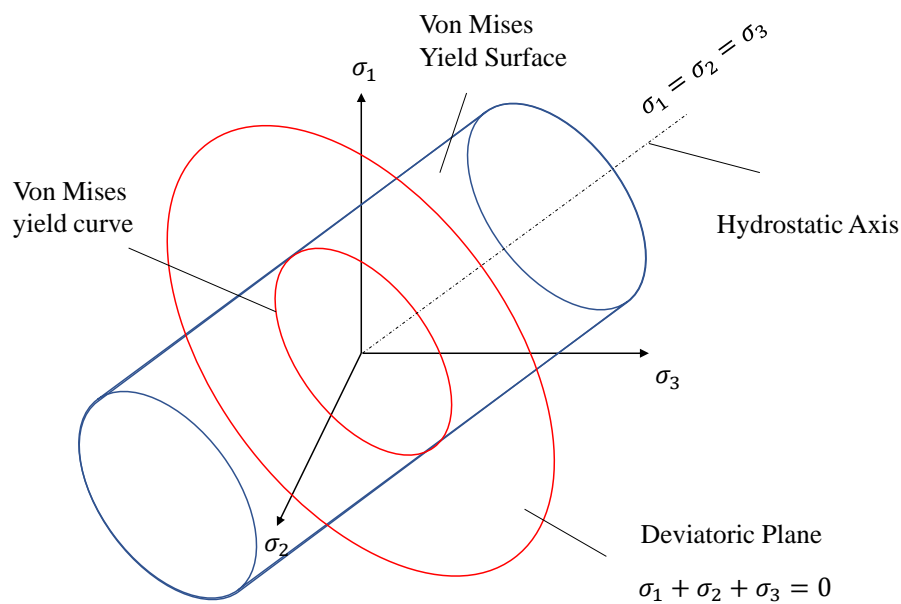


Figure 2.2: The von Mises yield surface.

Yield stress can be defined through various different functions such as JC plasticity model and Voce rule. JC model defines the nonlinear isotropic hardening of mate-

rials. JC is utilized, because in ballistic and shaped charge impact, the behavior of the materials are heavily influenced by the high strain rates, large strains and high temperature effects. In JC plasticity model yield stress is defined as,

$$\sigma_y = (A + B(\bar{\varepsilon}^p)^n)(1 + C \ln \dot{\bar{\varepsilon}}^*) (1 - T^{*m}) \quad (2.11)$$

where A , B , C and n are material constants, $\bar{\varepsilon}^p$ is the equivalent plastic strain. $\ln \dot{\bar{\varepsilon}}^*$ is defined as $\ln \dot{\bar{\varepsilon}}^* = \dot{\bar{\varepsilon}}/\dot{\varepsilon}_0$ in which $\dot{\bar{\varepsilon}}$ and $\dot{\varepsilon}_0$ represent plastic strain rate and reference strain rate, respectively. T^* is the homologous temperature and it is expressed as $T^* = (T - T_0)/(T_m - T_0)$ where T_m , T_0 and T are the melting temperature, room temperature, and the current temperature respectively.

The Voce rule is also used in this study. Since ballistic impact is a strain dependent process, strain rate effects are coupled as it is in JC model. The yield stress is formulated as,

$$\sigma_y = [\sigma_{y0} + q_1(1 - \exp(-q_2\varepsilon_{eq}^p)) + q_3(1 - \exp(-q_4\varepsilon_{eq}^p))](1 + C \ln \dot{\varepsilon}_{eq}^*) \quad (2.12)$$

where σ_{y0} is the initial yield stress, ε_{eq}^p is the von Mises equivalent plastic strain and q_1 , q_2 , q_3 , q_4 are material constants.

JC plasticity model is available in the ABAQUS software and it is used in Chapters 3 and 5. However, the Voce law equation is implemented using a user-defined subroutine (VUHARD) in Chapter 4. The current state of the model's variables is calculated by VUHARD using an explicit integration scheme. The constitutive model and its derivatives, as well as material parameters are required to implement the VUHARD subroutine.

2.3 Damage Models

The failure behavior of materials under various loading conditions is simulated in the current study using two different uncoupled damage models in ABAQUS. In uncoupled damage models, the effect of damage parameter on the constitutive equations is neglected. The first damage model, known as the JC damage model, is a built-in feature in ABAQUS. This model is commonly used to simulate the evolution of damage in materials subjected to ballistic impact loads while accounting for the effects of

stress triaxiality and strain rate. In JC damage model fracture strain, ε_f , is expressed as,

$$\varepsilon_f = [D_1 + D_2 \exp(D_3 \eta)](1 + D_4 \dot{\varepsilon}_{eq}^*)(1 + D_5 T^*) \quad (2.13)$$

where D_1, D_2, D_3, D_4 and D_5 are the JC material constants.

The second damage criterion is MMC damage model which considers the effect of stress triaxiality and Lode angle parameter on the damage evolution of the material. However, ballistic impact is a strain rate and temperature dependent process. As a result, a slightly modified MMC damage model is adapted from [41], in which the strain rate and temperature effects are incorporated in the same manner as JC is. ε_f is defined as,

$$\varepsilon_f = \left\{ \frac{K}{\hat{C}_2} \left[\hat{C}_3 + \frac{\sqrt{3}}{2 - \sqrt{3}} (\hat{C}_4^* - \hat{C}_3) \left(\sec \left(\frac{-\bar{\theta}\pi}{6} \right) - 1 \right) \right] \times \left[\sqrt{\frac{1 + \hat{C}_1^2}{3}} \cos \left(\frac{-\bar{\theta}\pi}{6} \right) + \hat{C}_1 \left(\eta + \frac{1}{3} \sin \left(\frac{-\bar{\theta}\pi}{6} \right) \right) \right] \right\}^{1/n} \times (1 + D_4 \dot{\varepsilon}_{eq}^*)(1 + D_5 T^*) \quad (2.14)$$

$$\hat{C}_4^* = \begin{cases} 1 & -1 \leq \bar{\theta} \leq 0 \\ \hat{C}_4 & 0 < \bar{\theta} \leq 1 \end{cases} \quad (2.15)$$

where $\hat{C}_1, \hat{C}_2, \hat{C}_3, \hat{C}_4, K$ and n are the MMC fracture criterion constants.

MMC is implemented in ABAQUS through a user-defined field (VUSDFLD). During the solution process, ABAQUS calls the VUSDFLD subroutine. VUSDFLD uses the stress data from ABAQUS to calculate the stress triaxiality and Lode angle parameter. Damage accumulation is then determined using the failure model. Evaluation of damage, D , is calculated by using the following formulation:

$$D = \int_0^{\bar{\varepsilon}^p} \frac{d\varepsilon_{eq}^p}{\varepsilon_f}. \quad (2.16)$$

The initial value of D is set to zero ($D = 0$), meaning the material is undamaged when the simulation begins. Throughout the analysis, the summation is done over all

of the increments as shown in Equation 2.17. When $D = 1$, the material is considered to have failed, and the element is deleted.

$$D = \sum \frac{\Delta \varepsilon_{eq}^p}{\varepsilon_f} \quad (2.17)$$

2.4 Equation of State (EOS)

EOS is used to describe the material behavior of shock-compressed solid metal and high explosive that are used in the shaped charge process. The shaped charge process is further discussed in Chapter 5. In this section, Hugoniot-based Mie-Grüneisen and The Jones-Wilkins-Lee (JWL) EOS are explained.

Shock waves depict a rapid transition between states. Mass, momentum, and energy are conserved throughout the shock waves. The relationships derived from these conservation equations are known as Rankine-Hugoniot relationships, as demonstrated as follows,

$$P_1 - P_0 = \frac{U_s U_{p1}}{\rho_0} \quad (2.18)$$

$$E_1 - E_0 = \frac{1}{2}(P_1 + P_0)(\rho_0 - \rho_1) \quad (2.19)$$

$$\frac{U_s - U_{p0}}{\rho_1} = \frac{U_s - U_{p1}}{\rho_0} \quad (2.20)$$

where U_s is the linear shock velocity, P_0 and P_1 are the pressure in two regions, U_{p0} and U_{p1} are the particle velocities, ρ_0 and ρ_1 are the density of upstream and downstream of the wave. Values of P_0 , E_0 and U_{p0} are zero along the principle Hugoniot. Initial value of ρ_0 is known. Hence, in these three equations there are four unknowns which are U_p , U_s , P and ρ_1 . A fourth equation is necessary to solve for the shock state. A common linear relationship between U_s-U_p is utilized for this reason and it is expressed as,

$$U_s = c_0 + sU_p \quad (2.21)$$

where s is a material parameter and c_0 is the bulk speed.

In order to define the equation of state of the metal liners, Mie-Grüneisen EOS is utilized. It can be expressed as:

$$p - p_H = \Gamma\rho(E_m - E_H) \quad (2.22)$$

where ρ is the current density and Γ is the Grüneisen ratio and it is expressed as $\Gamma = \Gamma_0(\rho_0/\rho)$. In which ρ_0 is reference density, Γ_0 is a material constant, E_m is the internal energy per unit mass and p_H is Hugoniot pressure which is formulated as,

$$p_H = \frac{\rho_0 c_0^2 \varsigma}{(1 - s\varsigma)^2} \quad (2.23)$$

The relationship between p_H and Hugoniot energy, E_H , which is the specific energy per unit mass, can be described as,

$$E_H = \frac{p_H \varsigma}{2\rho_0} \quad (2.24)$$

where $\varsigma = 1 - \rho_0/\rho$, ς is the nominal volumetric compressive strain. Coupled equations for pressure and internal energy are represented by the equation of state and energy equations. At each material point, these equations are simultaneously solved by ABAQUS/Explicit.

In the modeling of explosive charge JWL EOS is used. JWL high explosive equation of state calculates the pressure that is created by the chemical energy released in an explosive. The formulation of JWL is shown as follows,

$$p = A' \left(1 - \frac{\omega\rho}{R_1\rho_0}\right) \exp\left(-R_1 \frac{\rho_0}{\rho}\right) + B' \left(1 - \frac{\omega\rho}{R_2\rho_0}\right) \exp\left(-R_2 \frac{\rho_0}{\rho}\right) + \frac{\omega\rho^2}{\rho_0} E_{m_o} \quad (2.25)$$

where A' , B' , R_1 , R_2 and ω are material constants. E_{m_o} is the energy per unit mass. ρ_0 and ρ are the density of the explosive and the density of products of detonation, respectively.

2.5 SPH method

Large deformations in the impact process cause mesh distortion in FE simulations. In the literature, meshless techniques have been used to address this issue. SPH is a

fully Lagrangian mesh-free method available within the ABAQUS software package. Instead of elements and nodes in the FE approach, particles are used in this method. Visual representations of the SPH method and FE methods are shown in Figure 2.3.

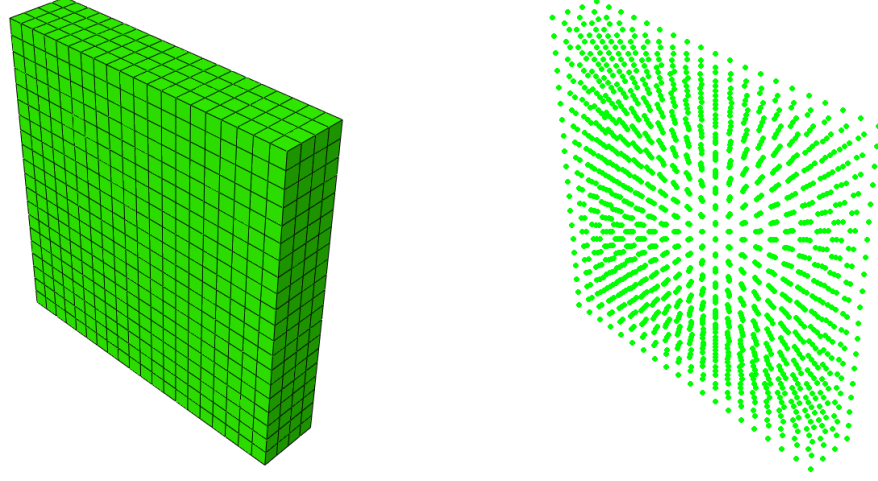


Figure 2.3: Visual representation of FE (left) and SPH (right) methods.

In ABAQUS/Explicit, the SPH method is utilized as a built-in framework. Instead of calculating nodal displacements by solving residual forces through element volume integration, SPH connects particles using a weighting function. Conservation equations are satisfied around a given point by using a weighting function. This is calculated by arbitrary function $f(x)$ as,

$$f(x) = \int f(x')W(x - x', h)dx' \quad (2.26)$$

where W is the kernel function, x is the position of the particle and h is the smoothing length which indicated the number of particles that affect the interpolation for a particular point. ABAQUS/Explicit automatically determines h at the start of the analysis, aiming for an average particle count per element ranging from 30 to 50. h remains constant throughout the analysis. Moreover, the kernel function must satisfy the following conditions,

$$\lim_{h \rightarrow 0} W(x - x', h) = \delta(x - x') \quad (2.27)$$

$$\int W(x - x', h)dx' = 1 \quad (2.28)$$

where δ is the Dirac delta function. One crucial characteristic of the smoothing function used for particles in SPH is that it must decrease monotonically as the distance from the particle increases. This behavior reflects the physical intuition that closer particles should have a more significant impact on the particle being considered.

There are many kernel functions such as cubic, quadratic and quintic functions. In the context of this thesis cubic kernel function is used. The cubic spline kernel is typically a better choice for highly time-dependent problems that occur over a short duration, such as the ballistic impact process [94]. This is because the cubic spline kernel provides better spatial resolution and smoother gradients, which is particularly useful for accurately capturing abrupt changes in the system behavior during these types of events. The cubic spline kernel function is expressed as,

$$W(x - x', h) = \frac{1}{h^3\pi} \begin{cases} 1 - \frac{3}{2}\xi^2 + \frac{3}{4}\xi^3, & \text{for } 0 \leq \xi \leq 1; \\ \frac{1}{4}(2 - \xi)^3, & \text{for } 1 \leq \xi \leq 2; \\ 0, & \text{for } \xi > 2, \end{cases} \quad (2.29)$$

where $\xi = \frac{x}{h}$. When using the cubic spline kernel in SPH, only particles that lie within twice the smoothing length of the particle being evaluated are included in the calculations. This approach helps to limit the computational cost by reducing the number of particles that need to be considered while still maintaining sufficient accuracy in the results. The visual representation of the cubic spline kernel function is illustrated in Figure 2.4. During the computations in SPH, only the particles that are located inside the designated domain (shown in black) are taken into account, while particles outside of the domain (shown in white) are not considered.

In order to estimate a field variable at any point in a domain, SPH employs an evolving interpolation. Approximation of the value of a variable at a particle of interest is calculated by adding up the contributions made by a set of nearby particles, represented by the subscript j , and can be shown as follows,

$$f(x) \simeq \sum_{j=1}^N \frac{m_j}{\rho_j} f_j W(|x - x_j|, h) \quad (2.30)$$

where ρ_j is the density, m_j is the mass and f_j is the field variable of the j th particle. When applying SPH, it is necessary to ensure that the conservation equations are met

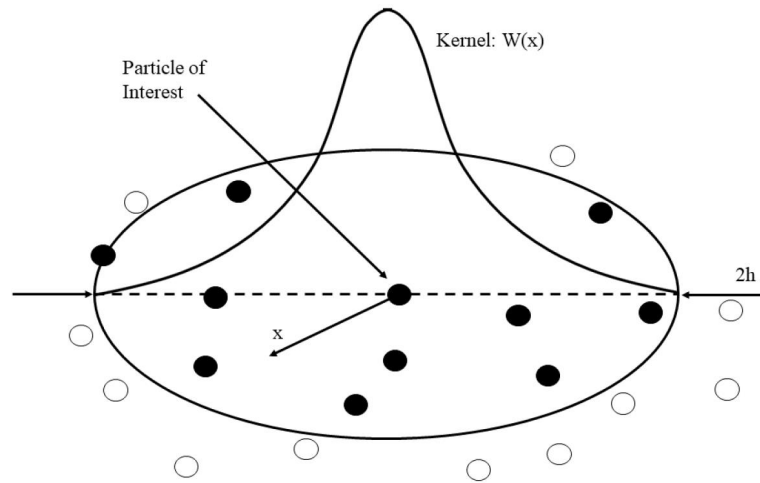


Figure 2.4: Visual representation cubic spline kernel function [94].

for each particle at every time increment. The field values obtained are updated and then used as the initial conditions for the next iteration. These updated values are carried forward to the next time step and the process is repeated until the simulation reaches its endpoint.

CHAPTER 3

NUMERICAL ANALYSIS OF BALLISTIC IMPACT THROUGH FE AND SPH METHODS

In this chapter, the effects of impact angle, target plate thickness, and projectile nose shape on ballistic impact are investigated. The target material is aluminum alloy 2024-T351 which is a ductile metal that is frequently utilized in the aerospace industry for ballistic impact tests. The behavior of the target plate is compared using JC and MMC damage by utilizing FE and SPH methods. The numerical model set-up is shown in Figure 3.1.

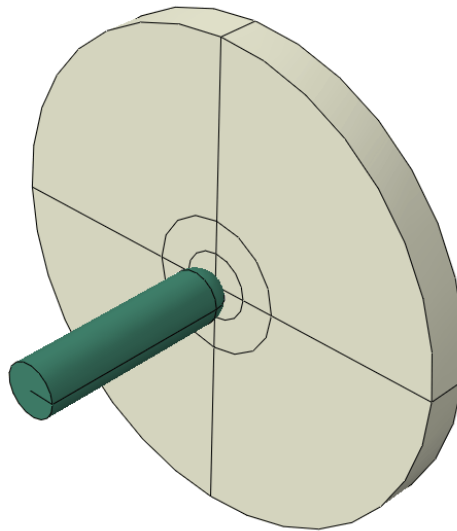


Figure 3.1: Numerical model set-up.

3.1 Material Parameters

Yield stress is defined using the JC plasticity model as shown in Equation 2.11. The material parameters of aluminum alloy 2024-T351 are presented in Table 3.1.

Table 3.1: Material parameters of aluminum alloy 2024-T351.

E(GPa)	ν	$\rho(g/cm^3)$	$\dot{\epsilon}_0^*(1/s)$	T_0 (K)	T_m (K)
72	0.3	2.77	8.336×10^{-4}	293	775
A(MPa)	B(MPa)	n	C	m	
235.7	377.5	0.1752	0.0146	1.7	

For damage criteria, JC and strain rate-dependent MMC models are used (see Equations 2.13 and 2.14). JC and MMC damage parameters for aluminum alloy 2024-T351 are shown in Table 3.2. Plasticity and damage parameters are retrieved from [38].

Table 3.2: JC and MMC fracture criteria constants for aluminum alloy 2024-T351.

D_1	D_2	D_3	D_4		
0.034	0.664	-1.5	0.011		
K (MPa)	\hat{C}_1	\hat{C}_2 (MPa)	\hat{C}_3	n	
678.7	0.104	335.6	1.036	0.138	

3.2 Numerical Modelling

The target is modeled as a deformable body in the numerical model, whereas the projectile is modeled as a rigid body. A reference point is attached to the nose tip of the projectile. The mass and velocity of the projectile are assigned through this

point. The projectile has a mass of 50 g and a diameter of 12.66 mm, and is studied in three different nose shapes: blunt, hemispherical, and ogival with an initial velocity ranging from 100 to 400 m/s. The geometry of projectiles and targets are presented in Figure 3.2. The target has a 116 mm diameter, and three thickness values are studied as 3 mm, 6 mm, and 9.94 mm. α is the impact angle and the assigned angles are 0° , 15° , 30° , 45° , and 60° .

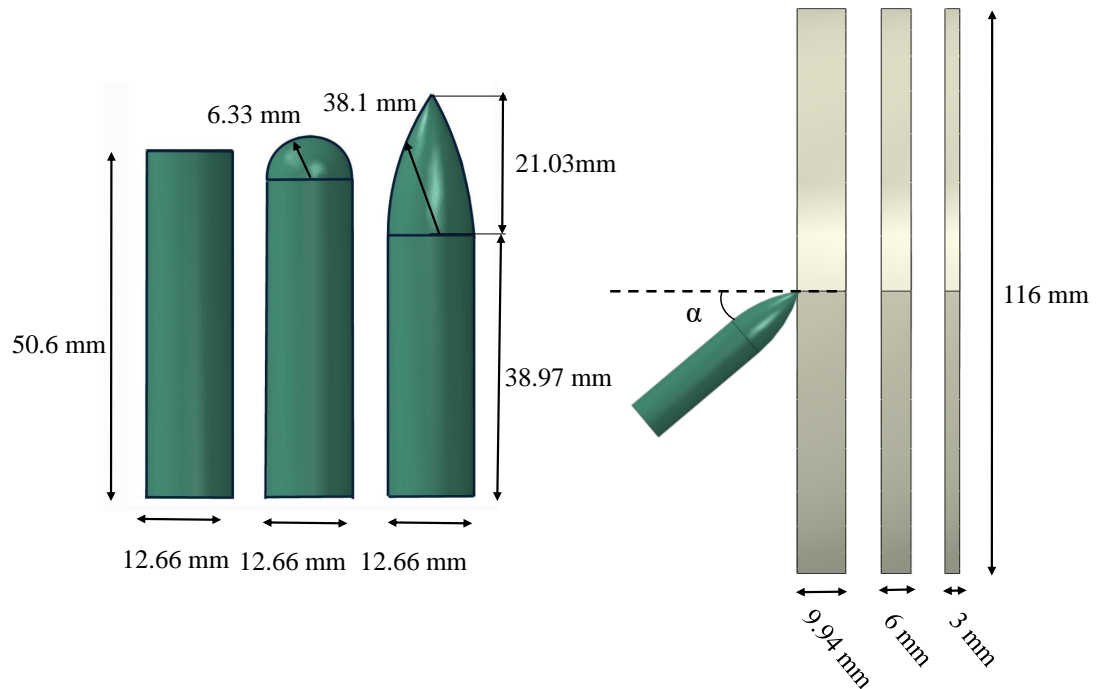


Figure 3.2: Geometry of the projectiles and targets

Simulations are conducted on one-fourth of the target plate. To accurately simulate the impact for the oblique impact simulations, half of the target plate is simulated. A study is carried out to demonstrate that the target can be modeled as a quarter or half portion without affecting the accuracy of the results. The initial velocity versus residual velocity curve of full, half, and quarter models is shown in Figure 3.3. A hemispherical projectile is used with 9.94 mm thick targets. The initial velocity of the projectile ranges from 250 m/s to 350 m/s. It can be seen that the difference between full, half, and quarter models are insignificant. The outer surface of the target is fixed. If the outer surface is not fixed, the target starts to bend outwards. Moreover,

for quarter and half models, the inner surfaces symmetry boundary conditions are applied. The interaction between the target and the projectile is defined as "hard" contact and friction is neglected. The surface of the projectile and the node region of the penetration zone of the target are selected when defining the interaction.

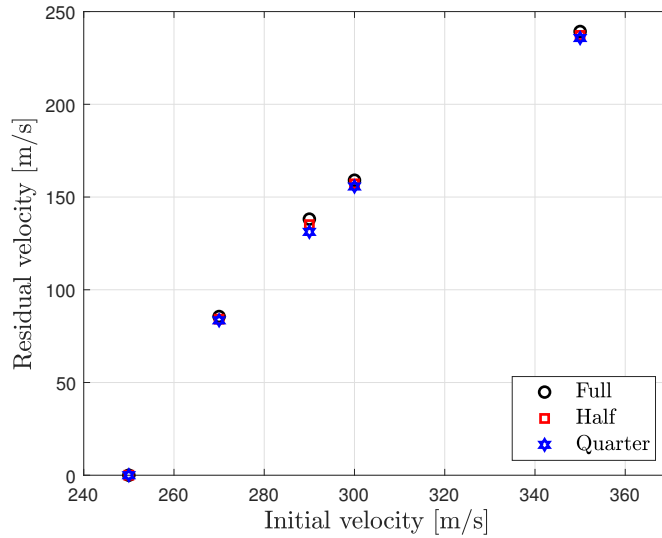
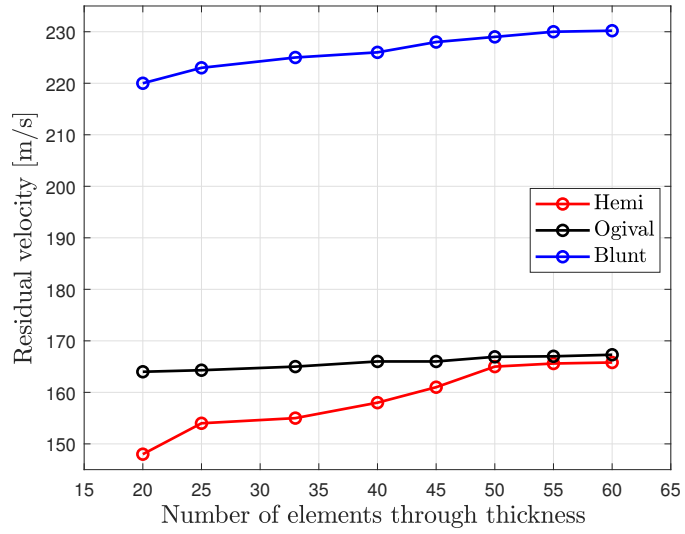


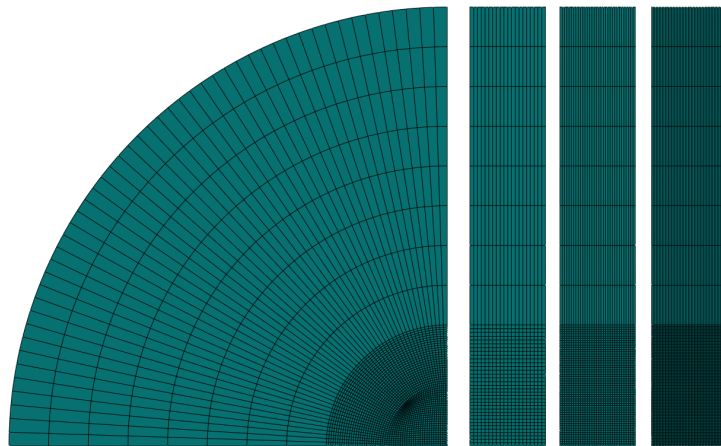
Figure 3.3: Initial vs. residual velocity curves of full, half and quarter models.

A mesh convergence study is conducted. In Figure 3.4a residual velocity values with varying the number of elements through the thickness from 20 to 60. A visual representation for number of elements through the thickness for 20,33 and 55 is shown in Figure 3.4b. This study is carried out with hemispherical, ogival, and blunt nose shapes with a 9.94 mm target plate, where the initial velocity of the projectile is 300 m/s. It is observed that the ogival nose shape is not as sensitive to the number of elements throughout the thickness. A similar trend is observed in [34] and it is stated that the dominance of plasticity in ogival nosed projectiles can be anticipated by larger elements. Greater numbers of elements through the thickness resulted in larger residual velocities for both hemispherical and blunt nose shapes. The number of elements through the thickness is chosen as 55. Additionally, the target is meshed with hexahedral linear elements with reduced integration (C3D8R). Penetration zone is partitioned in the FE model as shown in Figure 3.4b, and it is meshed finer than the outer surface.

However, in the SPH method partitioning the target results in the separation of the



(a) Mesh convergence results.



(b) Number of elements through the thickness for 20, 33 and 55.

Figure 3.4: Mesh convergence study.

partition boundaries. Hence, in SPH models, meshing is done with bias instead of partitioning which makes the mesh fine at the center and coarse towards the edge. After the mesh is assigned, the ABAQUS software uses the mesh as the orientation of the particles. Figure 3.5 illustrates the enlarged view of the particles of the target.

A mesh convergence study is also conducted for SPH simulations using hemispheri-

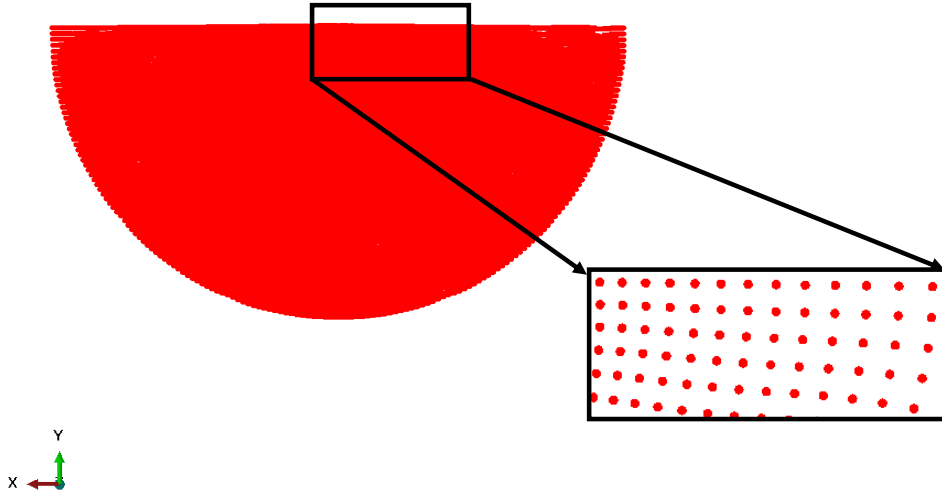


Figure 3.5: Enlarged view of the target for SPH simulations.

cal, ogival, and blunt nose shapes with a 9.94 mm target plate and an initial velocity of 300 m/s for the projectile. The effect of mesh size on residual velocity is investigated by varying the minimum element size from 0.2 mm to 0.5 mm as shown in Figure 3.6. When residual velocity results and computational cost are considered, the minimum mesh size for all projectiles is chosen to be 0.3 mm with hexahedral linear elements with reduced integration (C3D8R).

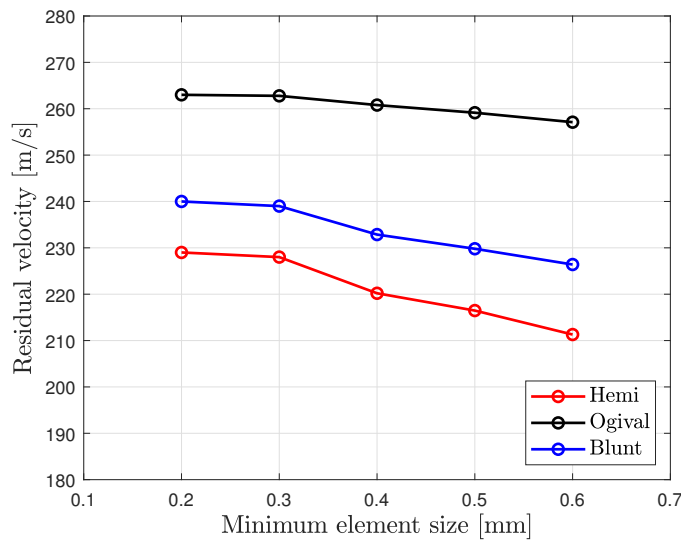


Figure 3.6: Mesh convergence study for SPH simulations.

The effect of mesh size on the failure mechanism is also investigated. Figure 3.7 illustrates a comparison of coarse and fine mesh and particle configurations for FE and SPH methods. A hemispherical projectile with a 9.94 mm target is used. The initial velocity of the projectile is 300 m/s. Despite the fact that their failure mechanisms appear to be the same, a fine configuration results in more detailed damage distribution for both methods.

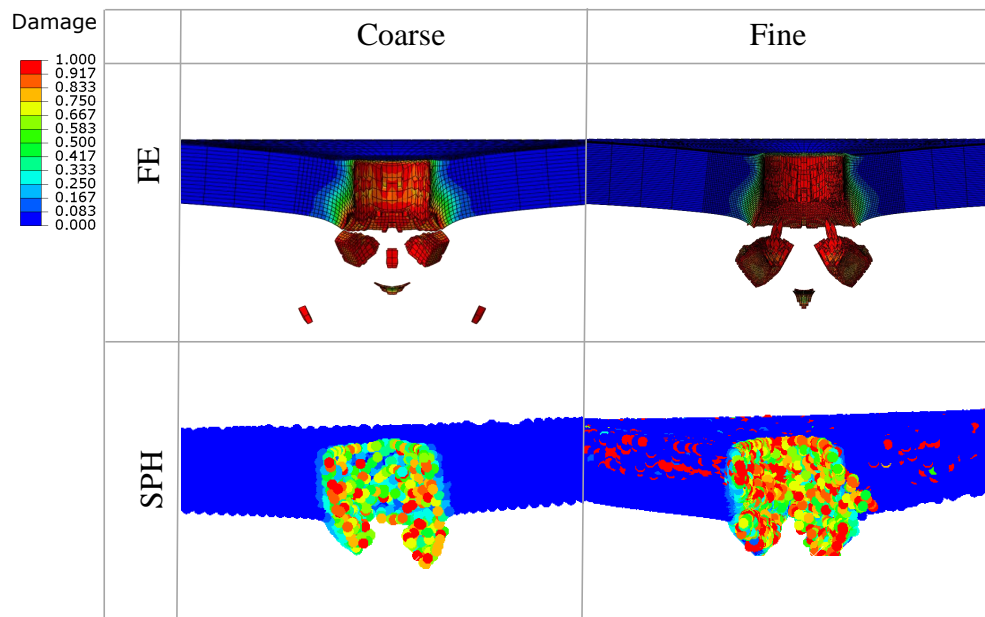


Figure 3.7: Comparison of coarse and fine configurations for FE and SPH methods.

To ensure the accuracy of simulation results, it is important to verify the conservation of energy in the simulations. For this purpose, kinetic energy, internal energy, hourglass energy, and total energy over the whole simulation time are shown in Figure 3.8. Conservation of energy is shown for a hemispherical projectile at 300 m/s initial velocity with a 9.94 mm thick target. Excessive distortion and deformation of elements within a system causes the generation of hourglass energy which is also known as artificial strain energy. The hourglass energy is observed to be less than 2% of the total energy during the impact process implying that hourglassing is not a problem. Damage dissipation energy due to element deletion is found to be insignificant (less than 1% of total energy).

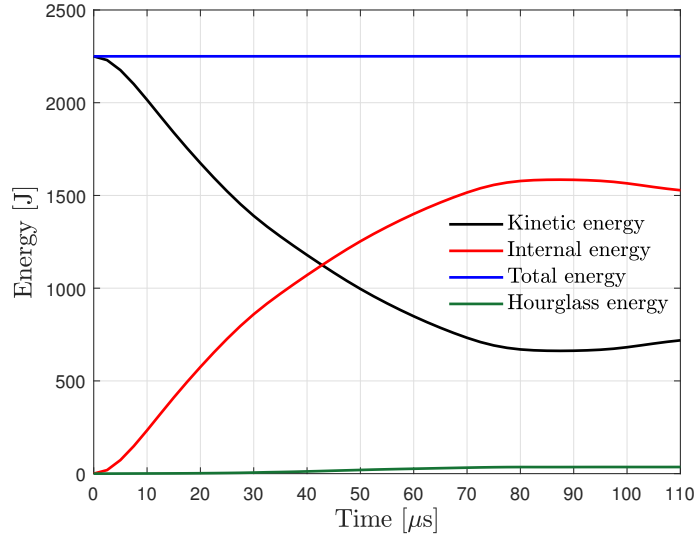


Figure 3.8: Energy time history of the target and projectile.

3.3 Results and Discussion

Figures 3.9, 3.10, and 3.11 demonstrate a comparison of FE and SPH approaches with JC and MMC damage models for hemispherical, blunt, and ogival projectiles. The effect of projectile nose shape on the relationship between initial and residual velocity is investigated. Initial velocities of the projectiles vary from 100 m/s to 400 m/s and the target thickness is 9.94 mm. It is observed that for all nose shapes, among all combinations of the methodologies, the velocity required to achieve a non-zero residual velocity is the highest for the FE-JC model. As the initial velocity increases, the residual velocity converges toward the experimental data for all three nose shapes. Furthermore, in all three nose shapes, it is observed that the FE-MMC model has the best and most consistent agreement with the experiment. Additionally, it has been noted that FE results seem to be more precise than SPH results.

At the target thickness of 3 mm, 6 mm, and 9.94 mm, a hemispherical projectile impacts the target. Simulations are carried out with three thicknesses with velocities ranging from 50 m/s to 350 m/s. The effect of changing the thickness of the target plate with an initial velocity of 250 m/s is shown in Figure 3.12. The results show that when the target thickness increases, the residual velocity of the projectile decreases. Additionally, the velocity needed to penetrate the target increases. At 9.94 mm thick-

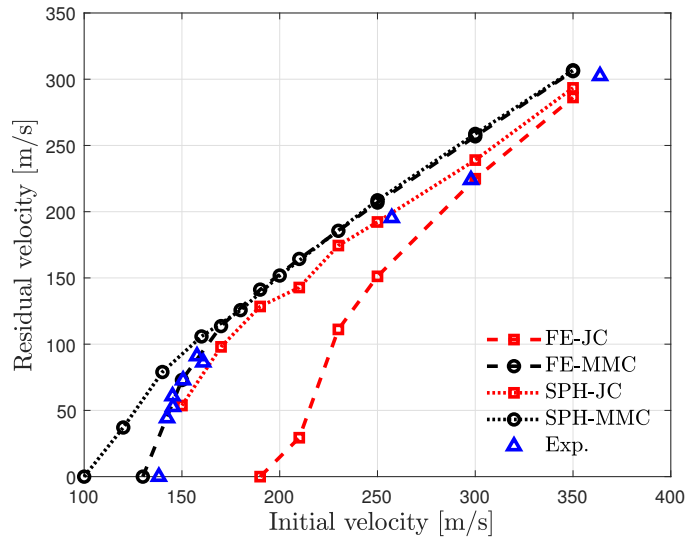


Figure 3.9: Initial vs. residual velocity curves of FE-JC, FE-MMC, SPH-JC, SPH-MMC models for blunt projectile at 9.94 mm target thickness. Experimental data from [38].

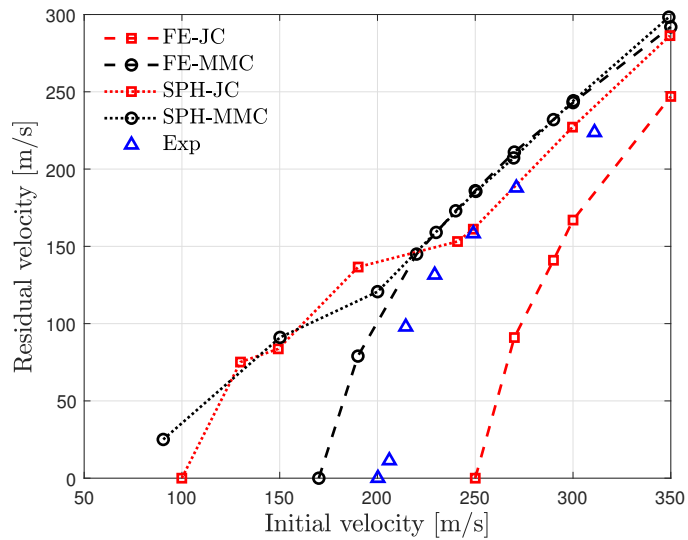


Figure 3.10: Initial vs. residual velocity curves of FE-JC, FE-MMC, SPH-JC, SPH-MMC models for hemispherical projectile at 9.94 mm target thickness. Experimental data from [38].

ness, the velocity required to penetrate the target is 170 m/s for FE-MMC, while at 6 mm thickness, the velocity needs to be 110 m/s to penetrate the target and for the 3

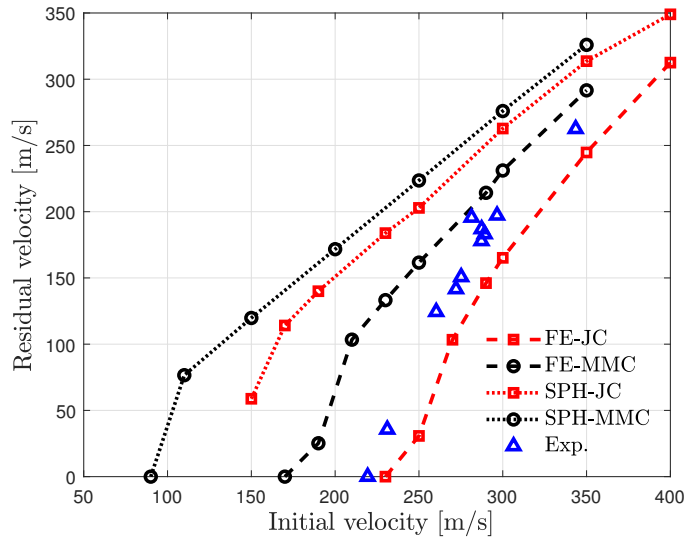


Figure 3.11: Initial vs. residual velocity curves of FE-JC, FE-MMC, SPH-JC, SPH-MMC models for ogival projectile at 9.94 mm target thickness. Experimental data from [38].

mm target the initial velocity has to be more than 70 m/s to penetrate the target. It is also observed that FE-MMC and SPH-MMC provide pretty comparable results. As the thickness increases, SPH-JC and FE-JC diverge. However, FE-JC differs from all other methodologies and the projectile does not penetrate the target at 9.94 mm.

The effect of impact angle is studied with 0° , 15° , 30° , 45° , and 60° obliquity. Figure 3.13 illustrates the relation between the impact angle and residual velocity for FE-JC and FE-MMC models. The initial velocity of the projectile is 350 m/s. Results show that when the obliquity increases, residual velocity decreases. The residual velocity difference is minimal for hemispherical and ogival projectiles with 0° , 15° , and 30° obliquity. However, the blunt projectile is sensitive to the change of impact angle. In the JC model, the residual velocity for blunt and hemispherical projectiles drops rapidly at the range of 45° and 60° obliquity. Moreover, for blunt projectiles, the drop in residual velocity for the JC model is roughly 30% and 13% for the MMC model. A similar pattern occurred for hemispherical projectiles, where JC and MMC reduce residual velocity by 31% and 12%, respectively. However, the residual velocity of the ogival projectile decreased by 10% and 7% in the JC and MMC models, respectively. In all three nose shapes, the residual velocities for JC models are significantly lower

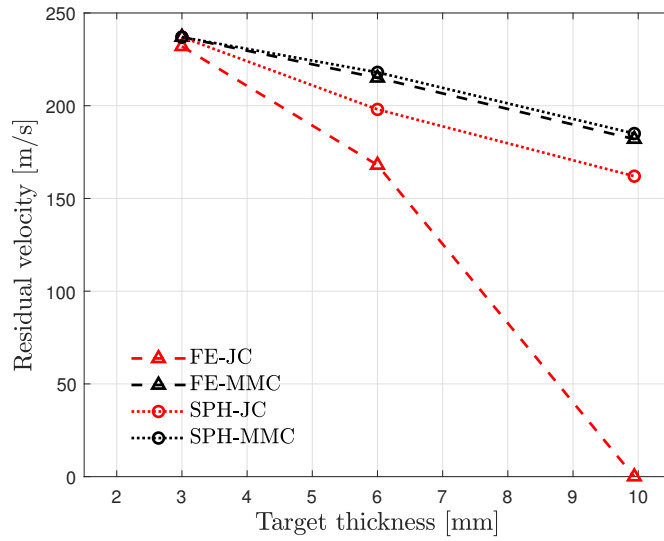


Figure 3.12: Target thickness-residual velocity curves of hemispherical projectile for FE-JC, FE-MMC, SPH-JC, SPH-MMC models at 250 m/s initial velocity with 3 mm, 6 mm, and 9.94 mm thicknesses.

for all angles than their MMC counterparts.

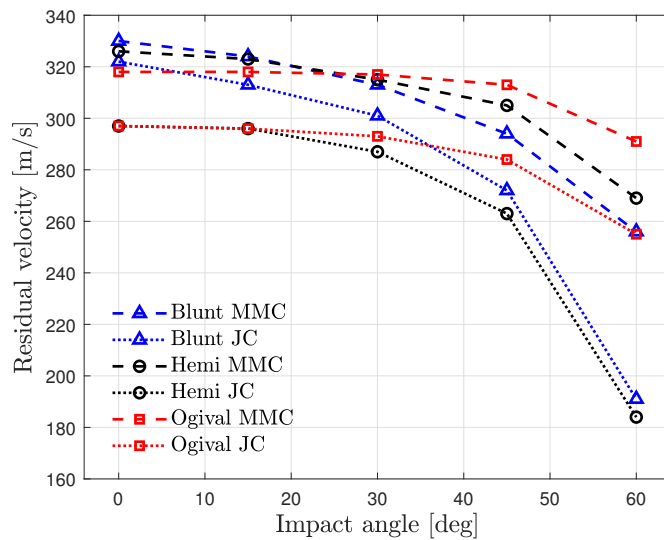


Figure 3.13: Impact angle-residual velocity curves of blunt, hemispherical, and ogival projectile for FE-JC and FE-MMC models at 350 m/s initial velocity with 6 mm thickness.

The failure mechanism of the target is investigated for three nose shapes at different

obliquity with FE-MMC and illustrated in Figure 3.14. The target's behavior changes as the nose shape and impact angle change. For the blunt projectile, from 0° to 30° obliquity, shear plugging is observed. As the impact angle increases from 30° to 60° obliquity, the created plug begins to shatter into little fragments. Additionally, for hemispherical projectiles at 0° , 15° and 30° obliquity shear plugging and fragmentation occur. As the obliquity increases the formed plug seems to crack into pieces. Hence the number of fragments increases as the impact angle increases. Further, for all three nose shapes as the angle increases the size of the generated hole increases as well.

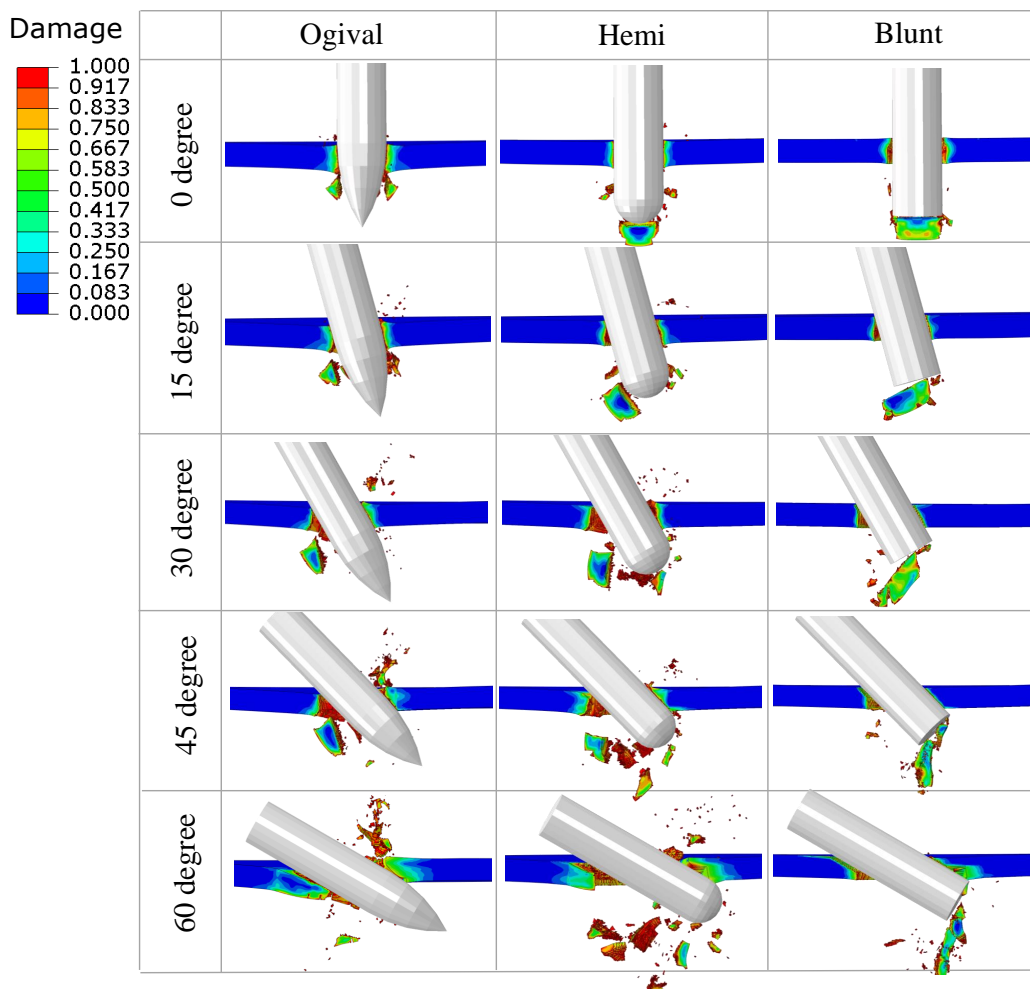


Figure 3.14: Failure mechanisms of blunt, hemispherical, and ogival projectile at 350 m/s initial velocity with 6 mm thickness for 0° , 15° , 30° , 45° , and 60° obliquity with FE-MMC.

The failure mechanism of the ogival projectile is investigated further. Figure 3.15 shows ogival projectile impacting the target plate with 0°, 15°, 30°, 45°, and 60° obliquity. The failure mechanism is investigated utilizing MMC-FE, MMC-SPH, JC-FE, and JC-SPH configurations. The initial velocity of the projectile is 350 m/s. For ogival nose shape, the dominant failure mechanism is ductile hole enlargement. It is observed in all of the methodologies. However, in some of the configurations other failure mechanisms occurred as well. For the JC-FE case as the impact angle increases, petaling is observed. Furthermore, as the impact angle increases, so does the size of the formed petal. In the MMC-SPH configuration, a similar pattern is observed in the JC-FE configuration. However, the formed petals are not as defined as in the JC-FE case. In MMC-FE configuration, at low impact angles, small-sized petals are observed. Nevertheless, as the impact angle increased the formed petal cracked into small pieces. Lastly, JC-SPH displayed very small petaling at obliquity from 0° to 45°. At 60° obliquity, very large plug-like cracks are observed.

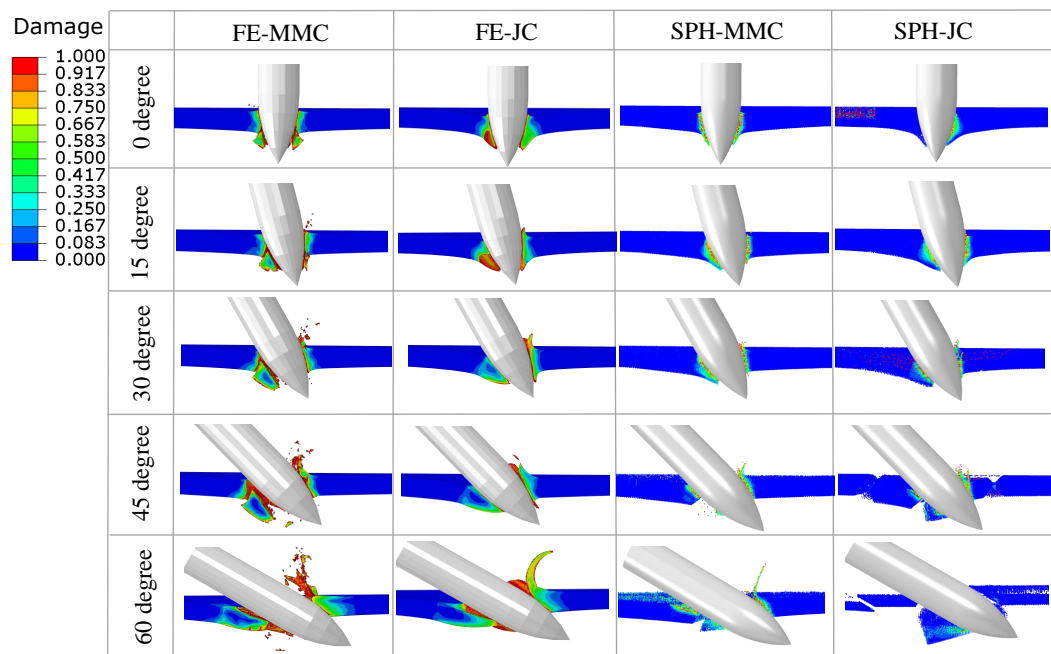


Figure 3.15: Failure mechanisms of 6 mm thickness ogival projectile at 350 m/s initial velocity with FE-JC, FE-MMC, SPH-JC, SPH-MMC for 0°, 15°, 30°, 45°, and 60° obliquity.

CHAPTER 4

A NUMERICAL BALLISTIC PERFORMANCE INVESTIGATION OF ARMOX 500T STEEL THROUGH DUCTILE DAMAGE MODELS

Armox 500T is very tough armor steel. It is critical to investigate armor steel failure in ballistic impact. It is discussed that the Lode parameter is an important factor in ballistic impact, but there is very little research available in the literature that considers the effects of the Lode parameter on armor steels. This chapter provides an in-depth investigation of the Armox 500T steel's material behavior and its application in ballistic impact. Material tests from the literature [90] are used to calibrate JC and MMC damage model parameters for Armox 500T steel. Then, using ballistic impact experiments from the literature [91], these parameters are validated. Additionally, JC and MMC damage models are compared by varying target thickness, projectile nose shape, and impact angle.

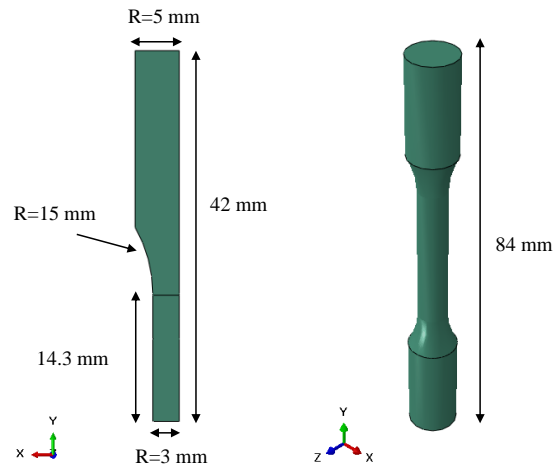
4.1 Numerical models and calibration

FE models and the calibration procedure for plasticity and damage models are explained in this section. The FE simulations are performed using ABAQUS/Explicit. The calibrated damage models are then validated and compared using the uniaxial tensile test data.

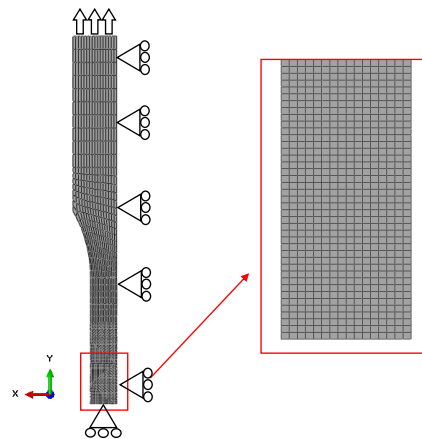
4.1.1 FE modeling of tensile tests

In [90], tension tests are conducted for thin double-grooved samples (referred to as 1.a-4.a), smooth/notched round bars (referred to as 5.b-10.b), thick double-grooved

samples (referred as 11.c–14.c). Shear and compression tests are also conducted and they are referred to as 15.d and 16.e, respectively. For smooth round bar specimen 5.b, a true stress-plastic strain curve is provided which we used to obtain the yield relation. The specimen geometry is shown in Figure 4.1a.



(a) Section view, 1/8 portion (left) and full scale (right) model of the specimen 5.b.



(b) Enlarged view of the fine meshed section of specimen 5.b.

Figure 4.1: Geometry (a) and boundary conditions (b) of specimen 5.b.

1/8 portion of the specimen is modeled in FE analysis to reduce computational time. The displacement boundary condition is applied to the top surface of the specimen. Symmetry boundary conditions are applied for the inner surfaces as shown in Figure 4.1b. A mesh convergence study is conducted using specimen 5.b. The element size

at the gauge length is investigated. The Voce law is used to define material properties (see Equation Equation 2.12) and the material parameters are tabulated in Table 4.1. Force versus gauge length elongation curve for varying element sizes is shown in Figure 4.2. The minimum element size varied from 0.09 mm to 0.06 mm. It is found that convergence is achieved at 0.07 mm; therefore, this element size is used for simulations of all other tensile tests. Mesh is finer at the gauge length and becomes coarser as illustrated in Figure 4.1b. The model is meshed with hexahedral linear elements with reduced integration (C3D8R). The gauge length is 28.6 mm. Force is measured from the nodes on the top surface and displacement is measured from a node at the center of the specimen and at the end of the gauge section in the FE simulations.

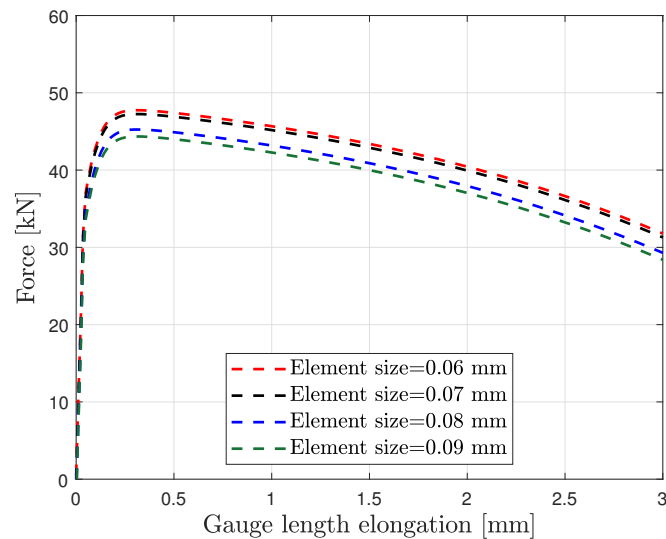


Figure 4.2: Force vs. gauge length elongation curve with varying element sizes for specimen 5.b.

Force versus gauge length elongation curve for 1/8 portion and full-scale specimens with experimental data are shown in Figure 4.3 and it demonstrates that they produce the same outcomes.

In order to test damage models, 3 more specimens with different ranges of Lode angle parameter and triaxiality are simulated. A quarter of specimens 2.a and 12.c, as well as 1/8 of specimen 8.b, are modeled as shown in Figure 4.4. Specimens 2.a and 12.c have thicknesses of 1 mm and 12 mm, respectively. These specimens are modeled

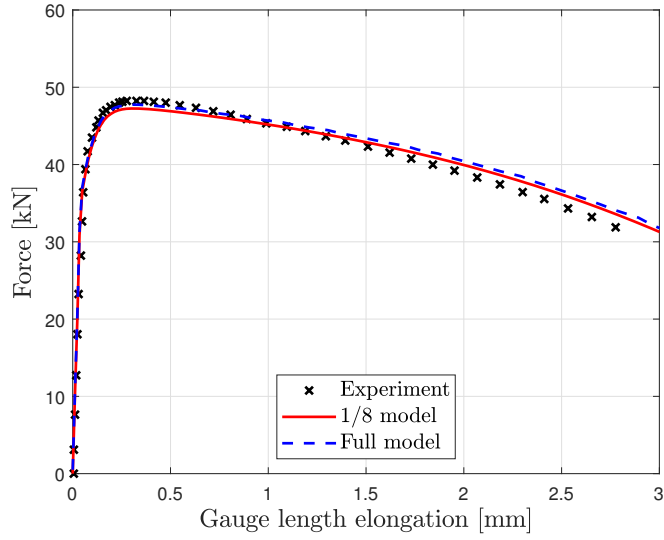


Figure 4.3: Force vs. gauge length elongation curve for an eighth and full scale specimens

in the same way as specimen 5.b, as described previously. The gauge lengths of specimens 8.b 2.a and 12.c are 10.96 mm, 23.74 mm, and 15.80 mm respectively.

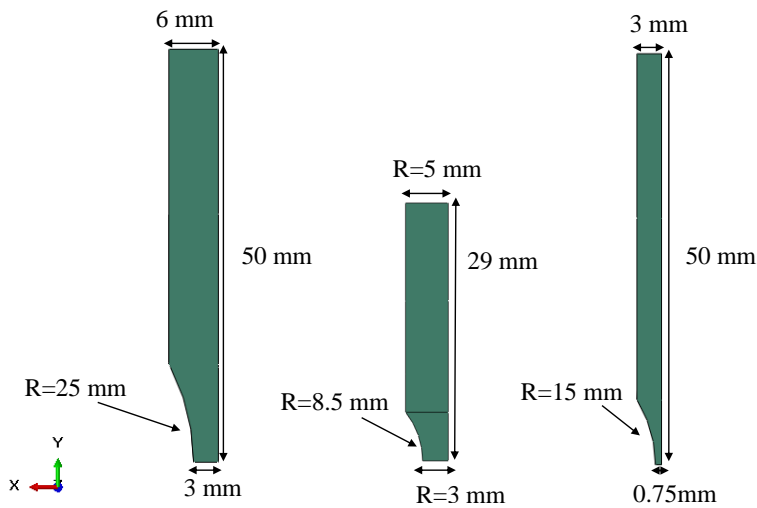


Figure 4.4: Geometry of specimens 2.a (left), 8.b (middle) and 12.c (right).

4.1.2 Plastic Deformation

Armox 500T steel is modeled as elasto-plastic with isotropic hardening defined by The Voce law and the plasticity is governed by classical J2 plasticity. The Voce law equation is expressed as in Equation 2.12. Values of C and $\dot{\epsilon}_0$ are retrieved from [91]. The Voce law parameters are tabulated in Table 4.1 and Young's modulus and Poisson's ratio of Armox 500T steel are taken as 201 GPa and 0.33.

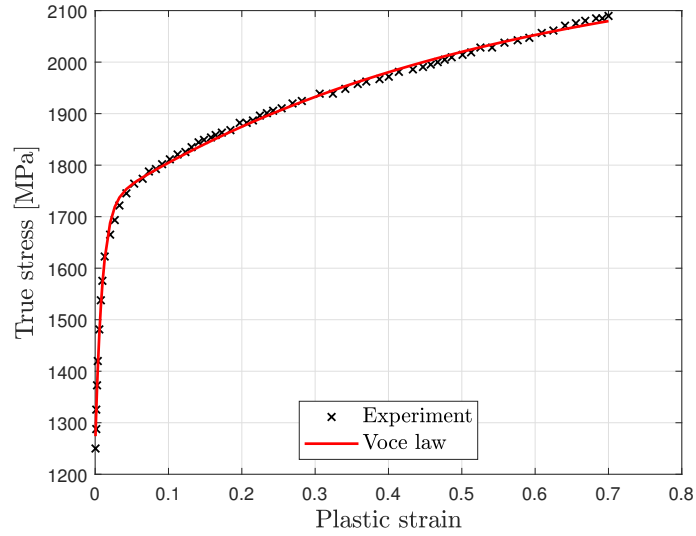


Figure 4.5: True stress-elastic strain curve of experimental data versus Voce law fit.

Table 4.1: The Voce law parameters of Armox 500T steel.

σ_{y0} [MPa]	q_1 [MPa]	q_2	q_3 [MPa]	q_4	C	$\dot{\epsilon}_0$ (1/s)
1250	470	109.1	488.6	1.903	0.0617	1

The plastic behavior of the specimen is implemented into ABAQUS through a user-defined hardening subroutine (VUHARD). True stress-elastic strain curve is shown with a comparison of Voce law equation fit and experimental data in Figure 4.5. This hardening rule is used for the simulation of tensile tests and ballistic impact process in the following sections.

4.1.3 Failure models and calibration process

Determination of material constants in the JC and MMC damage models through the hybrid experimental-numerical approach requires plastic strain, averaged of stress triaxiality and Lode angle parameter and final plastic strain at failure. However, these values are provided over the deformation history in [90]. Hence, the values are retrieved from provided figures, and averaged stress triaxiality (η_{av}) and Lode angle parameter ($\bar{\theta}_{av}$) are calculated as follows,

$$\eta_{av} = \frac{1}{\varepsilon_{eq}^p} \int_0^{\varepsilon_f} \eta d\varepsilon_{eq}^p \quad (4.1)$$

$$\bar{\theta}_{av} = \frac{1}{\varepsilon_{eq}^p} \int_0^{\varepsilon_f} \bar{\theta} d\varepsilon_{eq}^p \quad (4.2)$$

where ε_f is the fracture strain at the onset of failure and ε_{eq}^p is the von Mises equivalent plastic strain. Averaged Lode angle parameter ($\bar{\theta}_{av}$), averaged stress triaxiality (η_{av}), and fracture strain (ε_f) values for Armox 500T steel are tabulated in Table 4.2.

Material constants for JC model are calibrated using η_{av} and ε_f where $\bar{\theta}_{av}=1$ because JC is only η dependent. The fitted curve for the JC damage model (see Equation 2.13) is shown in Figure 4.6a and the calibrated JC model parameters are tabulated in Table 4.3.

MMC, in contrast to JC, is a Lode-dependent failure model as shown in Equation 2.14. Hence, $\bar{\theta}_{av}$, η_{av} , and ε_f are all used to calibrate the MMC damage model parameters. Figure 4.6b shows the 3D fracture surface of the MMC model data together with the experimental failure points. It should be noted that the 16.e specimen data has the highest deviation from the calibrated fracture surface. MMC damage model parameters are shown in Table 4.3.

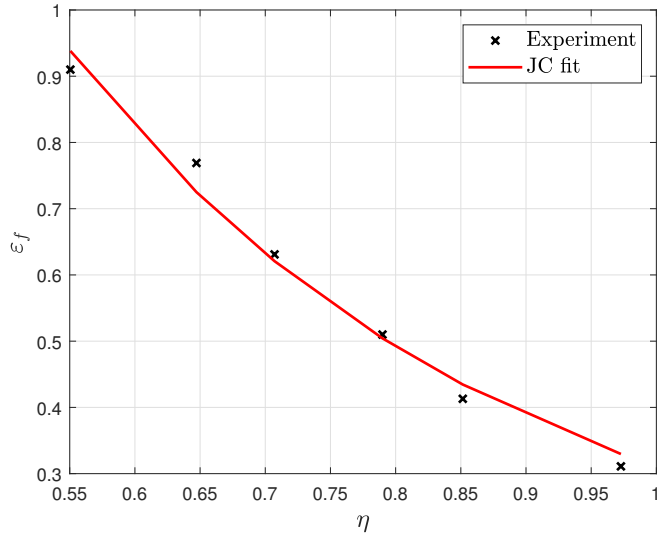
4.1.4 Failure model validation

JC and MMC damage model parameters are validated by conducting the tensile test simulations that are described previously. Force versus gauge length elongation curves are shown in Figure 4.7 for both MMC and JC damage models. It is observed

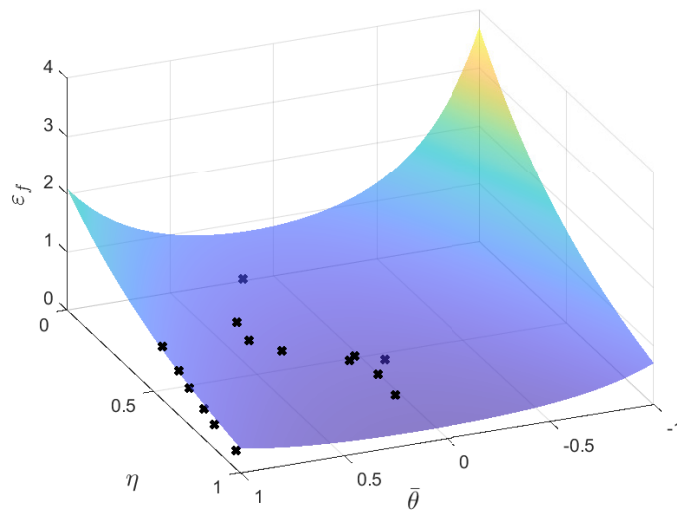
Table 4.2: Average Lode angle parameter ($\bar{\theta}_{av}$), average triaxiality (η_{av}), and fracture strain (ε_f) values for Armox 500T steel.

Specimen	$\bar{\theta}_{av}$	η_{av}	ε_f
1.a	0.5925	0.4955	0.9370
2.a	0.5455	0.5066	0.6310
3.a	0.4138	0.5424	0.4680
4.a	-0.0375	0.5980	0.2150
5.b	1.0000	0.5505	0.9100
6.b	1.0000	0.6472	0.7690
7.b	1.0000	0.7071	0.6310
8.b	1.0000	0.7899	0.5100
9.b	1.0000	0.8515	0.4130
10.b	1.0000	0.9728	0.3110
11.c	0.1249	0.6144	0.4170
12.c	0.1617	0.6309	0.3990
13.c	0.0923	0.7099	0.3470
14.c	0.0964	0.8182	0.3010
15.d	0.2807	0.1578	0.5490
16.e	-1.0000	-0.6202	1.4990

that the JC and MMC model results for specimen 5.b are nearly identical and agree well with the experiments. Specimen 8.b shows that the MMC model is in better agreement with the experimental data compared to the JC model. Furthermore, for specimens 2.a and 12.c prediction of these models differs a lot and the MMC model is in better accordance with the experiments overall.



(a) η vs ε_f for JC damage parameter calibration.



(b) $\bar{\theta}$ vs. η vs. ε_f curve for MMC damage model parameter calibration.

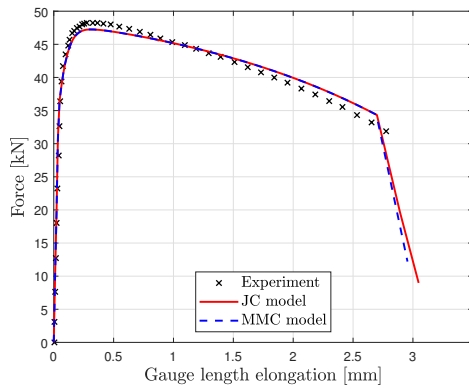
Figure 4.6: JC and MMC damage model curve fits.

4.2 Ballistic Impact Simulations

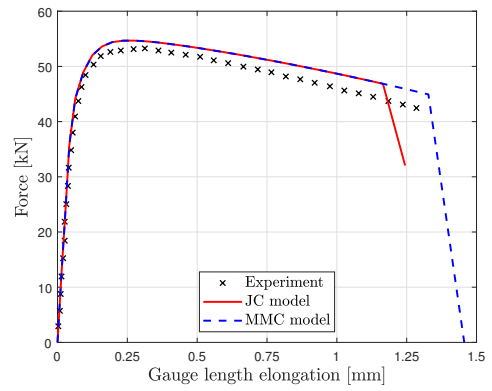
This section presents the FE modeling process and the different ballistic impact configurations explored in this work. In this work, 7.62 API and 12.7 API projectiles are used with various $\bar{\theta}$ target thicknesses. Additionally, blunt and hemispherical projectile

Table 4.3: JC and MMC damage model parameters for Armox 500T steel.

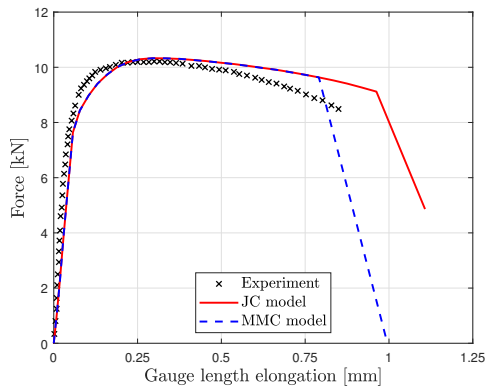
D_1	D_2	D_3				
0.09	4.406	2.993				
K (MPa)	n	\hat{C}_1	\hat{C}_2 (MPa)	\hat{C}_3	\hat{C}_4	
1903	0.04235	0.03595	994.3	0.9105	1	



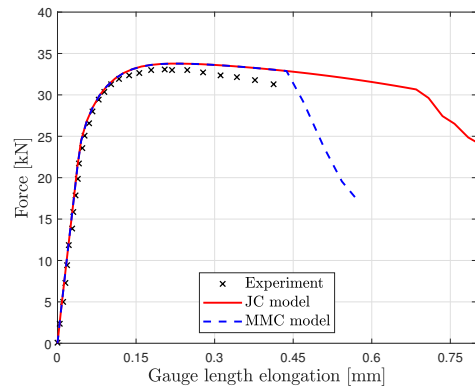
(a) 5.b



(b) 8.b



(c) 2.a



(d) 12.c

Figure 4.7: Comparison of JC and MMC damage models with the experimental data [90]. Force vs gauge length elongation for specimens (a) 5.b, (b) 8.b, (c) 2.a and (d) 12.c.

geometries are studied. The thickness value of the target is varied between 2 mm and 10 mm. The impact angle, α , is investigated for 0° , 15° , 30° , 45° , and 60° . Projectile geometries, FE model set-up and illustration of oblique impact are illustrated in Figure 4.8. The geometry 7.62 and 12.7 API projectiles are retrieved from [91] while the blunt and hemispherical ones are modeled to match the height and diameter of the 7.62 API projectile. Shank diameter, shank length, total length, and ogival nose length are 6.06, 20.75, 28.4, and 7.65 mm for 7.62 API, and 10.9, 24.4, 52.6, and 19.1 mm for 12.7 API, respectively. The target is modeled as a deformable body, whereas the projectile is treated as rigid. The mass of the projectiles is 5.5 g for 7.62 API, blunt and hemispherical projectiles, and 30.06 g for 7.62 API and 12.7 API projectiles. A reference point is attached to the nose tip of the projectile, and mass and velocity are assigned to this point. The displacement of the projectile at the x and y directions is restricted in perpendicular impact scenario and only x displacement is restricted in oblique impact simulations. Kinematic contact algorithm with "hard" contact is adapted between the target and projectile.

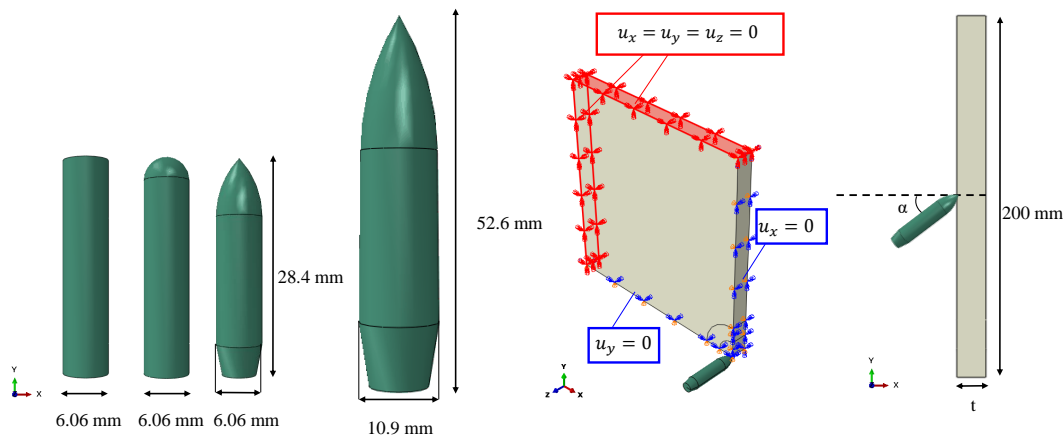


Figure 4.8: Projectile geometries (left), ballistic impact FE model boundary conditions (middle), impact angle (α) illustration (right).

A quarter of the target is modeled to reduce computational costs. A study is carried out to demonstrate that quarter and full model simulations provide the same outcomes. The quarter and full-scale body of the target is shown in Figure 4.9. For oblique impact simulations, however, half portion of the target is modeled to be able to predict failure mechanism correctly. At the impact zone, the target is partitioned into three zones to increase mesh density. The inner surface of the target is subjected to sym-

metry boundary conditions while the outer surface of the target is fixed as shown in Figure 4.8.

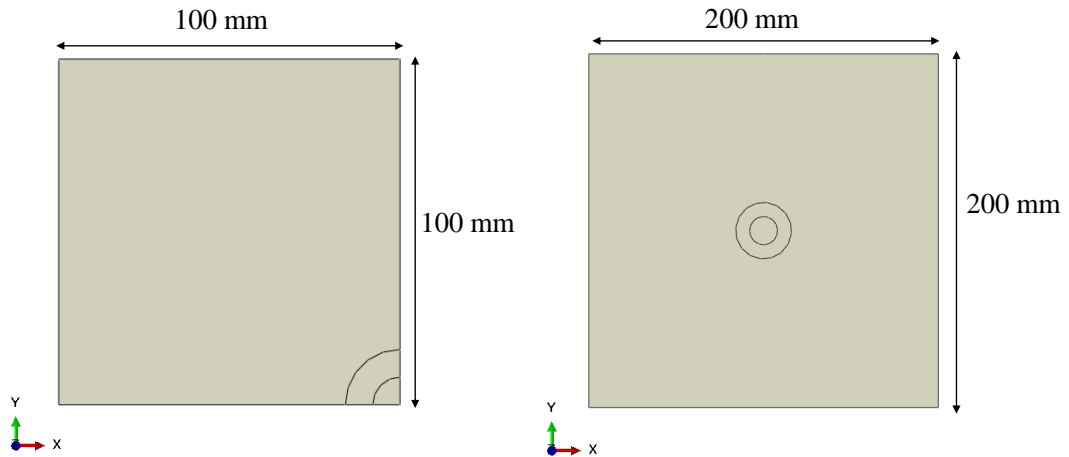
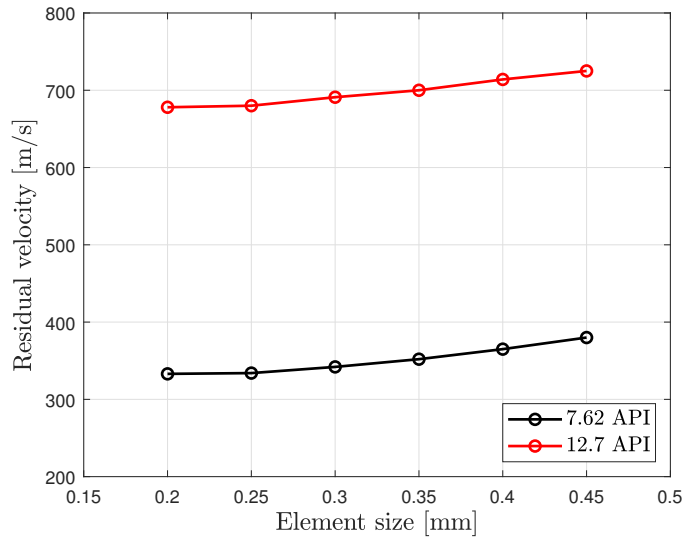


Figure 4.9: Quarter target (left), full scale target (right).

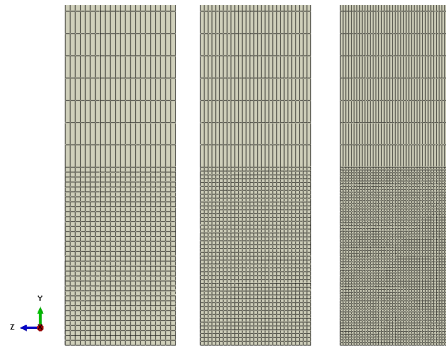
Mesh and time increment convergence studies are carried out using the JC failure model. The variation in residual velocity with respect to the element size is shown in Figure 4.10a. The minimum element size in the impact zone is investigated using an 8 mm thick target. The initial velocity of the projectile is 823.62 m/s for 7.62 API and 841.89 m/s for 12.7 API. Element size is varied from 0.45 to 0.20 mm. Convergence is achieved at 0.25 mm element size for both 7.62 API and 12.7 API projectiles. The mesh density of the target is decreased towards the edges. Figure 4.10b illustrates a mesh convergence analysis for mesh sizes of 0.45 mm, 0.35 mm, and 0.25 mm.

Furthermore, a step-size increment study is conducted for JC and MMC models at 823.62 m/s initial velocity with 7.62 API projectile. Increment size is varied between 10^{-10} and 5×10^{-9} as shown in Figure 4.11. 5×10^{-10} is found to be yielding almost converged residual velocities without increasing the computation times too much. These values are utilized in all of the following studies.

As previously discussed in the preceding chapter, it is crucial to confirm the precision of simulation outcomes by validating the preservation of energy within the simulations. This is demonstrated in Figure 4.12, which depicts the conservation of kinetic energy, internal energy, hourglass energy, and total energy at 823.62 m/s initial velocity with a 7.62 API projectile. During the impact process, the hourglass energy



(a) Residual velocity (m/s) vs. element size (mm) curve.



(b) FE models with 0.45 mm, 0.35 mm and 0.25 mm element sizes.

Figure 4.10: Mesh convergence study.

appears to be less than 3% of the overall energy, indicating that hourglassing is not an issue. The energy dissipated by element deletion is determined to be minimal (less than 1% of total energy).

4.3 Results and discussion

In this section, the discussion focuses on the validation of results with experimental data from the literature [91], followed by a comparison of JC and MMC models using

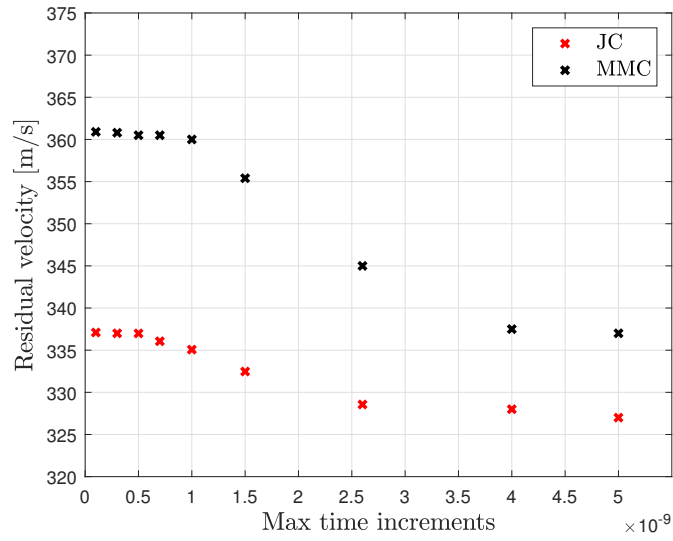


Figure 4.11: Residual velocity (m/s) vs. maximum time increments curve.

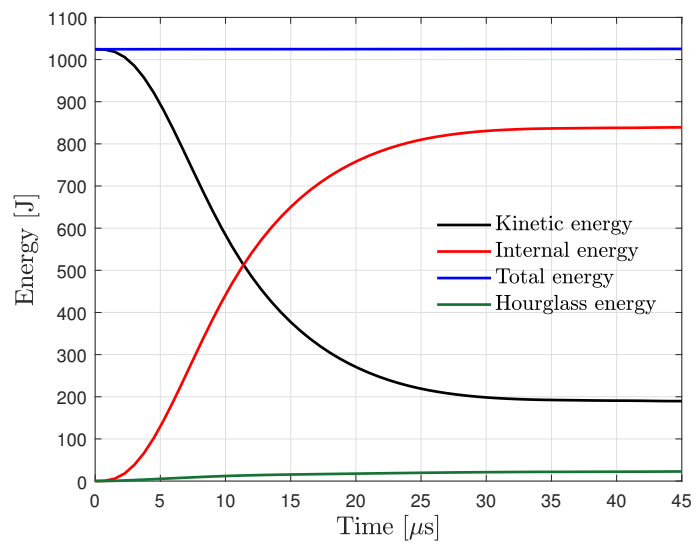


Figure 4.12: Energy time history of the target and projectile.

different configurations of the impact process. These configurations include different target thicknesses, impact velocity, and oblique impact cases with three projectile nose shapes.

4.3.1 Comparisons with experiments

The 7.62 API projectile is shot against an 8 mm thick ArmoX 500T target to match the experimental setup. The projectile's initial velocities are reported as 823.62 m/s and 828.02 m/s. In Table 4.4, experimental and numerical residual velocities are compared. At an initial velocity of 823.62 m/s, the error for the JC model is 0.77% and 7.71% for the MMC model. At 828.02 m/s initial velocity, the JC model predicts residual velocity with 0.80% error while the MMC model predicts with 7.38% error. Both models are able to predict accurate residual velocities with less than 8% error. The JC model is found to be more accurate for this configuration.

It should be noted that ballistic impact is a highly strain rate-dependent process. If a rate-independent hardening relation is used, experiments and the FE analysis results do not agree well. The residual velocity of 571 m/s is obtained with the rate-independent form of the Voce rule while the experimental value is 334.28 m/s. Hence the Voce hardening law is coupled with $(1 + C \ln \dot{\epsilon}_{eq}^*)$ to improve the capability of the FE framework.

Table 4.4: Experimental and numerical results for 7.62 API projectile with 8 mm thick target.

Initial velocity (m/s)	Residual velocity (m/s)				
	Experiment	JC	MMC	JC error (%)	MMC error (%)
823.62	334.28	336.87	360.07	0.77	7.71
828.02	343.74	346.52	369.13	0.80	7.38

A comparison of the failure mechanism of ArmoX 500T steel against a 7.62 API projectile with an 8 mm thick target is shown in Figure 4.13. The front view is where the projectile enters the target plate, and the back view is where it exits. With both JC and MMC models, ductile hole enlargement is observed. The hole diameter with the JC model is 8.15 mm and 8.20 mm with the MMC model while it is measured as 8.10 mm in experiments. Both models correctly predicted the diameter of the hole. In terms of failed surfaces, FE simulations resulted in bulges in the back view but the MMC model predicted a larger bulge in agreement with the experimental

observations.

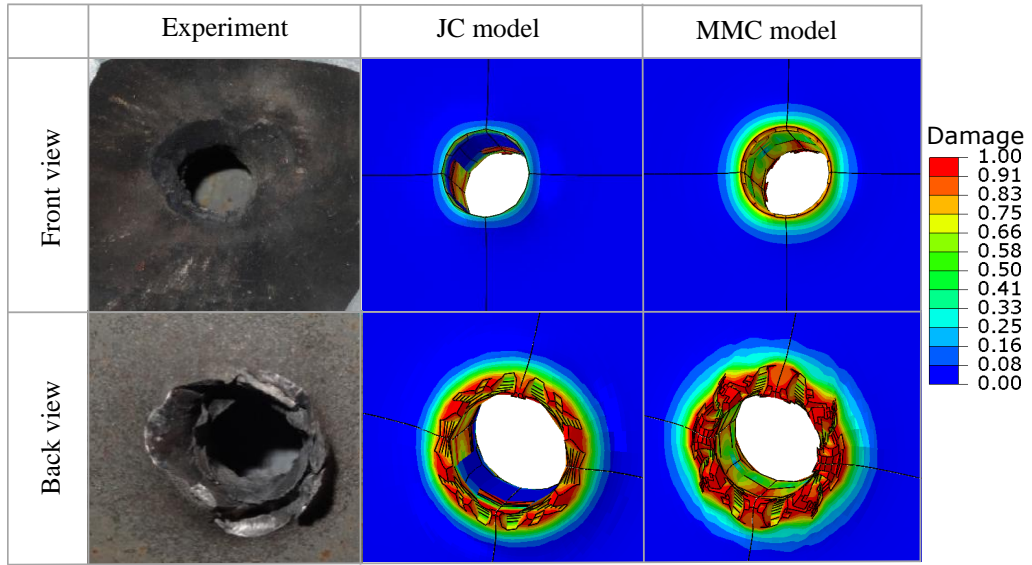


Figure 4.13: Failure mechanism of Armox 500T steel against 7.62 API projectile with 8 mm thick target. Experimental data from [91].

Table 4.5: Experimental and numerical results for 12.7 API projectile with 10 mm thick target.

	Initial velocity (m/s)		Residual velocity (m/s)			
	Experiment	JC	MMC	JC error (%)	MMC error (%)	
831.67	663.82	664.92	683.90	0.16	3.02	
841.89	686.37	681.99	697.90	0.63	1.67	

Experimental and numerical results of residual velocities for 12.7 API projectile with a 10 mm thick target are shown in Table 4.5. JC and MMC damage models predict the residual velocities with high accuracy with a maximum error of 3%. Similar to the previous case, the JC model is found to be better at predicting the experimental residual velocity compared to the MMC model. Figure 4.14 illustrates a comparison of the failure mechanism of Armox 500T steel against a 12.7 API projectile with a 10 mm thick target. A similar trend is observed in the 12.7 API projectile results and the 7.62 API results. Ductile hole enlargement is the main failure mechanism

observed as well as a bulge is formed in the back surface. The size of the bulge is larger in the MMC case. In the experiments, the hole diameter is measured as 13.12 mm, whereas it is 13.16 mm with the JC model and 13.19 mm with the MMC model. Again both models are able to predict accurate hole diameters. Overall, the MMC model outperforms the JC model in terms of failure mode predictions while both models are accurate in residual velocity outcomes.

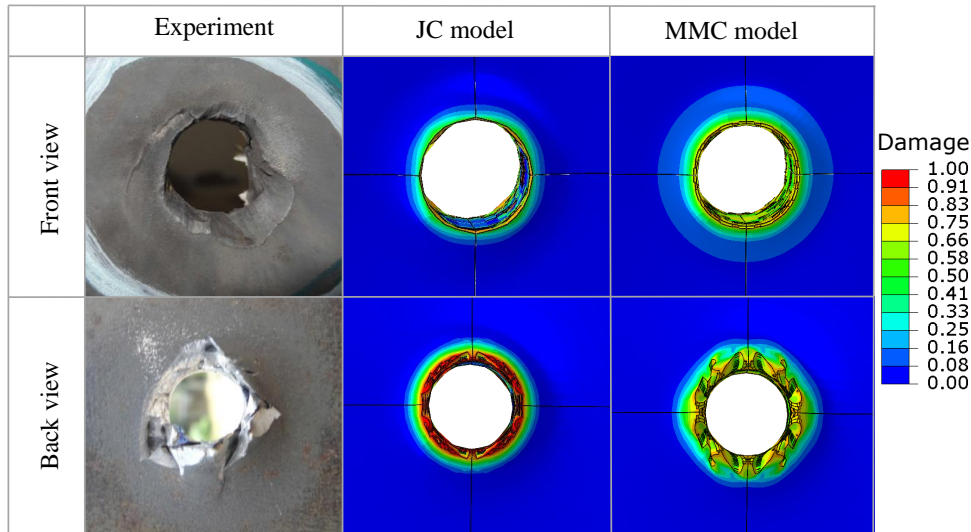


Figure 4.14: Failure mechanism of ArmoX 500T steel against 12.7 API projectile with 10 mm thick target. Experimental data from [91].

4.3.2 Comparison of the JC and MMC models under various configurations

Although it has been shown in the previous section that both failure models perform well compared to experiments, the comparison is limited to a few cases. As discussed, the accuracy of the failure model depends on the dominant stress state during fracture which may change with impact process parameters. Thus, the applicability of these models is explored under various impact configurations in this section. The relative percent difference between the JC and MMC models is formulated as

$$\%D = \frac{|v_R^{MMC} - v_R^{JC}|}{v_R^{MMC}} \quad (4.3)$$

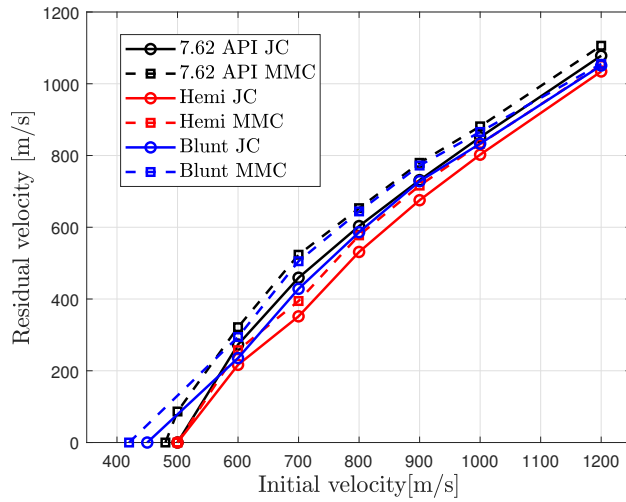
where v_R^{MMC} and v_R^{JC} are the residual velocities predicted by the MMC and the JC models, respectively.

Firstly, the influence of changing thickness on residual velocity is studied with different projectiles at initial velocities ranging from 400 to 1200 m/s. Initial versus residual velocity plot is shown in Figure 4.15 for 4 mm and 8 mm thick targets. The minimum velocity required to penetrate the target is lowest for the blunt projectile and highest for the hemispherical projectile. All three nose shapes follow a similar trend with increasing the initial velocity at both target thicknesses. The MMC model consistently produces higher residual velocities compared to the JC model.

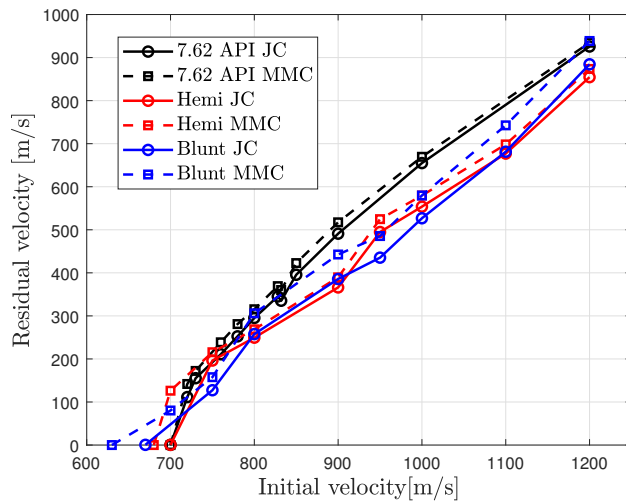
The percentage difference between residual velocities provided by JC and MMC models is plotted for 4 mm and 8 mm thick targets in Figure 4.16. It is observed that the difference between models decreases significantly as the initial velocity increases. The difference is less than 10% at and above initial velocities of 800 m/s except for the blunt projectile impacted on an 8 mm target. At lower impact velocities, the least difference is observed with the hemispherical projectile.

Figure 4.17a shows a comparison of JC and MMC models using projectiles with different nose shapes at varying thicknesses. Targets with thicknesses of 2 mm, 4 mm, 6 mm, 8 mm, and 10 mm are impacted by 7.62 API, hemispherical, and blunt projectiles at 900 m/s initial velocity. It is demonstrated that residual velocity decreases for all projectiles for both the JC and MMC models as the target thickness increases, with the JC model consistently providing lower residual velocities than the MMC model. Moreover, when the target thickness is increased, the residual velocity for 7.62 API projectiles decreases almost linearly, whereas there is a significant drop in residual velocity for hemispherical and blunt projectiles after an 8 mm target thickness. Blunt and hemispherical projectiles appear to be more sensitive to target thickness than the 7.62 API projectile. The difference between JC and MMC model predictions is plotted in Figure 4.17b. No apparent trend is captured except for the blunt projectile results. The difference increases as the target thickness increases with the blunt one. For the other two nose shapes, the difference between models is less than 8%.

Effect of obliquity is investigated using 7.62 API, hemispherical, and blunt projectiles at impact angles of 0°, 15°, 30°, 45° and 60° at 900 m/s initial velocity on 4 mm thick



(a) Target thickness = 4 mm



(b) Target thickness = 8 mm

Figure 4.15: Residual velocity (m/s) vs. initial velocity (m/s) curves for (a) 4 mm and (b) 8 mm thick targets

target, and the results are presented in Figure 4.18a. Residual velocity decreases as obliquity increases, with MMC consistently providing higher residual velocity than the JC model; however, the dependency on impact angle for the three nose shapes is vastly different. The blunt projectile is the most sensitive to obliquity change, whereas the 7.62 API projectile is the least sensitive. A significant change in the behavior of the hemispherical projectile is observed after 45° obliquity. The residual velocity

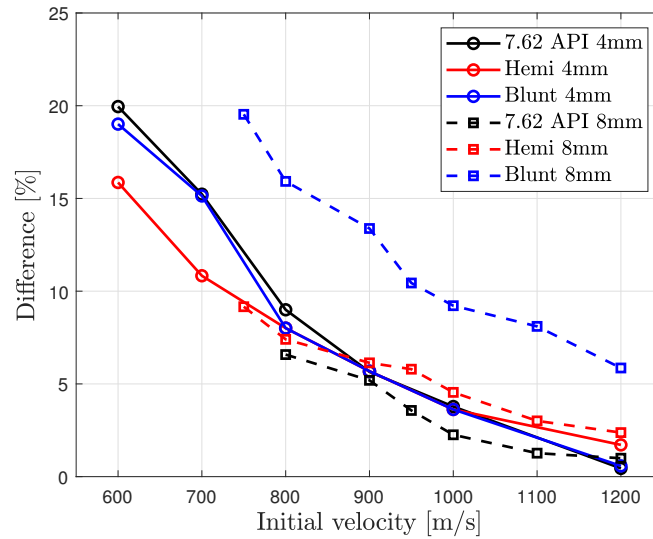
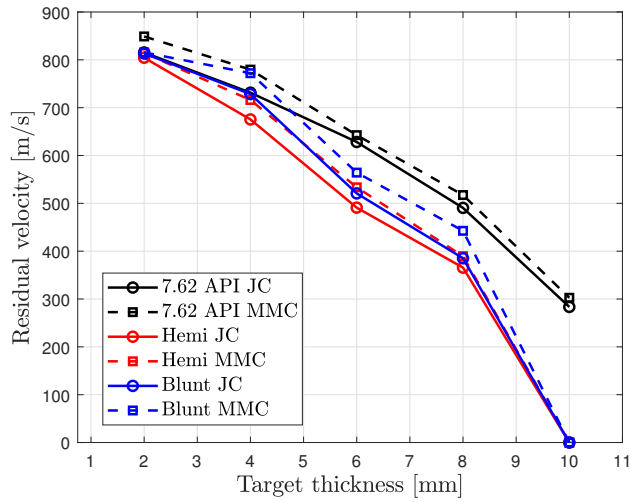


Figure 4.16: Difference of JC and MMC models in (%) vs. initial velocity (m/s) at 0° impact angle for 4 mm and 8 mm thick targets.

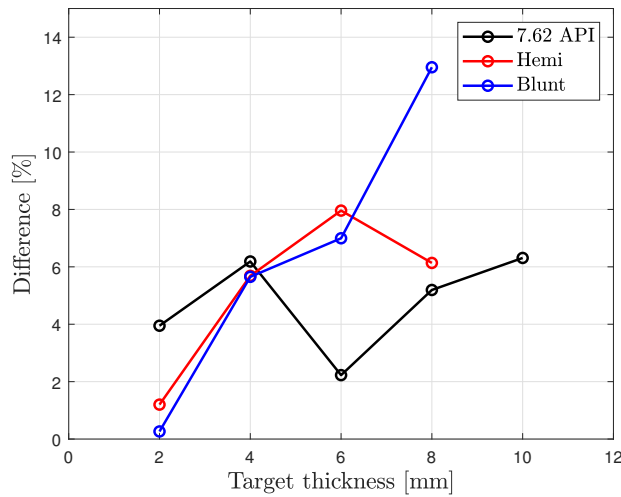
almost linearly decreases with increased impact angle for the blunt projectile. Figure 4.18b illustrates the difference between the two failure models for the three projectile shapes with varying impact angles. The biggest difference between damage models is observed at 0° for 7.62 API. The difference decreases from 0° to 15° impact angle for hemispherical and 7.62 API projectiles and then the difference increases with increasing obliquity. However, this trend is not observed for the blunt projectile. Nevertheless, ballistic impact at increased obliquity may require a Lode parameter-dependent failure model for accurate predictions of residual velocity.

4.3.3 Comparison of failure modes

Depending on the configuration of the ballistic impact, different failure modes are observed. The projectile nose shape is a critical feature that dictates the failure mechanism. Figure 4.19 shows failure mechanisms observed in FE analysis of 7.62 API projectile at 900 m/s initial velocity with 4 mm thickness for 0° , 15° , 30° , 45° , and 60° obliquity. Ductile hole enlargement is observed in all cases. At low obliquity, the difference between JC and MMC models is not significant. However, at 45° and 60° petaling is observed for the MMC model whereas only ductile hole enlargement is



(a) Residual velocity (m/s) vs. target thickness (mm) curve.

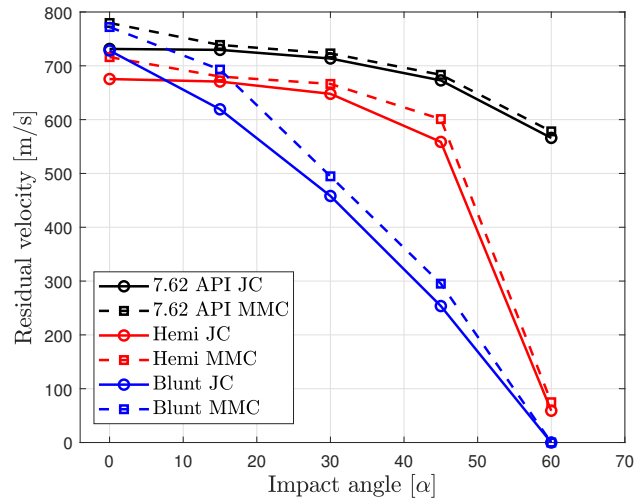


(b) Difference(%) vs. target thickness (mm) curve.

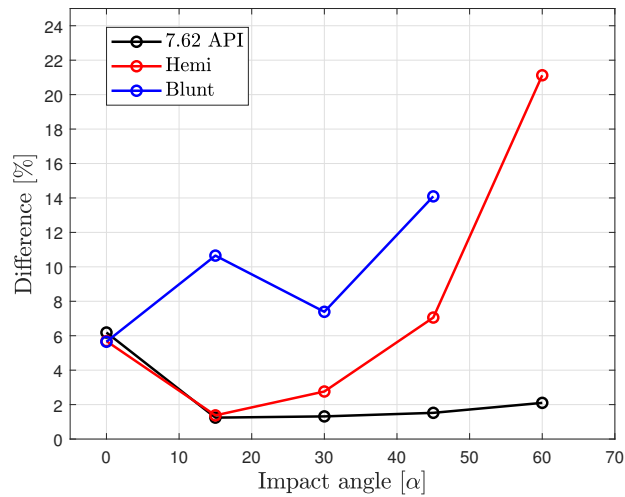
Figure 4.17: (a) Residual velocity (m/s) vs. target thickness (mm) curves and (b) percent difference between JC and MMC damage models for various target thickness at 900 m/s initial velocity.

observed for the JC model. Experiments in [95] show that at higher obliquity petaling failure mechanism is observed with ogival projectiles on metal plates; thus, the MMC model matches the experimentally observed failure mechanism.

Failure mechanisms of blunt projectile is studied at 900 m/s initial velocity with 4



(a) Residual velocity (m/s) vs. imp. angle



(b) Difference(%) vs. imp. angle

Figure 4.18: (a) Residual velocity (m/s) vs. impact angle (α) curves and (b) percent difference between JC and MMC damage models for various impact angles at 900 m/s initial velocity.

mm thickness for 0° , 15° , 30° , 45° , and 60° obliquity and the results are illustrated in Figure 4.20. It should be noted that the presented results are taken at the same time step. At lower obliquity, shear plugging and fragmentation are the main failure modes, whereas the mode changes to tearing at higher obliquity. A similar pattern is experimentally demonstrated in [43] using blunt projectiles on metal targets for

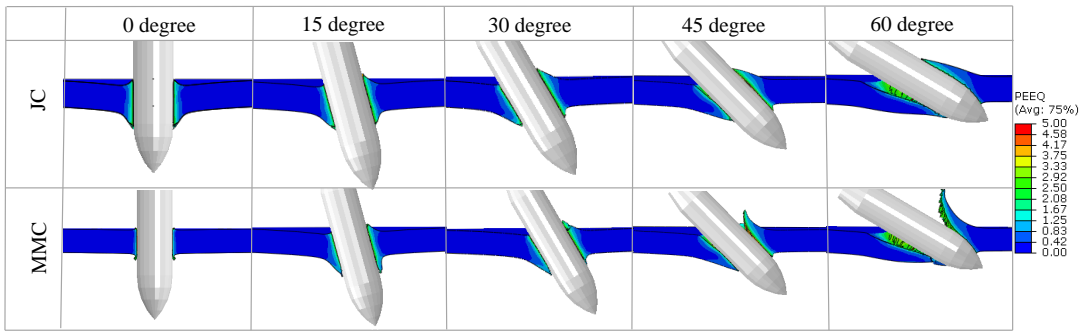


Figure 4.19: Failure mechanisms of 7.62 API projectile at 900 m/s initial velocity for 4 mm target thickness and at 0°, 15°, 30°, 45°, and 60° obliquity with JC and MMC models.

oblique impact. For the MMC case, the plug size is smaller at 0°. At 45°, the separation of the plug is slightly different for JC and MMC cases. Overall, the observed failure mechanisms are not significantly different for the two failure models. 60° projectile failed to penetrate the target for both cases.

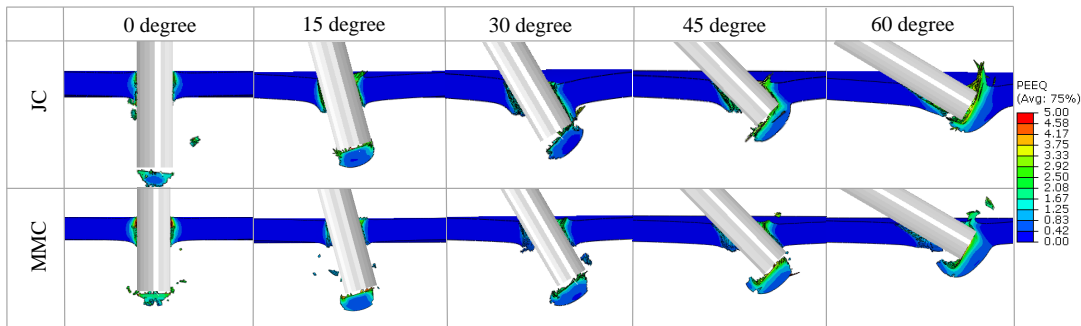


Figure 4.20: Failure mechanisms of blunt projectile at 900 m/s initial velocity for 4 mm target thickness and at 0°, 15°, 30°, 45°, and 60° obliquity with JC and MMC models.

For hemispherical projectiles, failure mechanisms at 900 m/s initial velocity with 4 mm thickness for 0°, 15°, 30°, 45°, and 60° obliquity with the JC and the MMC models is shown in Figure 4.21. Fragmentation and ductile hole enlargement are simultaneously observed for all configurations. The number of fragments in the MMC

simulations is greater than in the JC ones. The results in Figure 4.21 are produced at the same time step. Note that all of the projectiles have a non-zero residual velocity in these simulations.

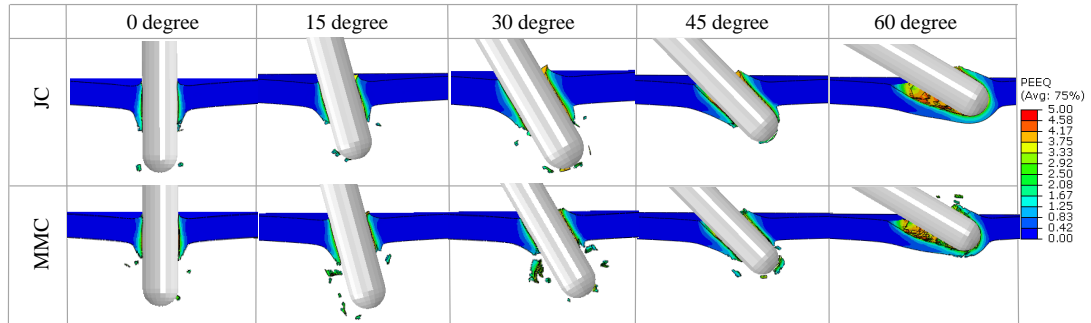


Figure 4.21: Failure mechanisms of hemispherical projectile at 900 m/s initial velocity for 4 mm target thickness and at 0°, 15°, 30°, 45°, and 60° obliquity with JC and MMC models.

In the previous chapter, the SPH method is utilized to study the failure mechanisms of metal targets. The SPH method's particle-based nature prevented it from accurately predicting failure mechanisms. Fast residual velocity predictions can be obtained using the SPH method, but the FE method should be used to identify failure mechanisms. Simulations with the SPH method are therefore not conducted in this work.

CHAPTER 5

A NUMERICAL STUDY ON THE BALLISTIC PERFORMANCE OF PROJECTILES FORMED BY SHAPED CHARGE

In this chapter, a numerical analysis of the shaped charge impact process is conducted to investigate the jet formation process and its penetration performance on metal targets. Numerical results are compared with experimental data from published literature for liners made up of copper and iron [55]. Conical and bowl-shaped liner geometries are simulated with various configurations to observe their effects on projectile shape and penetration capability using the FE method. #45 and Armox 500T steels are used as the target materials. In addition to the FE method, SPH is utilized as well to evaluate its capacity in predicting the failure behavior of the metal targets.

5.1 Numerical analysis

In this section, methods for numerical modeling of jet formation and penetration processes are addressed separately. FE and SPH analysis are conducted through ABAQUS/Explicit solver for both processes. Constitutive models and relevant parameters are given for the materials used in the computational analysis.

5.1.1 Jet formation process

Shaped charge impact consists of an explosive charge, a liner, and a target. In this study shaped charge impact is modeled in two stages. Firstly, the detonation and forming of the jet are modeled using FE analysis in 2D. JWL equation of state and JC plasticity model are utilized. Copper and iron liners, as well as the influence of

the cone angle, α , and m distance, are studied. The conical liner is formed using the bowl-shaped liner geometry given in [55]. Geometries and dimensions of the liners are shown in Figure 5.1. The mass of the copper and iron liner are given in the aforementioned study as 69.4 g and 60.6 g, respectively. Interaction between the explosive charge and the liner is defined using a kinematic contact algorithm. Symmetry boundary conditions are applied at the center of the model. Both parts are meshed with 4-node axisymmetric elements (CAX4R). Projectile velocities are measured at 160 μ s, corresponding to the onset of the jet making contact with the target.

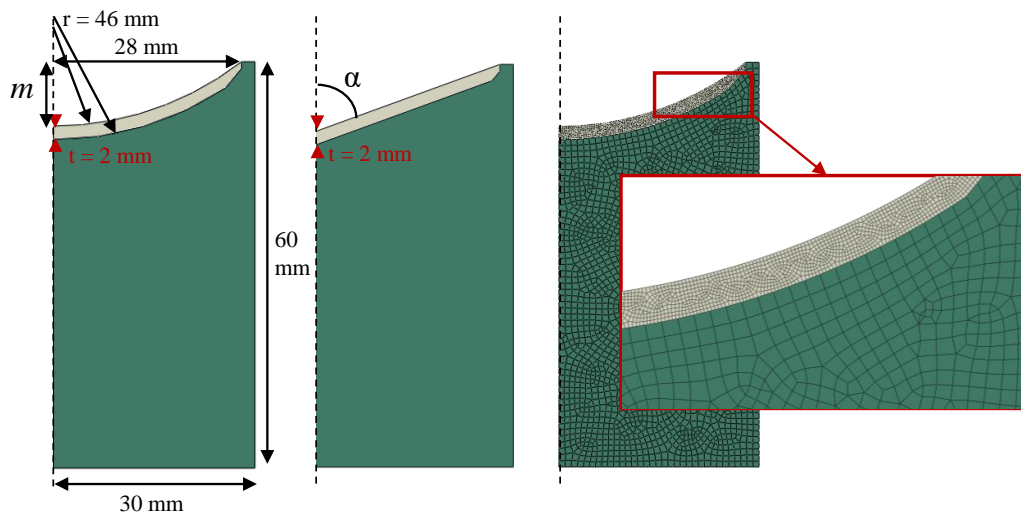


Figure 5.1: Geometry of explosive charge and bowl-shaped (left) and conical (middle) liners. Axisymmetric FE model of the bowl-shaped liner (right).

A convergence study is conducted for mesh size. Mesh convergence study for copper and iron liners is presented in Tables 5.1 and 5.2. As the mesh becomes finer the jet tip velocity increases. Convergence is achieved at 0.20 mm element size for both of the liners. When the convergence is achieved, jet tip velocity, x- momentum and kinetic energy values do not change significantly. 0.2 mm element size is used for the liner in the following simulations while 2 mm is used for the explosive charge (see Figure 5.1).

A maximum time increment convergence study is conducted for both of the liners.

Table 5.1: Properties of copper jet at $160\mu\text{s}$ with varying element sizes.

Element size (mm)	Jet tip velocity (m/s)	X-momentum (kg·m/s)	Kinetic energy (J)
0.15	1484	102.69	7.5669×10^4
0.20	1482	102.55	7.5663×10^4
0.30	1465	101.37	7.5605×10^4
0.40	1440	99.64	7.4690×10^4
0.50	1402	97.01	7.4685×10^4

Table 5.2: Properties of iron jet at $160\mu\text{s}$ with varying element sizes.

Element size (mm)	Jet tip velocity (m/s)	X-momentum (kg·m/s)	Kinetic energy (J)
0.15	1593	95.58	7.5909×10^4
0.20	1592	95.52	7.5908×10^4
0.30	1577	94.62	7.5803×10^4
0.40	1550	93.00	7.5795×10^4
0.50	1509	90.54	7.5601×10^4

Step size is varied from 1×10^{-9} to 8×10^{-8} as shown in Figure 5.2. A step size increment of 7.44×10^{-9} is used for both of the liners.

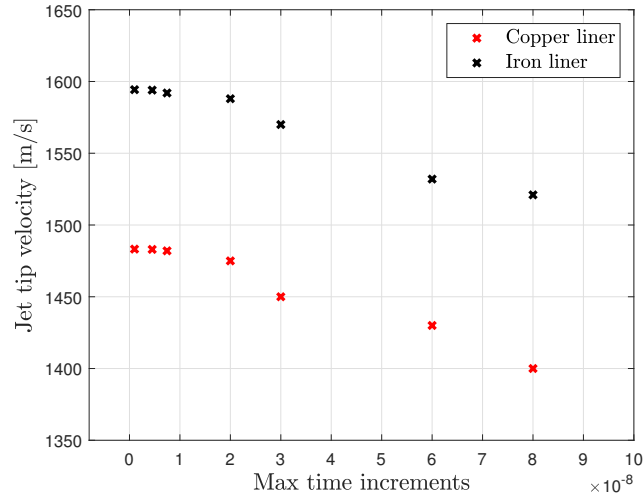


Figure 5.2: Jet tip velocity (m/s) vs. maximum time increments curve.

Copper and iron are utilized as the metal liner material in the current work. Material behavior is governed by the von-Mises plasticity model with the JC isotropic

hardening law. JC is employed here since materials undergo deformation at high strain rates in shaped charge impact. JC model parameters are adopted from [23, 55]. The yield stress in this model is given in Equation 2.11. The JC model is used in a temperature-independent form. It is a common misconception that shaped charges efficiency depends on heating or melting. The ballistic effectiveness of an EFP is entirely determined by its kinetic energy rather than thermal factors [52, 96, 97]. Material parameters are presented in Table 5.3.

Table 5.3: Material parameters of copper and iron liners.

Elastic constants				
	E (GPa)	ν	ρ (g/cm ³)	
Copper	46.50	0.34	8.97	
Iron	80	0.39	7.89	
JC model parameters				
	A (MPa)	B (MPa)	n	C
Copper	90	292	0.31	0.025
Iron	175	380	0.32	0.060

In order to define the equation of state of the liners, the shock Hugoniot-based Mie-Grüneisen EOS is utilized and it is thoroughly discussed in Chapter 2. EOS parameters for copper and iron are shown in Table 5.4.

Table 5.4: EOS parameters for copper and iron liners.

Material	s	Γ_0	c_0 (km/s)
Copper	1.49	2.02	3.94
Iron	1.92	2.02	3.57

8701 explosive is used as the charge material and its behavior is defined with The Jones-Wilkens-Lee (JWL) EOS model. Material parameters of the explosive are shown in Table 5.5. The formulation of JWL is shown in Equation 2.25. EOS parameters are obtained from [55].

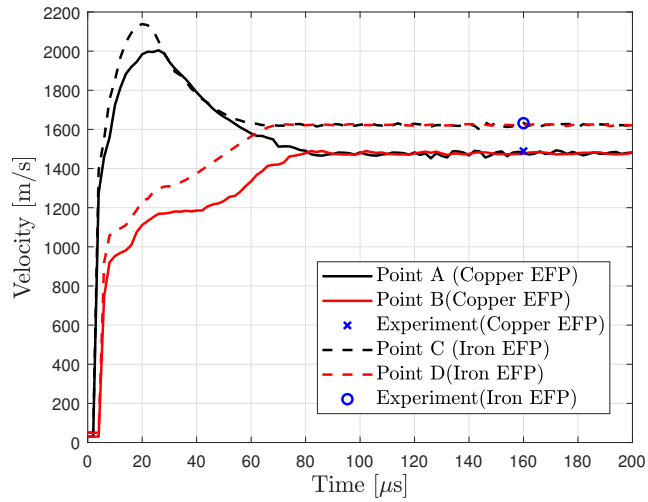
Table 5.5: Material parameters of explosive.

Material	\hat{A}	\hat{B}	R_1	R_2	ω	$\rho(g/cm^3)$	D (km/s)
8701 explosive	524.23	7.678	4.20	1.1	0.34	1.71	8.315

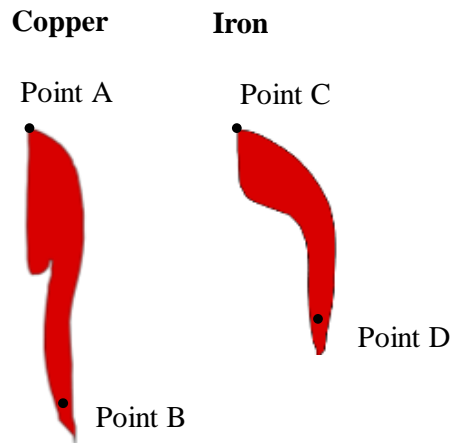
5.1.2 Penetration process and damage modeling

In the second part of the shaped charge impact, the formed shape of the EFP is extracted as a 3D geometry and the impact is simulated in a 3D setting. The projectile is treated as a rigid body, as performed in [86, 87], to simplify the process and overcome the difficulties of modeling shaped charge impact. In this study, velocity of the tip and the tail of the EFP converges before penetration as shown in Figure 5.3; thus, the velocity of the projectile is the same throughout the body. As the jet moves farther from the shaped charge, it has more time to stabilize and achieve a relatively constant shape and velocity. The specific distance at which the jet stabilizes varies based on factors such as the size and shape of the shaped charge and the explosive type. Once the jet reaches a stable state, its shape and velocity remain mostly constant as it approaches the target.

In addition to penetration of formed EFPs, maximum penetration depth and impact angle (β) are investigated. 500 mm thick #45 steel and 250 mm thick Armox 500T targets are used to study maximum penetration depth. Impact angle (β) and thickness of the target (t) are illustrated in Figure 5.4. Investigated impact angles are 0° , 15° , 30° and 45° . Using EFP with $\alpha = 65^\circ$, the effect of varying thickness on residual velocity is also examined. The penetration process is modeled in FE software ABAQUS with 3D elements with reduced integration (C3D8R). One-fourth of the geometry is modeled for all FE analysis except for oblique impact simulations where a half model is used to save computational time. Thickness of the target is taken as 20 mm to match the impact experiments. The outer surface (shown in red in Figure 5.4) of the target is fixed in all three directions while for the inner surfaces of the target (shown in blue in Figure 5.4), symmetry boundary conditions are applied. Displacement of the EFP in x and y directions are restricted. Contact between the EFP and the target is defined using a kinematic contact algorithm. Target is meshed finer at the penetration



(a) Velocity vs time



(b) Representation of the points

Figure 5.3: Velocity variation plot for various points on formed jets.

zone and coarser at the outer parts as shown in Figure 5.5. In the case of SPH, a full-scale model is employed due to failure modes being inconsistent between the quarter model and full model, which is not a problem in FE analysis. Moreover, partitioning the part in the SPH method causes separation at the partition boundaries. Thus, the SPH model is not partitioned and the element size is gradually reduced towards the impact zone (see Figure 5.5). By varying the minimum element size in the impact zone for both FE and SPH analysis, a mesh convergence study is carried out and

presented for $\alpha = 65^\circ$ and $m = 7.5$ mm in Figure 5.6. The minimum element size varied between 0.15 mm and 0.35 mm. It can be seen that the residual EFP velocity for FE simulations converged at 0.25 mm, whereas for SPH simulations, it converged at 0.20 mm. Hence for FE and SPH methods, the minimum converged element sizes are found to be different and they are selected as 0.25 mm and 0.20 mm, respectively.

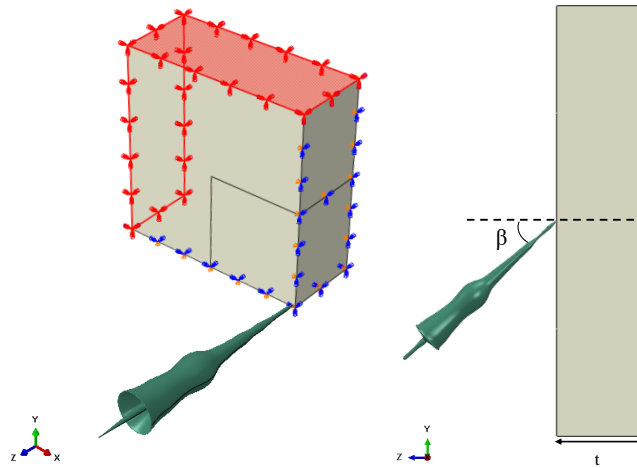


Figure 5.4: Boundary conditions of the target (left) and illustration of thickness (t) and impact angle (β) (right).

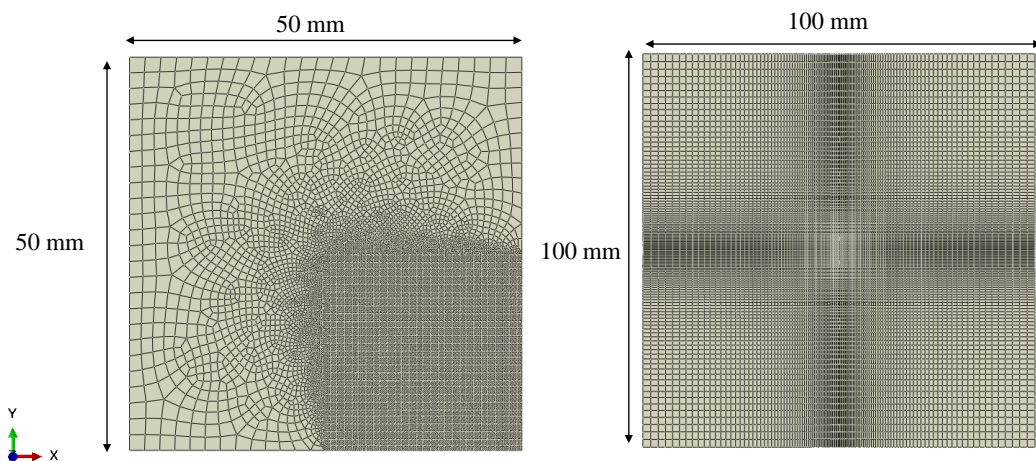


Figure 5.5: FE model with max mesh size: 2 mm, min mesh size: 0.25 mm (left) and SPH model with max mesh size: 2 mm, min mesh size: 0.20 mm (right) models of the target.

Two different target materials are investigated in this study which are #45 steel and

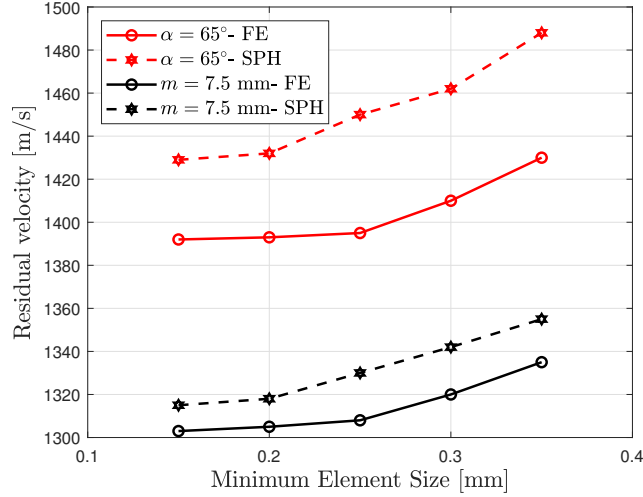


Figure 5.6: Mesh convergence study for $\alpha = 65^\circ$ and $m = 7.5$ mm with FE and SPH methods.

Armox 500T. Similar to jet formation process the the plastic behavior of the materials is assumed to follow classical J2 plasticity with isotropic hardening law defined by the JC plasticity model in Equation 2.11. Model parameters of #45 steel and Armox 500T are tabulated in Table 5.6, adopted from [55, 91].

Table 5.6: JC plasticity parameters of #45 steel and Armox 500T

Elastic constants				
	E (GPa)	ν	ρ (g/cm ³)	
#45 Steel	77	0.3	7.83	
Armox 500T	201	0.33	7.85	
JC model parameters				
	A (MPa)	B (MPa)	n	C
#45 Steel	792	510	0.2	0.014
Armox 500T	1372.488	835.022	0.2467	0.0617

Different than most of the studies in the literature addressing shaped charge impact

process, in the penetration analysis the ductile damage modeling approach is employed here. In this context, the ductile failure of the target is investigated using strain rate, temperature, and stress triaxiality-dependent JC damage criteria. The failure strain is defined by Equation 2.13. Values of the damage constants can be seen from Table 5.7. JC damage model parameters for #45 and Armox 500T steels are retrieved from [92, 91].

Table 5.7: JC damage model parameters of #45 and Armox 500T steels.

Material	D_1	D_2	D_3	D_4
#45 Steel	0.1	0.76	1.57	0.005
Armox 500T	0.04289	2.1521	2.7575	0.0066

5.2 Results and Discussion

The results from the numerical analysis of the jet formation process as well as the ballistic performance of the EFPs in shaped charge impact are presented in this section. First, the results are compared with available experimental data from literature to validate shaped charge impact simulations [88]. Results are then discussed in two separate sections. In Section 5.2.2, formed projectile shapes are given in detail. Then, in Section 5.2.3, penetration performance of formed EFPs are analyzed by utilizing FE and SPH methods. A study of varying thickness, maximum penetration depth, and impact angle are also covered.

5.2.1 Comparison with experiments

To validate the results for the process, experimental data in [88] is used that examines the ballistic performance of shaped charge impact process. with a similar configuration where 8701 explosive, copper liner and #45 steel target are utilized. The diameter and length of the explosive charge are 60 and 66 mm respectively. The mass of the liner is 72 g and the target thickness is 25 mm. Simulation of this configuration is

done the same way as explained previously.

First, the detonation and jet formation processes are conducted. The shape and velocity of the EFP are taken at $336 \mu s$ where the velocity of the projectile stabilizes before impact. In the experiments, the diameter and length of the EFP are measured as 15 and 40 mm respectively. In simulations diameter of the EFP is 16.6 mm whereas the length of the EFP is 41.2 mm and the formed shape is shown in Figure 5.7. The simulations are conducted using ABAQUS/Explicit. In [88], simulations are conducted using LS-DYNA. The diameter and length of the EFP is found as 16.7 and 47.6 mm, respectively in the aforementioned study. A comparison of the formed shape of the EFP is shown in Figure 5.7.



Figure 5.7: Formed 2D shape and 3D models of EFPs at the onset of impact with ABAQUS. Deformable EFP is from [88] with LS-DYNA.

Velocity before penetration is measured as 1556 m/s in the experiments and 1501 m/s in the simulations. After obtaining the shape, the penetration process is simulated in 3D utilizing FE and SPH methods. Failure mechanisms are shown in Figure 5.8. FE method shows plug formation and fragmentation failure mechanisms while SPH shows only fragmentation. In the experiments plug formation is observed. Hence it can be said that FE can predict failure mechanism better than SPH method. Moreover, the residual velocity of the EFP predicted as 931 and 958 m/s with FE and SPH methods, respectively. In the experiments residual velocity is 798 m/s. FE and SPH methods predict residual velocity with approximately 14% and 16% error, respectively. In the aforementioned study, when deformable EFP is used residual velocity is found to be 694 m/s. Hence, with a deformable projectile residual velocity is underestimated with 14% error. This can be attribute to the to the rigid modeling of the EFP and inaccuracies in damage model of the target. Assuming the projectile

as a rigid body reduces the computational cost with increased residual velocity estimations while the failure mechanisms of the target can still be predicted with FE method.

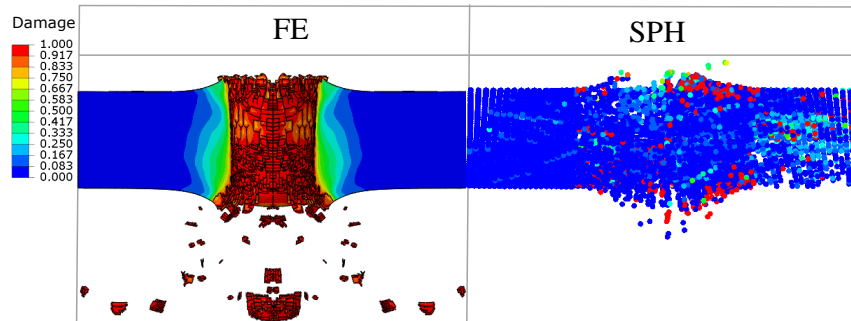


Figure 5.8: Failure mechanisms of 25 mm thick #45 steel target with FE and SPH methods.

5.2.2 Jet formation results

In order to compare and validate the simulation process with the experimental results presented in [55], the jet formation is simulated with copper and iron liners with the geometry used in experiments (bowl-shaped liner with $m = 9.5$ mm). In Figure 5.9, the results from the 2D analysis and the 3D models generated based on the 2D projectile shape is presented. The iron liner forms a wider but shorter projectile while it is longer and thinner with a copper liner. The velocity of the EFPs are found to be 1482 m/s and 1592 m/s, respectively, at the onset of impact. The experimental results demonstrate that the final velocity for copper EFP is 1489 m/s and for iron EFP it is 1632 m/s. Experimental data and simulation results are in good agreement with less than 2.5 % error.

The detailed experimental analysis of detonation and jet formation is not straightforward and it is not easy to illustrate the influence of liner geometry, which could be done employing the current modeling strategy. For that purpose, two different configurations are studied with copper liners as discussed previously. For the conical liner, cone angles are investigated between $\alpha = 65^\circ$ and $\alpha = 90^\circ$ with $\alpha = 90^\circ$ representing a flat liner. Bowl-shaped liner geometry is studied between $m = 7.5$ mm





	2D EFP	3D EFP
Copper Liner		
Iron Liner		

Figure 5.9: Formed 2D shape and 3D models of EFPs at the onset of impact for bowl-shaped liner with $m = 9.5$ mm (correspond to the experimental setup).

and $m = 11.5$ mm. The obtained EFP shapes from the computational analysis are plotted in Figure 5.10 for various configurations. The results reveal that as the cone angle decreases and m parameter increases, the projectiles become sharper, longer, and faster. The obtained velocity values of the respective geometries at the onset of impact are given in Table 5.8. The obtained velocity values are used as the impact velocity in Section 5.2.3. At $\alpha = 90^\circ$ the shape of the EFP is very blunt compared to other configurations. As α decreases, the projectiles become extremely narrow and pointy with increased velocity which is actually an experimentally observed trend (see [64]). Moreover, it is observed that the projectile shapes for $m = 7.5$, $m = 8.5$, and $m = 9.5$ mm are quite similar to each other while the variation of the cone angle results in a substantial change in the final shape of the projectile indicating a higher sensitivity of the EFP to the cone angle.

It is not always possible to directly compare all these EFP shapes after the jet formation just before impact due to the lack of experimental data. However, shapes can be validated using the fracture characteristic of the target after penetration. In this way, numerical studies give the opportunity for the evaluation of jet formation process without extensive experimental work. In Table 5.9, the experimental and the numerical results for penetration hole sizes are compared for a bowl-shaped liner with

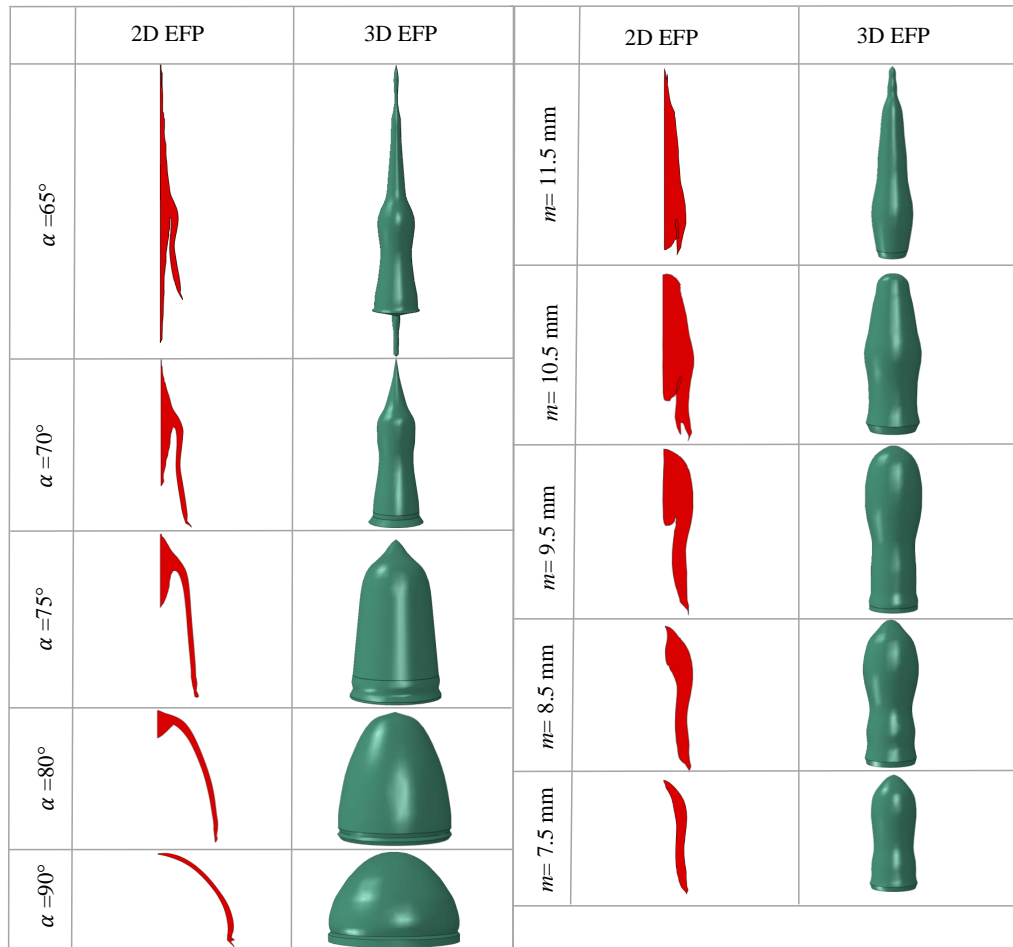


Figure 5.10: Formed 2D shape and 3D models of EFPs at the onset of impact at various configurations.

Table 5.8: EFP velocities at the onset of impact.

	$\alpha = 65^\circ$	$\alpha = 70^\circ$	$\alpha = 75^\circ$	$\alpha = 80^\circ$	$\alpha = 90^\circ$
Velocity (m/s)	1517.20	1506.44	1451.08	1411.57	1275.36
	$m = 11.5$	$m = 10.5$	$m = 9.5$	$m = 8.5$	$m = 7.5$
Velocity (m/s)	1491.76	1480.28	1482.39	1455.48	1420.32

$m = 9.5$ mm for both FE and SPH methods. FE analysis is able to capture experimental hole diameter with about 5% and 7% error for copper and iron projectiles,

respectively, while the SPH method consistently showed higher error percentages. Since SPH is a particle-based method, there are no distinct boundaries between failed and intact material. Therefore, the diameter measurement after penetration might not be as accurate as the FE simulations. The error might originate from the assumption of a rigid projectile after the formation where the material is still at elevated temperatures; thus, deformation of the projectile could still be important. Furthermore, the interaction between the EFP and the target material is neglected in the current methodology. However, it has been reported that some liner material remains around the penetration zone after shaped charge impact (see [55]).

Table 5.9: Hole diameter at the inlet after penetration using the projectile geometries in Figure 5.9 (correspond to the experimental setup). Simulation vs. Experiments [55]

Hole diameter [cm]	Experiment	#45 steel - FE	#45 steel - SPH
Copper	5.74	5.44	5.38
Iron	6.88	6.38	6.13

5.2.3 Ballistic performance analysis

This section covers a detailed ballistic performance analysis of the EFPs impacted on #45 and Armox 500T steel targets, which is missing in the open literature. In previous chapters, the importance of validating simulation outcomes by confirming that energy is conserved during the simulations is discussed. This step is crucial to ensure the precision of the results. Hence, this is demonstrated in Figure 5.11, which shows the conservation of kinetic energy, internal energy, hourglass energy, and total energy for a bowl-shaped liner with $m = 9.5\text{mm}$ using Armox 500T target. The hourglass energy appears to be less than 2% of the total energy throughout the impact phase, showing that hourglassing is not a concern. It is established that the energy dissipated by element elimination is not significant (less than 1% of total energy).

Initially, the failure behavior of #45 and Armox 500T steel targets against copper and iron EFPs (bowl-shaped liner with $m = 9.5\text{mm}$), presented in Figure 5.9, are

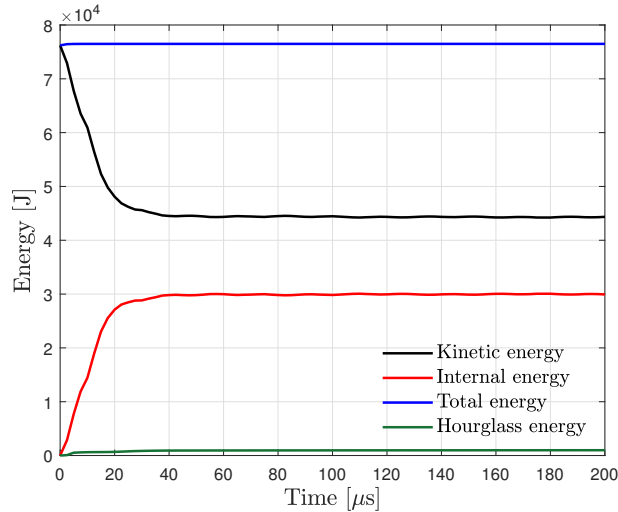


Figure 5.11: Energy time history of the target and projectile.

illustrated in Figure 5.12. The contour plots of the targets after the impact are shown perpendicular to the projectile movement with projectiles moving from top to bottom. For #45 steel target, it is observed that plug formation occurs in FE simulations which is in agreement with experimental observation, while for ArmoX 500T target, EFP is prevented from penetrating and a very small plug is formed. Plug formation is a failure mechanism in ballistic impact when a portion of the target separates as a whole after the impact. Furthermore, for #45 steel, the observed failure mode is both plug formation and fragmentation, which is another failure mechanism where the target breaks apart into smaller pieces. For ArmoX 500T, complete failure is not observed and only a bulge formed. SPH method shows only fragmentation type of failure and no plug formation is observed due to the particle-based nature of the method. It should be noted that the shaped charge impact experiment for #45 steel and iron liner resulted in a bulge without complete penetration, unlike the current numerical results. This is mostly due to the rigid projectile assumption.

For the numerical analysis of ballistic performance, we opted to use the copper liner as it is a commonly used liner material in shaped charge devices. Figure 5.13 shows the failure behavior of targets against EFPs that are formed with various cone angles utilizing FE and SPH methods. It has been shown that the hole width increases along with the cone angle and the SPH method predicts approximately the same hole size as the FE method. Besides, the EFP failed to penetrate the target at $\alpha = 90^\circ$ for #45 steel

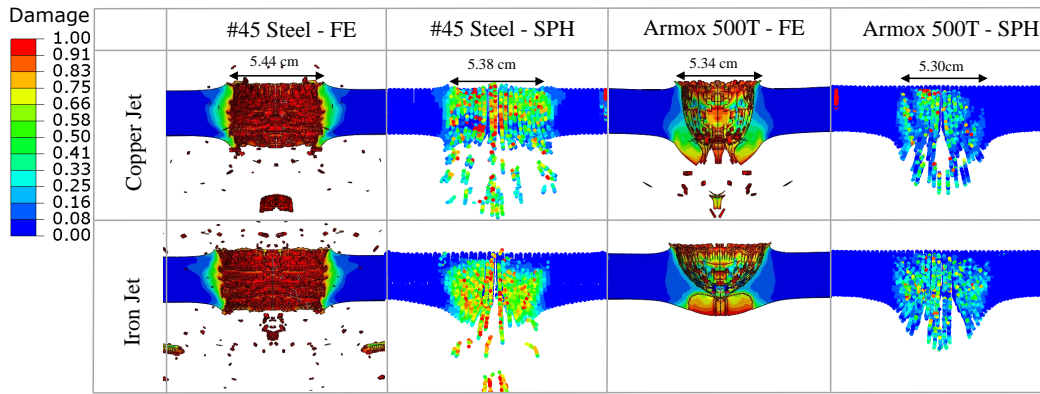


Figure 5.12: Failure mechanisms of #45 steel and ArmoX 500T targets using copper and iron EFPs.

and at $\alpha = 80^\circ$ and $\alpha = 90^\circ$ for ArmoX 500T. Between $\alpha = 65^\circ$ and $\alpha = 75^\circ$, ductile hole enlargement and fragmentation are the observed failure mechanisms. The size of the fragments increases at $\alpha = 80^\circ$. Additionally, for #45 steel targets, plug formation and fragmentation happened at $\alpha = 90^\circ$. However, the projectile failed to penetrate ArmoX 500T target at cone angles of $\alpha = 80^\circ$ and $\alpha = 90^\circ$. SPH method again failed to show failure mechanisms other than fragmentation while it is capable of predicting similar hole diameters as FE analysis.

In Figure 5.14 failure behaviors are illustrated for #45 steel and ArmoX 500T targets against EFPs produced at different m values using FE and SPH methods. It is demonstrated that the size of the hole decreases as the m parameter increase due to the generated EFP shapes. The observed failure mechanisms are mostly ductile hole enlargement with a small number of fragments occurring compared to the previous results with cone-shaped liners. Again, similar outcomes are anticipated by FE and SPH methods in terms of hole sizes.

Residual velocities, which is the remaining velocity of the projectile after penetration, of the EFPs for various cone angles impacted on #45 steel and ArmoX 500T targets are presented in Figure 5.15a. As the cone angle increases resulting in a flatter liner, residual velocity decreases significantly mostly due to a more blunt projectile. After $\alpha = 80^\circ$, EFP failed to penetrate the ArmoX 500T target while the limit is between $\alpha = 80^\circ - 90^\circ$ for the #45 steel target. Slight variations are observed between FE

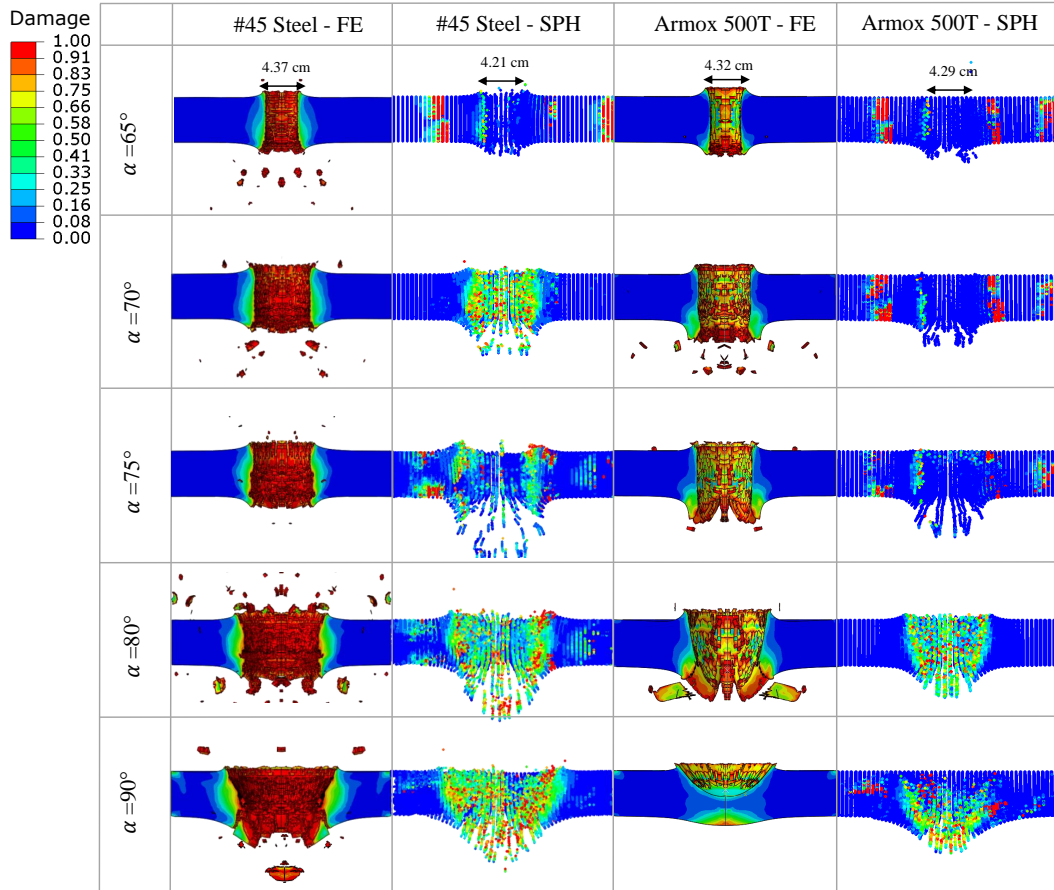


Figure 5.13: Failure mechanisms of #45 steel and ArmoX 500T targets using EFPs with various cone angles.

and SPH analysis where SPH simulations consistently yield higher residual velocities. A maximum difference of 137 m/s is observed between these two numerical methods at $\alpha = 80^\circ$ against #45 steel target. Moreover, #45 steel targets always have higher residual velocities than ArmoX 500T targets demonstrating the higher ballistic resistance of ArmoX 500T, a common armor material used for military vehicles. In addition, the hole diameters are shown in the same figure with blue colored lines for various cone angles. Hole diameter could be associated with the damage after the impact and it inversely affected with cone angle where hole diameter increases with increasing α . Since the hole diameter is mostly affected by the shape of the projectile, the results are almost identical for both target materials with FE and SPH methods.

In Figure 5.15b effect of varying m parameter of the bowl-shaped liner on residual

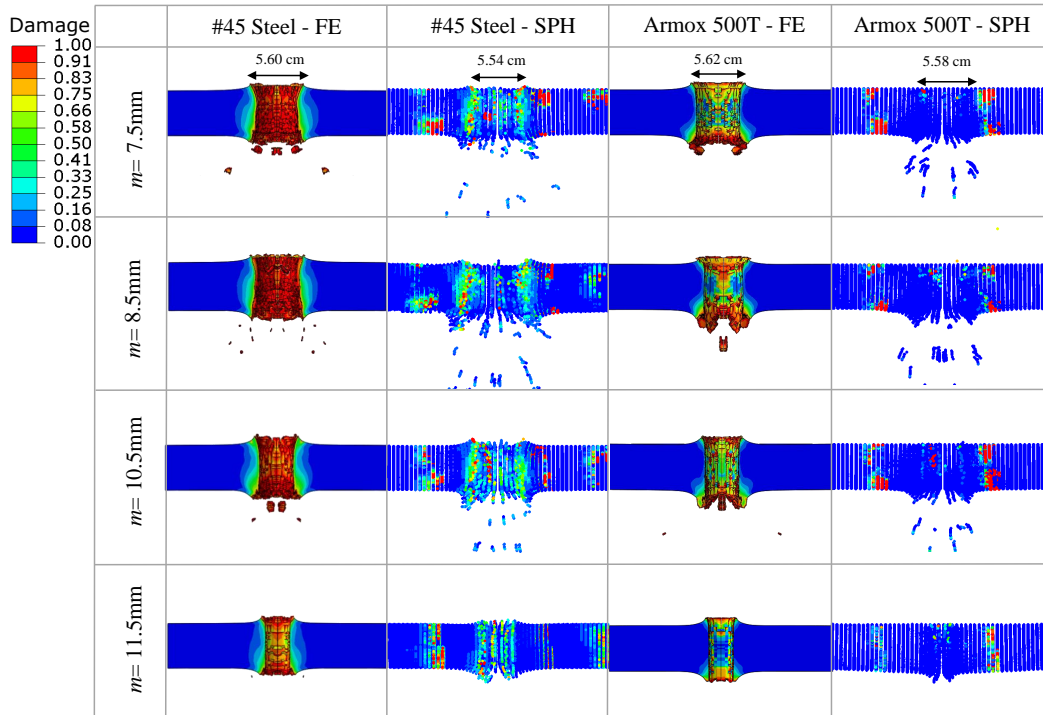
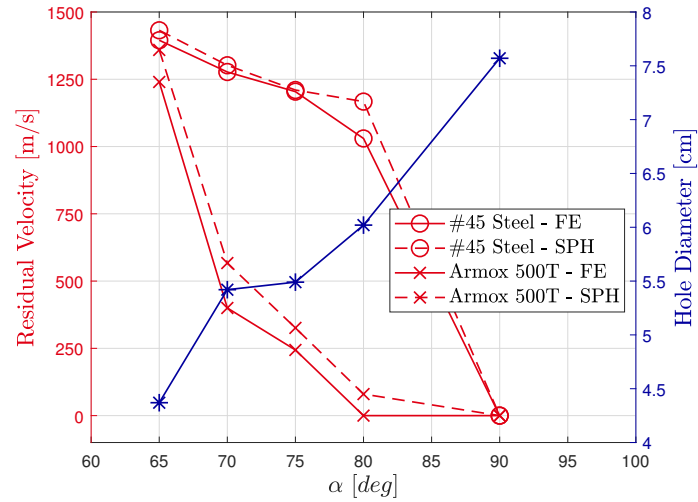
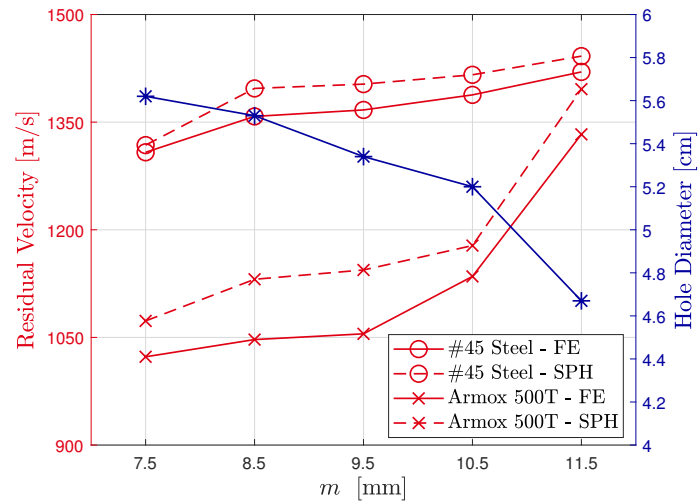


Figure 5.14: Failure mechanisms of #45 steel and ArmoX 500T targets using EFPs with different m parameter.

velocity and hole diameter for #45 steel and ArmoX 500T targets are depicted. Increasing m and decreasing α have a similar increasing effect on residual velocity. The ballistic performance is found to be less sensitive to the parameter m with a smaller variation in residual velocity. It can be said that the bowl-shaped liner geometry is more efficient in pure ballistic performance against a thin metal target plate compared to the conical liner. The highest residual velocity is obtained with a bowl-shaped liner at $m = 11.5$ mm as 1420 m/s. In every instance, the EFPs are able to penetrate the target and residual velocities of ArmoX 500T targets are lower than #45 steel targets as expected. SPH predicts residual velocities slightly greater than FE analysis, in accordance with the data gathered from simulations with various cone angles. The inverse relation between hole diameter and residual velocity is also present. At the peak residual velocity for both conical ($\alpha = 65^\circ$) and bowl-shaped ($m = 11.5$ mm) liners, penetration zones are found to be comparable in size with a slightly higher hole diameter of EFP for bowl-shaped liner. Note that SPH is computationally faster compared to the FE analysis with similar accuracy while FE is favored to obtain failure



(a) Conical liner



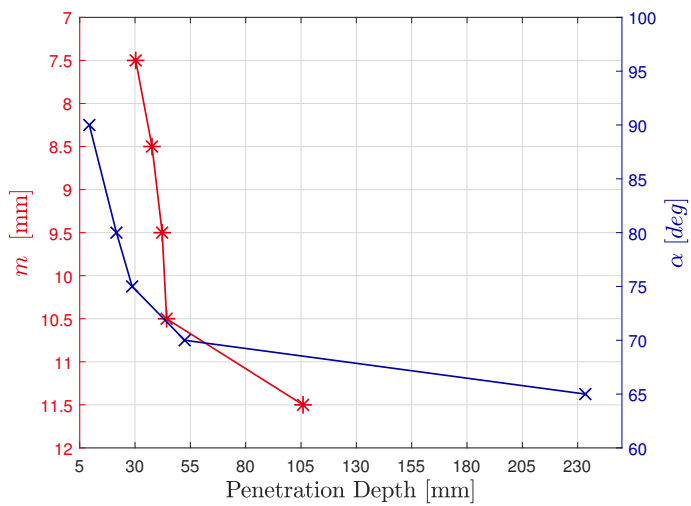
(b) Bowl-shaped liner

Figure 5.15: Residual velocity and hole diameter vs. cone angle and m parameter for #45 steel and Armox 500T targets with FE and SPH methods.

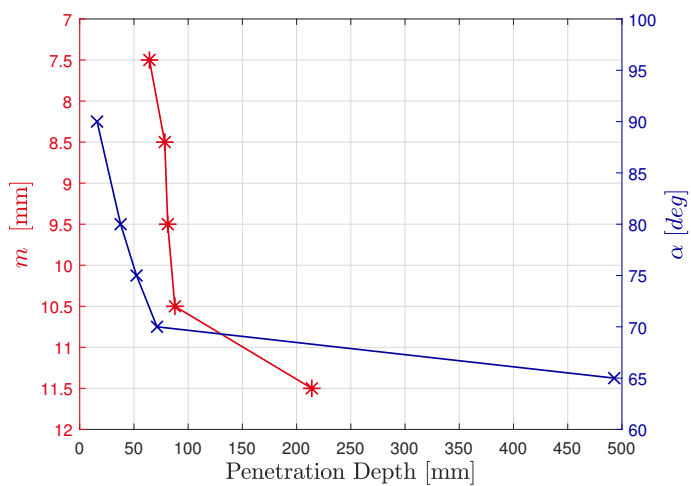
modes in accordance with the literature (e.g. [98]).

The same projectiles are then impacted on a 250 mm thick Armox 500T and 500 mm thick #45 steel structures. In Figure 5.16a, the penetration depth with varying liner geometry for Armox 500T target is depicted. For conical liners, penetration depth significantly increases at cone angles smaller than 70° . Maximum penetration

depth is achieved with conical liner at $\alpha = 65^\circ$ as 233 mm. A very similar pattern is observed for #45 steel targets (see Figure 5.16b). However, compared to Armox 500T, penetration depth is approximately two times greater. Maximum penetration depth for conical liner at $\alpha = 65^\circ$ is observed as 492 mm. Illustration of maximum penetration depth is shown in Figure 5.17. Simulations suggest that the EFP should be as sharp and thin as possible to achieve maximum penetration depth regardless of impact velocity.



(a) Armox 500T.



(b) #45 steel

Figure 5.16: Penetration depth vs. cone angle and m parameter.

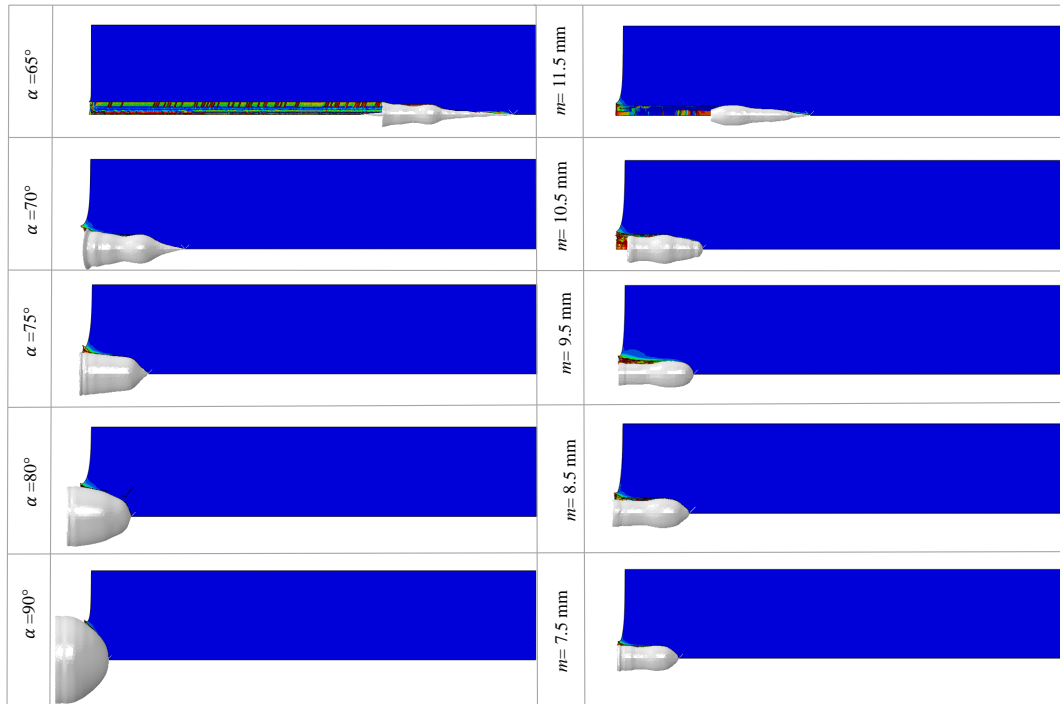
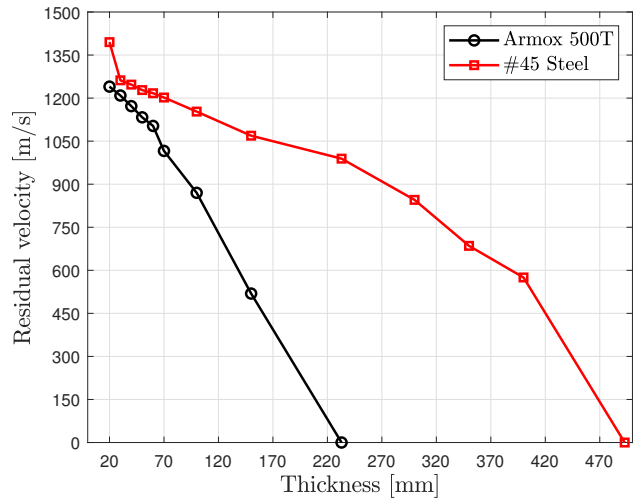


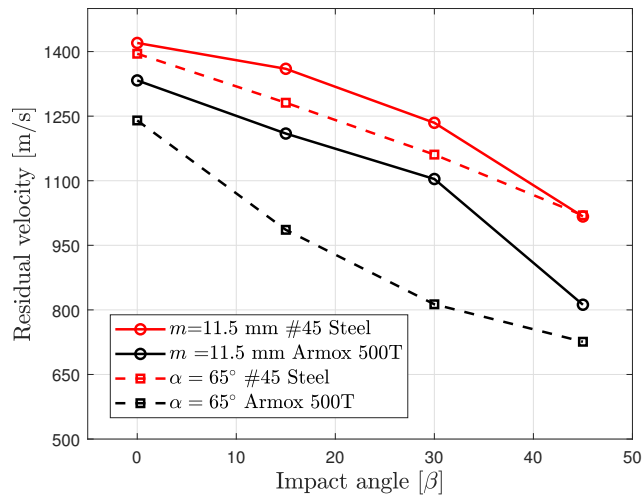
Figure 5.17: Maximum penetration depth for 250 mm thick Armox 500T.

Figure 5.18a illustrates the effect of the thickness of the target plate on residual velocity. Due to its significantly greater maximum penetration depth than that of all other EFPs, the EFP with $\alpha = 65^\circ$ offers the greatest range for examining how target thickness affects residual velocity. Conical liner with $\alpha = 65^\circ$ is fired against #45 and Armox 500T steel targets with a thickness range from 20 mm to 250 mm for Armox 500T and 20 mm to 500 mm for #45 steel. It is observed that the increase in thickness of the target plate, results in decreased residual velocity. At lower target thickness values, the target material has a reduced effect on residual velocity. As the target gets thicker, the difference between Armox 500T and #45 steel increases significantly. EFPs fails to penetrate Armox 500T at 233 mm thickness and #45 steel at 492 mm thickness.

Effect of varying impact angle on residual velocity is illustrated in Figure 5.18b using liners with $\alpha = 65^\circ$ and $m = 11.5$. Impact angle is varied as 0° , 15° , 30° and 45° . The results demonstrate that the residual velocity achieved with the Armox 500T target is consistently lower than that obtained with #45 steel. When EFP with $m = 11.5$ is used residual velocity decreases by 28% for #45 steel and 39% for Armox 500T



(a) Residual velocity vs. thickness



(b) Residual velocity vs. impact angle

Figure 5.18: Plot for #45 and ArmoX 500T (a) using conical liner with $\alpha = 65^\circ$ and (b) steel targets using EFPs with $\alpha = 65^\circ$ and $m = 11.5$.

when the impact angle is increased. Moreover, when the impact angle is increased, for EFP with $\alpha = 65^\circ$, decrease in residual velocity is 26% for #45 steel and 41% for ArmoX 500T. Overall, it is determined that ArmoX 500T has a higher percentage of preventing EFP from penetration under oblique impacts as well.

Figure 5.19 depicts the failure mechanisms of #45 and ArmoX 500T steel targets

with various impact angles using EFPs with $\alpha = 65^\circ$ and $m = 11.5$. Ductile hole enlargement failure mechanism is observed for all cases. When EFP with $\alpha = 65^\circ$ is used for #45 steel targets fragmentation occurs. However, fragmentation is not observed for Armox 500T. At 0° , the greatest number of fragments is observed. The amount of fragments decreases as obliquity increases. Moreover, for EFPs with $m = 11.5$ the difference of failure mechanisms observed between #45 and Armox 500T steel targets is not significant.

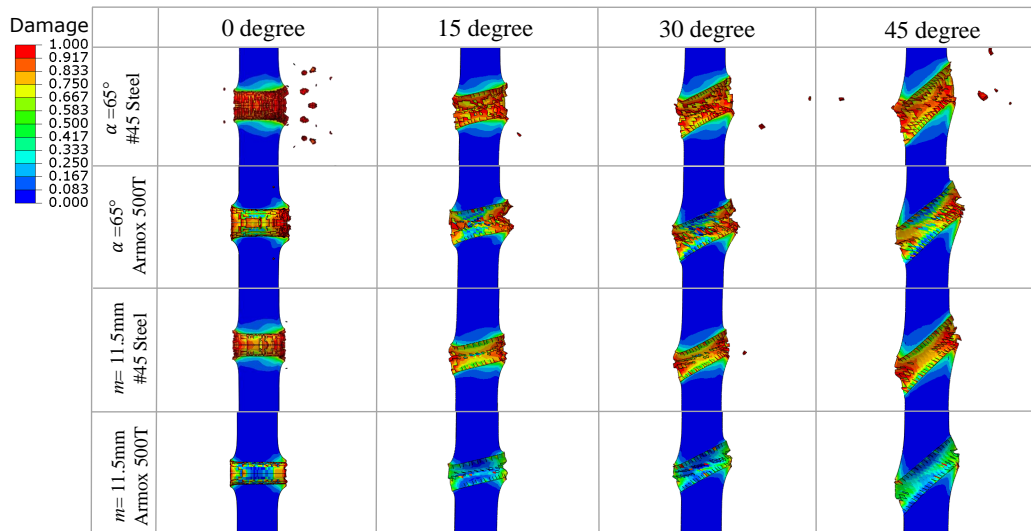


Figure 5.19: Failure mechanisms of #45 steel and Armox 500T targets using EFPs with $\alpha = 65^\circ$ and $m = 11.5$.

CHAPTER 6

CONCLUSIONS

The behavior of metal targets exposed to ballistic and shaped charge impact is examined in this thesis using numerical simulations with FE and SPH techniques. The study includes a thorough examination of various modeling approaches and different damage models for a range of configurations, and the outcomes are confirmed by available experimental tests from the literature. The study conducted in this thesis is divided into 3 chapters. First, the ballistic impact performance of aluminum alloy 2024-T351 is examined with various configurations. Then an extended study is conducted for armor steel Armox 500T where the damage model parameters are calibrated. Lastly, the ballistic performance of shaped charge impact is studied for various configurations for #45 and Armox 500T steels. Hence, first, a general conclusion is drawn that this thesis provides insights into the behavior of different materials and configurations subjected to impact loads. Then for each chapter, in depth, conclusions are presented separately.

Overall, the results demonstrate that blunt projectiles, which are the most sensitive to parameter change. Moreover, the failure mechanism of the target is difficult to demonstrate in SPH simulations. However, SPH can be useful for predicting fast residual velocity and hole diameter results. Furthermore, the performance of JC and MMC varies for different configurations, highlighting the need for further research in this area.

In Chapter 3, the effects of projectile nose shapes, target thickness and impact angle in ballistic impact are investigated using numerical simulations for aluminum alloy 2024-T351 and preliminary results are already published in [99]. The damage model and material parameters are taken from the literature as well as experimental data

[38]. JC and MMC damage models are used to compare FE and SPH approaches. For the FE method, the MMC and JC models produce significantly different outcomes, with the MMC model correlating better with experiments. However, in the SPH method, JC and MMC models are in relatively better agreement for the blunt and hemispherical projectile. When compared to experimental data, the SPH approach produces higher residual velocity for the ogival projectile. Furthermore, except in the JC model, results show that decreasing the thickness of the target plate resulted in a linear increase in residual velocity. In the oblique impact simulations, increasing the obliquity of the target plate resulted in larger holes and greater separation of petals from the target. The velocity of the blunt projectile changes significantly as the impact angle changes, but the velocity of the other two projectiles does not vary significantly at low obliquity. While the FE approach is consistent in most circumstances, the SPH method, with the exception of blunt-shaped projectiles, overpredicts the residual velocity values at initial velocities less than 200 m/s. Furthermore, some SPH simulations have difficulty displaying the target's failure mechanism.

In Chapter 4, the JC and the MMC models are comparatively studied for the ballistic impact process with Armox 500T armor steel targets. Results of this Chapter are to be submitted to the Engineering Fracture Mechanics Journal. Fracture model parameters are calibrated for Armox 500T steel using tensile tests presented in the literature for various specimen geometries [90]. These models are then validated and compared with ballistic test data. The results show that the residual velocity predicted by the JC model is more accurate than the residual velocity predicted by the MMC model. However, the failure mechanisms displayed using the MMC model are more compatible with experimental findings. The difference between the model predictions is then studied thoroughly with various target thicknesses, impact angles, and obliquity configurations. For all configurations, the difference between residual velocities obtained with the MMC and JC models decreases with increasing the initial velocity. Overall, the relative difference between the models is increased with increasing target thickness and impact angle. Blunt projectile nose shape is the most sensitive to varying target thickness and impact angle whereas 7.62 API is mostly insensitive. Additionally, the failure modes of the 7.62 API projectile demonstrated by the MMC and JC models began to differ as the impact angle increased. For blunt projectiles,

shear plugging and fragmentation are observed at lower obliquity, whereas failure by tearing occurs at higher obliquity. Fragmentation and ductile hole enlargement are identified as the main failure modes for the hemispherical projectile. 7.62 API projectile exhibits mostly ductile hole enlargement. The difference between the JC and MMC models is not significant at low obliquity. However, petaling, an experimentally observed phenomenon at oblique impact, is predicted by the MMC model at 45° and 60°, but not with the JC model.

Finally, in Chapter 5, the projectile formation of shaped charges and their ballistic performance on targets made up of #45 and Armox 500T steels are numerically studied through FE and SPH analysis in this work and results are submitted to the Journal of Applied Mechanics.. The influence of the cone angle of the conical liner and the depth of the bowl-shaped liner on penetration performance is investigated. It is observed that the projectile shape is highly sensitive to liner geometry. Liners with lower cone angles and higher depth result in sharper and narrower projectiles with increased impact velocities. Experimental validation of the jet formation simulation is performed in terms of the impact velocity demonstrating that numerical methods can be efficient alternatives to experimental work to predict the EFP shapes and their exit velocities. The rigid assumption of EFPs in modeling shaped charge is found to be acceptable for copper liners but it failed to capture experimental results in impact performance with iron as liner material. Rigid assumption decreases the computational cost and predicts failure mode successfully with FE model when copper liner is utilized. However, it overestimates the residual velocity and predicts approximately with 15% error. Hence it can be utilized to study effects of varying design parameters considering its shortcomings. In addition, the ballistic performance of the copper EFPs on the #45 steel and Armox 500T targets are examined using FE and SPH methods. Despite the poor performance of SPH in demonstrating failure mechanism, residual velocity prediction of both FE and SPH showed limited deviation. It is concluded that the SPH method can be used as a faster alternative to predict residual velocities and hole diameters; however, FE analysis is preferred to predict failure modes. It should be noted that Armox 500T targets consistently produce lower residual velocities. Additionally, the penetration depth is nearly twice as much as with #45 steel, indicating higher impact resistance of Armox 500T compared to #45 steel. It

is seen that the penetration depth is substantially increased with thinner and sharper projectiles formed with liners at smaller cone angles.

REFERENCES

- [1] H. K. Cooper and G. J. Bowen, "Metal armor from St. Lawrence Island," *Arctic Anthropology*, vol. 50, no. 1, pp. 1–19, 2013.
- [2] D. Starley, "Determining the technological origins of iron and steel," *Journal of Archaeological Science*, vol. 26, no. 8, pp. 1127–1133, 1999.
- [3] J. A. Zukas, *High velocity impact dynamics*. Wiley-Interscience, 1990.
- [4] P. K. Jena, B. Mishra, K. Siva Kumar, and T. B. Bhat, "An experimental study on the ballistic impact behavior of some metallic armour materials against 7.62mm deformable projectile," *Materials & Design*, vol. 31, no. 7, pp. 3308–3316, 2010.
- [5] S. Ryan, H. Li, M. Edgerton, D. Gallardy, and S. Cimpoeru, "The ballistic performance of an ultra-high hardness armour steel: An experimental investigation," *International Journal of Impact Engineering*, vol. 94, pp. 60–73, 2016.
- [6] P. K. Jena, K. S. Kumar, R. Mandal, and A. Singh, "An experimental study on the fracture behavior of different aluminium alloys subjected to ballistic impact," *Procedia Structural Integrity*, vol. 17, pp. 957–964, 2019. 3rd International Conference on Structural Integrity, ICSI 2019, 2-5 September 2019, Funchal, Madeira, Portugal.
- [7] M. Costas, M. Edwards-Mowforth, M. Kristoffersen, F. Teixeira-Dias, V. Brøtan, C. O. Paulsen, and T. Børvik, "Ballistic impact resistance of additive manufactured high-strength maraging steel: An experimental study," *International Journal of Protective Structures*, vol. 12, no. 4, pp. 577–603, 2021.
- [8] N. Kılıç and B. Ekici, "Ballistic resistance of high hardness armor steels against 7.62mm armor piercing ammunition," *Materials & Design*, vol. 44, pp. 35–48, 2013.

- [9] A. Manes, D. Lumassi, L. Giudici, and M. Giglio, “An experimental–numerical investigation on aluminium tubes subjected to ballistic impact with soft core 7.62 ball projectiles,” *Thin-Walled Structures*, vol. 73, pp. 68–80, 2013.
- [10] P. M. Elek, S. S. Jaramaz, D. M. Micković, and N. M. Miloradović, “Experimental and numerical investigation of perforation of thin steel plates by deformable steel penetrators,” *Thin-Walled Structures*, vol. 102, pp. 58–67, 5 2016.
- [11] A. Mubashar, E. Uddin, S. Anwar, N. Arif, S. W. U. Haq, and M. Chowdhury, “Ballistic response of 12.7mm armour piercing projectile against perforated armour developed from structural steel,” *Proceedings of the Institution of Mechanical Engineers, Part L: Journal of Materials: Design and Applications*, vol. 233, no. 10, pp. 1993–2005, 2019.
- [12] Y. Xiao, H. Dong, J. Zhou, and J. Wang, “Studying normal perforation of monolithic and layered steel targets by conical projectiles with sph simulation and analytical method,” *Engineering Analysis with Boundary Elements*, vol. 75, pp. 12–20, 2 2017.
- [13] M. Rodriguez-Millan, D. Garcia-Gonzalez, A. Rusinek, F. Abed, and A. Arias, “Perforation mechanics of 2024 aluminium protective plates subjected to impact by different nose shapes of projectiles,” *Thin-Walled Structures*, vol. 123, pp. 1–10, 2 2018.
- [14] T. Yalcinkaya and A. Cocks, “Physics based formulation of a cohesive zone model for ductile fracture,” in *Material Forming ESAFORM 2015*, vol. 651 of *Key Engineering Materials*, pp. 993–999, Trans Tech Publications Ltd, 8 2015.
- [15] T. Yalçinkaya and A. Cocks, “Micromechanical cohesive zone relations for ductile fracture,” *Procedia Structural Integrity*, vol. 2, pp. 1716–1723, 2016. 21st European Conference on Fracture, ECF21, 20-24 June 2016, Catania, Italy.
- [16] T. Yalçinkaya, I. T. Tandogan, and A. Cocks, “Development of a micromechanics based cohesive zone model and application for ductile fracture,” *Procedia Structural Integrity*, vol. 21, pp. 52–60, 2019. 1st International Workshop on Plasticity, Damage and Fracture of Engineering Materials, IWPDF 2019, 22-23 August 2019, Ankara, Turkey.

- [17] I. Tandogan and T. Yalcinkaya, “Development and implementation of a micromechanically motivated cohesive zone model for ductile fracture,” *International Journal of Plasticity*, vol. 158, p. 103427, 2022.
- [18] T. Yalçinkaya, B. Tatli, I. Erkin Ünsal, and I. U. Aydiner, “Crack initiation and propagation in dual-phase steels through crystal plasticity and cohesive zone frameworks,” *Procedia Structural Integrity*, vol. 42, pp. 1651–1659, 2022. 23 European Conference on Fracture.
- [19] A. L. Gurson, “Continuum Theory of Ductile Rupture by Void Nucleation and Growth: Part I—Yield Criteria and Flow Rules for Porous Ductile Media,” *Journal of Engineering Materials and Technology*, vol. 99, pp. 2–15, 01 1977.
- [20] V. Tvergaard and A. Needleman, “Analysis of the cup-cone fracture in a round tensile bar,” *Acta Metallurgica*, vol. 32, no. 1, pp. 157–169, 1984.
- [21] T. Yalçinkaya, C. Erdoğan, I. T. Tandoğan, and A. Cocks, “Formulation and implementation of a new porous plasticity model,” *Procedia Structural Integrity*, vol. 21, pp. 46–51, 2019.
- [22] M. Cockcroft, “Ductility and workability of metals,” *J. of Metals.*, vol. 96, p. 2444, 1968.
- [23] G. R. Johnson and W. H. Cook, “Fracture characteristics of three metals subjected to various strains, strain rates, temperatures and pressures,” *Engineering Fracture Mechanics*, vol. 21, no. 1, pp. 31–48, 1985.
- [24] Y. Bai and T. Wierzbicki, “Application of extended Mohr-Coulomb criterion to ductile fracture,” *International Journal of Fracture*, vol. 161, pp. 1–20, 1 2010.
- [25] H. Vural, C. Erdoğan, T. O. Fenercioğlu, and T. Yalçinkaya, “Ductile failure prediction during the flow forming process,” *Procedia Structural Integrity*, vol. 35, pp. 25–33, 2022.
- [26] C. Erdoğan, H. Vural, T. O. Fenercioğlu, and T. Yalçinkaya, “Effect of process parameters on the ductile failure behavior of flow forming process,” *Procedia Structural Integrity*, vol. 42, pp. 1643–1650, 2022. 23 European Conference on Fracture.

- [27] A. Rusinek, J. Rodríguez-Martínez, A. Arias, J. Klepaczko, and J. López-Puente, “Influence of conical projectile diameter on perpendicular impact of thin steel plate,” *Engineering Fracture Mechanics*, vol. 75, no. 10, pp. 2946–2967, 2008.
- [28] X. Wang and J. Shi, “Validation of johnson-cook plasticity and damage model using impact experiment,” *International Journal of Impact Engineering*, vol. 60, pp. 67–75, 2013.
- [29] K. Senthil and M. Iqbal, “Effect of projectile diameter on ballistic resistance and failure mechanism of single and layered aluminum plates,” *Theoretical and Applied Fracture Mechanics*, vol. 67-68, pp. 53–64, 2013.
- [30] M. Rodríguez-Millán, A. Díaz-Álvarez, R. Bernier, M. H. Miguélez, and J. A. Loya, “Experimental and numerical analysis of conical projectile impact on Inconel 718 plates,” *Metals*, vol. 9, no. 6, 2019.
- [31] Y. Bai and T. Wierzbicki, “A new model of metal plasticity and fracture with pressure and lode dependence,” *International Journal of Plasticity*, vol. 24, no. 6, pp. 1071–1096, 2008.
- [32] J. K. Holmen, O. S. Hopperstad, and T. Børvik, “Low-velocity impact on multi-layered dual-phase steel plates,” *International Journal of Impact Engineering*, vol. 78, pp. 161–177, 2015.
- [33] J. K. Holmen, J. Johnsen, O. S. Hopperstad, and T. Børvik, “Influence of fragmentation on the capacity of aluminum alloy plates subjected to ballistic impact,” *European Journal of Mechanics - A/Solids*, vol. 55, pp. 221–233, 2016.
- [34] J. K. Holmen, O. S. Hopperstad, and T. Børvik, “Influence of yield-surface shape in simulation of ballistic impact,” *International Journal of Impact Engineering*, vol. 108, pp. 136–146, 2017. In Honour of the Editor-in-Chief, Professor Magnus Langseth, on his 65th Birthday.
- [35] J. K. Holmen, S. Thomesen, M. J. Perez-Martin, O. S. Hopperstad, and T. Børvik, “Ballistic impact of structural steels at low temperatures,” *Journal of Applied Mechanics*, vol. 89, no. 10, 2022. 101001.

- [36] C. C. Roth, T. Frasn, and D. Mohr, "Dynamic perforation of lightweight armor: Temperature-dependent plasticity and fracture of aluminum 7020-T6," *Mechanics of Materials*, vol. 149, p. 103537, 2020.
- [37] T. Frasn, C. C. Roth, and D. Mohr, "Dynamic perforation of ultra-hard high-strength armor steel: Impact experiments and modeling," *International Journal of Impact Engineering*, vol. 131, pp. 256–271, 2019.
- [38] Y. Wang, X. Chen, X. Xiao, V. V. Vershinin, R. Ge, and D. sen Li, "Effect of lode angle incorporation into a fracture criterion in predicting the ballistic resistance of 2024-T351 aluminum alloy plates struck by cylindrical projectiles with different nose shapes," *International Journal of Impact Engineering*, vol. 139, p. 103498, 2020.
- [39] Y. Deng, H. Wu, Y. Zhang, X. Huang, X. Xiao, and Y. Lv, "Experimental and numerical study on the ballistic resistance of 6061-T651 aluminum alloy thin plates struck by different nose shapes of projectiles," *International Journal of Impact Engineering*, vol. 160, p. 104083, 2022.
- [40] X. Xiao, Y. Wang, V. V. Vershinin, L. Chen, and Y. Lou, "Effect of Lode angle in predicting the ballistic resistance of Wieldox 700 E steel plates struck by blunt projectiles," *International Journal of Impact Engineering*, vol. 128, pp. 46–71, 2019.
- [41] X. Xiao, H. Pan, Y. Bai, Y. Lou, and L. Chen, "Application of the modified Mohr–Coulomb fracture criterion in predicting the ballistic resistance of 2024-T351 aluminum alloy plates impacted by blunt projectiles," *International Journal of Impact Engineering*, vol. 123, pp. 26–37, 2019.
- [42] X. Xiao, Y. Shi, Y. Wang, X. Chen, and B. Jia, "Effect of incorporating lode angle parameter into a fracture criterion in predicting ballistic impact behavior of double-layered 2024-T351 aluminum alloy plates against blunt projectiles," *International Journal of Impact Engineering*, vol. 160, p. 104082, 2022.
- [43] Z. Mohammad, P. K. Gupta, and A. Baqi, "Experimental and numerical investigations on the behavior of thin metallic plate targets subjected to ballistic impact," *International Journal of Impact Engineering*, vol. 146, p. 103717, 2020.

- [44] M. Iqbal, K. Senthil, V. Madhu, and N. Gupta, "Oblique impact on single, layered and spaced mild steel targets by 7.62 AP projectiles," *International Journal of Impact Engineering*, vol. 110, pp. 26–38, 2017. Special Issue in honor of Seventy Fifth Birthday of Professor N. K. Gupta.
- [45] J. Han, Y. Shi, Q. Ma, V. V. Vershinin, X. Chen, X. Xiao, and B. Jia, "Experimental and numerical investigation on the ballistic resistance of 2024-T351 aluminum alloy plates with various thicknesses struck by blunt projectiles," *International Journal of Impact Engineering*, vol. 163, p. 104182, 2022.
- [46] G. Ben-Dor, A. Dubinsky, and T. Elperin, "Effect of layering on ballistic properties of metallic shields against sharp-nosed rigid projectiles," *Engineering Fracture Mechanics*, vol. 77, no. 14, pp. 2791–2799, 2010.
- [47] Y. Deng, W. Zhang, and Z. Cao, "Experimental investigation on the ballistic resistance of monolithic and multi-layered plates against ogival-nosed rigid projectiles impact," *Materials & Design*, vol. 44, pp. 228–239, 2013.
- [48] K. Senthil and M. Iqbal, "Prediction of superior target layer configuration of armour steel, mild steel and aluminium 7075-T651 alloy against 7.62 AP projectile," *Structures*, vol. 29, pp. 2106–2119, 2021.
- [49] E. Flores-Johnson, M. Saleh, and L. Edwards, "Ballistic performance of multi-layered metallic plates impacted by a 7.62-mm APM2 projectile," *International Journal of Impact Engineering*, vol. 38, no. 12, pp. 1022–1032, 2011.
- [50] E. Palta, M. Gutowski, and H. Fang, "A numerical study of steel and hybrid armor plates under ballistic impacts," *International Journal of Solids and Structures*, vol. 136-137, pp. 279–294, 2018.
- [51] A. Paman, G. Sukumar, B. Ramakrishna, and V. Madhu, "An optimization scheme for a multilayer armour module against 7.62 mm armour piercing projectile," *International Journal of Protective Structures*, vol. 11, no. 2, pp. 185–208, 2020.
- [52] W. Walters and A. P. Ground, "An overview of the shaped charge concept," in *11th Annual ARL/USMA Technical Symposium*, vol. 5, 2003.

- [53] I. G. Cullis and R. Townsley, "The potential of FOX-7 explosive in insensitive munition design," *Journal of Applied Mechanics*, vol. 78, 08 2011.
- [54] P. Church, R. Claridge, P. Ottley, I. Lewtas, N. Harrison, P. Gould, C. Braithwaite, and D. Williamson, "Investigation of a nickel-aluminum reactive shaped charge liner," *Journal of Applied Mechanics*, vol. 80, 04 2013. 031701.
- [55] J. Liu, Y. Long, C. Ji, M. Zhong, and Q. Liu, "The influence of liner material on the dynamic response of the finite steel target subjected to high velocity impact by explosively formed projectile," *International Journal of Impact Engineering*, vol. 109, pp. 264–275, 2017.
- [56] J. Liu, Y. Long, and C. Ji, "Ballistic performance study on the finite steel target subjected to normal and oblique impact by copper explosively formed projectile," *International Journal of Protective Structures*, vol. 9, no. 4, pp. 461–483, 2018.
- [57] W. long Xu, C. Wang, J. ming Yuan, and T. Deng, "Bore-center annular shaped charges with different liner materials penetrating into steel targets," *Defence Technology*, vol. 15, no. 5, pp. 796–801, 2019. SI: 2019 International Symp. Ballistics.
- [58] P. Appelgren, M. Skoglund, P. Lundberg, L. Westerling, A. Larsson, and T. Hurtig, "Experimental study of electromagnetic effects on solid copper jets," *Journal of Applied Mechanics*, vol. 77, 09 2009. 011010.
- [59] K. H. Kamarudin, A. M. A. Zaidi, S. Abdullah, and M. F. S. Koslan, "Establishment of Shaped Charge Optimum Parameters for Small Scale Hydrodynamic Penetration," *Modern Applied Science*, vol. 10, pp. 1–82, January 2015.
- [60] H. Wu, F. Hu, and Q. Fang, "A comparative study for the impact performance of shaped charge jet on uhpc targets," *Defence Technology*, vol. 15, no. 4, pp. 506–518, 2019.
- [61] C. Wang, T. Ma, and J. Ning, "Experimental investigation of penetration performance of shaped charge into concrete targets," *Acta Mechanica Sinica*, vol. 24, no. 3, pp. 345–349, 2008.

- [62] M. S. Yavuz, R. O. Yıldırım, and N. Serin, “Numerical and experimental investigation of jet formation and particulation in shaped charges with tulip-like steel liners,” *Procedia Engineering*, vol. 58, pp. 608–616, 2013. Proceedings of the 12th Hypervelocity Impact Symposium.
- [63] N. D. Gerami, G. H. Liaghat, G. H. R. S. Moghadas, and N. Khazraiyani, “Analysis of liner effect on shaped charge penetration into thick concrete targets,” *Journal of the Brazilian Society of Mechanical Sciences and Engineering*, vol. 39, pp. 3189–3201, 2017.
- [64] C. Wang, W. Xu, and S. Chung Kim Yuen, “Penetration of shaped charge into layered and spaced concrete targets,” *International Journal of Impact Engineering*, vol. 112, pp. 193–206, 2018.
- [65] H. Wang, H. Guo, B. Geng, Q. Yu, and Y. Zheng, “Application of ptfе/al reactive materials for double-layered liner shaped charge,” *Materials*, vol. 12, no. 17, 2019.
- [66] H. Zhang, Y. feng Zheng, Q. bo Yu, C. Ge, C. hai Su, and H. fu Wang, “Penetration and internal blast behavior of reactive liner enhanced shaped charge against concrete space,” *Defence Technology*, vol. 18, no. 6, pp. 952–962, 2022.
- [67] V. F. Minin, O. V. Minin, and I. V. Minin, “Physics hypercumulation and comdined shaped charges,” *2012 IEEE 11th International Conference on Actual Problems of Electronics Instrument Engineering (APEIE)*, pp. 34–52, 2012.
- [68] W. Xu, C. Wang, and D. Chen, “The jet formation and penetration capability of hypervelocity shaped charges,” *International Journal of Impact Engineering*, vol. 132, p. 103337, 2019.
- [69] C. Ge, Z. Qu, J. Wang, D. Hu, and Y. Zhang, “Study on jet formation behavior and optimization of trunconical hypercumulation shaped charge structure,” *Defence Technology*, 2022.
- [70] S. Saran, O. Ayısit, and M. S. Yavuz, “Experimental investigations on aluminum shaped charge liners,” *Procedia Engineering*, vol. 58, pp. 479–486, 2013. Proceedings of the 12th Hypervelocity Impact Symposium.

- [71] W. Xu, C. Wang, and J. Yuan, "Impact performance of an annular shaped charge designed by convolutional neural networks," *Thin-Walled Structures*, vol. 160, p. 107241, 2021.
- [72] Z. Zhang, C. Wang, W. Xu, H. Hu, and Y. Guo, "Application of a new type of annular shaped charge in penetration into underwater double-hull structure," *International Journal of Impact Engineering*, vol. 159, p. 104057, 2022.
- [73] W. Guo, J. Liu, Y. Xiao, S. Li, Z. Zhao, and J. Cao, "Comparison of penetration performance and penetration mechanism of w-cu shaped charge liner against three kinds of target: Pure copper, carbon steel and Ti-6Al-4V alloy," *International Journal of Refractory Metals and Hard Materials*, vol. 60, pp. 147–153, 2016.
- [74] T. Elshenawy, A. Elbeih, and Q. Li, "Influence of target strength on the penetration depth of shaped charge jets into RHA targets," *International Journal of Mechanical Sciences*, vol. 136, pp. 234–242, 2018.
- [75] A. Helte and E. Lidén, "The role of Kelvin–Helmholtz instabilities on shaped charge jet interaction with reactive armor plates," *Journal of Applied Mechanics*, vol. 77, 07 2010. 051805.
- [76] A. Wiśniewski, "Explosive sensitivity influence on one- and two-layered reactive armors' behavior," *Journal of Applied Mechanics*, vol. 77, 06 2010. 051901.
- [77] X. Jia, Z. xiang Huang, X. dong Zu, X. hui Gu, C. sheng Zhu, and Z. wen Zhang, "Experimental study on the performance of woven fabric rubber composite armor subjected to shaped charge jet impact," *International Journal of Impact Engineering*, vol. 57, pp. 134–144, 2013.
- [78] H. Guo, Y. Zheng, Q. Yu, C. Ge, and H. Wang, "Penetration behavior of reactive liner shaped charge jet impacting thick steel plates," *International Journal of Impact Engineering*, vol. 126, pp. 76–84, 2019.
- [79] H. G. Guo, S. He, H. B. Ma, T. Sun, and Y. F. Zheng, "Effect of inner liner material on penetration behavior of reactive material double-layered liner shaped charge," *Journal of Physics: Conference Series*, vol. 1507, p. 032005, mar 2020.

- [80] W. Xu, C. Wang, and D. Chen, “Formation of a bore-center annular shaped charge and its penetration into steel targets,” *International Journal of Impact Engineering*, vol. 127, pp. 122–134, 2019.
- [81] D. Pyka, A. Kurzawa, M. Bocian, M. Bajkowski, M. Magier, J. Sliwinski, and K. Jamroziak, “Numerical and experimental studies of the Łk type shaped charge,” *Applied Sciences*, vol. 10, no. 19, 2020.
- [82] P. Żochowski and R. Warchoń, “Experimental and numerical study on the influence of shaped charge liner cavity filing on jet penetration characteristics in steel targets,” *Defence Technology*, 2022.
- [83] Z. Zhang, L. Wang, V. V. Silberschmidt, and S. Wang, “SPH-FEM simulation of shaped-charge jet penetration into double hull: A comparison study for steel and sps,” *Composite Structures*, vol. 155, pp. 135–144, 2016.
- [84] M. Pang, F. Sun, B. Liu, and S. Xue, “An ale approach to the simulation of perforating process,” *IOP Conference Series: Earth and Environmental Science*, vol. 267, p. 042014, may 2019.
- [85] Y. Du, G. He, W. Li, and K. Wang, “Experimental and numerical study on the penetration performance of a shaped charge,” *Materials*, vol. 15, no. 11, 2022.
- [86] Z. Zhang and W.-W. Jin, “Finite element modeling of the shaped charge jet and design of the reusable perforating gun,” *Petroleum Science*, vol. 17, no. 5, pp. 1389–1399, 2020.
- [87] P. Dehestani, A. Fathi, and H. M. Daniali, “Numerical study of the stand-off distance and liner thickness effect on the penetration depth efficiency of shaped charge process,” *Proceedings of the Institution of Mechanical Engineers, Part C: Journal of Mechanical Engineering Science*, vol. 233, no. 3, pp. 977–986, 2019.
- [88] J. Wu, J. Liu, and Y. Du, “Experimental and numerical study on the flight and penetration properties of explosively-formed projectile,” *International Journal of Impact Engineering*, vol. 34, no. 7, pp. 1147–1162, 2007.
- [89] ABAQUS, *The Abaqus documentation collection, version 6.14*. Providence, Rhode Island,: Dassault Systèmes, 2017.

- [90] A. Popławski, P. Kędzierski, and A. Morka, “Identification of Armox 500T steel failure properties in the modeling of perforation problems,” *Materials & Design*, vol. 190, p. 108536, 2020.
- [91] M. Iqbal, K. Senthil, P. Sharma, and N. Gupta, “An investigation of the constitutive behavior of armox 500t steel and armor piercing incendiary projectile material,” *International Journal of Impact Engineering*, vol. 96, pp. 146–164, 2016.
- [92] X. Chen, G. Chen, and F. Zhang, “Deformation and failure modes of soft steel projectiles impacting harder steel targets at increasing velocity,” *Experimental Mechanics*, vol. 48, no. 3, pp. 335–354, 2008.
- [93] Y. Bai, “Effect of loading history on necking and fracture,” *PhD. Massachusetts Institute of Technology, Cambridge, USA*, 2007.
- [94] D. G. Spear, A. N. Palazotto, and R. A. Kemnitz, “Modeling and simulation techniques used in high strain rate projectile impact,” *Mathematics*, vol. 9, no. 3, 2021.
- [95] T. Børvik, L. Olovsson, S. Dey, and M. Langseth, “Normal and oblique impact of small arms bullets on AA6082-T4 aluminium protective plates,” *International Journal of Impact Engineering*, vol. 38, no. 7, pp. 577–589, 2011.
- [96] W. P. Walters, “The shaped charge concept. part 1. introduction,” tech. rep., Army Ballistic Research Lab Aberdeen Proving Ground MD, 1990.
- [97] A. Bolonkin, *Innovations and New Technologies (v2)*. 01 2013.
- [98] Y. Cheng, H. Wu, P. Jiang, and Q. Fang, “Ballistic resistance of high-strength armor steel against ogive-nosed projectile impact,” *Thin-Walled Structures*, vol. 183, p. 110350, 2023.
- [99] Y. Göçmen, H. Vural, C. Erdoğan, and T. Yalçinkaya, “Numerical analysis of ballistic impact through FE and SPH methods,” *Procedia Structural Integrity*, vol. 42, pp. 1736–1743, 2022.